On Kinetics and Thermodynamics of High Angle Grain Boundaries in Aluminum: Experimental Study on Grain Boundary Properties in Bi- and Tricrystals

Von der Fakultät für Georessourcen und Materialtechnik
der Rheinisch -Westfälischen Technischen Hochschule Aachen

zur Erlangung des akademischen Grades eines
Doktors der Ingenieurwissenschaften

genehmigte Dissertation

vorgelegt von **Diplom-Ingenieur**

Vladimir A. Ivanov

aus Moskau / Russland

Berichter: Univ.-Prof. Dr.rer.nat. Günter Gottstein
Priv.-Doz. Dr.rer.nat. Dmitri A. Molodov
Prof. Dr.rer.nat. Lazar S. Shvindlerman

Tag der mündlichen Prüfung: 13. Januar 2006

Note of thanks

I am grateful to my PhD thesis advisor Prof. Dr. rer. nat. Günter Gottstein, director of the Institut für Metallkunde und Metallphysik (IMM) at the RWTH University Aachen, for giving me the opportunity to carry out this work and for keeping his faith in my scientific work.

Lots of thanks to my mentor, the leader of the interface dynamics group of the IMM, Dr. rer. nat. Dmitri A. Molodov for supporting me over the years, his friendly encouragement and stimulating discussions on various scientific and personal issues.

I would like to thank Prof. Dr. Lazar S. Shvindlerman for his valuable discussions and suggestions.

I would also like to thank Doc. Dr. hab. Witold Łojkowski, head of the Laboratory of Nanomaterials (NL) of the Institute of High Pressure Physics at Polish Academy of Sciences, for cooperative work and useful discussions. I would like to thank all colleagues at NL, whom I met during my stay there, especially Dmitri Kolesnikov for his invaluable help in carrying out experiments at high gas pressure.

Many thanks are due to Prof. Dr. Anthony D. Rollett, Professor of Materials Science and Engineering at the Carnegie Mellon University, for fruitful discussions and his interest in my scientific work.

I was happy to be a member of the interface dynamics group at the IMM, and I would like to thank members of this group, Peter Konijnenberg, Dirk Kirch and Dorothea Mattissen, for their friendly assistance and the number of useful discussions.

I am deeply thankful to my students Tatiana Gorkaya, Jenny Rudnizki, Gerrit Esch. I would like to thank my student assistant Tatiana Gorkaya for her help and permanent assistance. Her creativity and hard work are highly appreciated. My deepest thanks go to Tatiana for inspiration and encouragement.

Many thanks are due to the IMM mechanical workshop team, especially Erich Hoffmann, Detlef Fuchs, Gerd Schütz and Alex Teschner for their help in manufacturing experimental devices.

I would also like to express my gratitude to all my colleagues at the IMM. I like to name Hao Chen, Syed Badirijjaman, Talal Al Samman, Luis Antonio Barrales Mora, Emmanuel Jannot and Prasad Gurla.

Help of Andreas Borgardt in solving mathematical problems and friendly debates are greately appreciated. Special thank goes to Alexei Zhdanov for careful proof reading.

I am thankful to Sergej Laiko for his friendly support and constant encouragement during my stay in Germany and after my leave to the USA.

Many thanks are to Peter Konijnenberg. Ample discussions are well remembered and appreciated.

I acknowledge helpful discussions with Prof. Dr. Yuri Mishin, Professor of the Department of Physics and Astronomy at George Mason University, and Dr. John W. Cahn, Senior Fellow of the Materials Science and Engineering Laboratory at the National Institute of Standards and Technology (NIST), and their critical suggestions and comments which contributed to my deeper understanding of materials science.

Last but not the least my deepest gratitudes to my parents, Nadezda and Alexander Ivanov, for their love, encouragement and support throughout my life.

Preface

The properties of metallic materials are strongly influenced by the presence of internal interfaces. Grain boundaries, i.e. interfaces between differently oriented crystallites of the same phase (grains), play a significant role in many processes in materials and determine such characteristics of materials as strength, fracture, plasticity, electroresistance, corrosion resistance and many others.

The ability of grain boundaries to move is their most important property. The mobility of grain boundaries determines changes of microstructure during annealing which cause recrystallization and grain growth and, in turn, determine physical and mechanical properties of the materials. Polycrystalline materials are represented as an assemble of grains surrounded by boundaries. The grains are equal in their physical and chemical properties and vary in size and shape. The grain boundaries, however, are essentially different in structure and properties. An important feature of grain boundaries is the strong dependence of their thermodynamic and kinetic properties on the crystallographic characteristics, first of all, on misorientation between the adjoining grains and the spatial orientation of the grain boundary plane (grain boundary inclination). That is the reason why the characteristics of grain boundaries are so important for understanding of the fundamentals of microstructure evolution.

The contiguous arrangement of grains in a polycrystal requires that their interfaces be connected, i.e. form junctions, triple junction lines and quadruple junction points. Although the number of grain boundary triple junctions in polycrystals is comparable in order of magnitude with the number of grain boundaries, so far, all peculiarities of grain growth in polycrystals were traditionally attributed to the motion of grain boundaries and the role of triple

junctions was reduced to characterize thermodynamically predicted equilibrium angles at the line where the boundaries meet. However, under certain circumstances grain growth in polycrystals can be controlled by the mobility of triple junctions.

Studies on polycrystals can only yield the averaged data on grain boundary and triple junction properties. The specific problems of microstructure evolution – structural, impurity, pressure and driving force dependence of grain boundary and triple junction mobility can, therefore, be addressed only in experiments and atomistic computer simulations on *individual* grain boundaries and triple junctions.

Despite of the numerous investigations on grain boundary migration, the physical mechanisms underlying this process are still obscure. It is worth emphasizing that the current understanding of the fundamentals of grain boundary migration, such as the relationship between grain boundary structure and mobility, the effect of solutes, shear stress and magnetic field on grain boundary mobility, is still far from forming a generalized theory of grain boundary migration.

Addressing above issues determined the goals and directions of experimental studies performed over the last five years in the Interface Dynamics Group of the Institut für Metallkunde und Metallphysik der RWTH Aachen. In the present manuscript we attempt to shed light on some unsolved questions and present the recent achievements in the experimental research on grain boundaries and triple junctions.

Outline of this work:

In Chapter 1, the fundamentals of grain boundaries, including their structure and energy, and grain boundary migration are presented.

In Chapter 2, experimental techniques are discussed. In particular, bicrystal and tricrystal growth methods, specimen fabrication and measuring equipment are reviewed.

Chapter 3 is dedicated to studies of the influence of grain boundary orientation on migration of curved grain boundary in bicrystals of aluminum.

Chapter 4 presents the results of the studies of interactions between the moving grain boundary and the external crystal surface. Potential drags of the "surface" triple junction and of the thermal groove are analyzed. Anisotropy of the external crystal surface and its effect on grain boundary motion are comprehensively discussed.

Chapter 5 treats migration of connected grain boundaries (grain boundaries with a triple junction) in aluminum doped by magnesium. The impact of solute atoms of magnesium on grain boundary and triple junction mobilities is studied.

Chapter 6 introduces a new experimental method to determine one of the fundamental characteristics of grain boundaries – the free volume of grain boundary. The thermodynamic approach utilized in this method and its peculiarities are reviewed.

The Appendices contain the reference information on the purity of used materials, the orientation of studied bi- and tricrystals and analysis of experimental errors.

Contents

Chapter 1

Theoretical background and previous studies

1.1 Structure and energy of grain boundaries

1.1.1 Introduction and definitions

Grain boundaries are the lattice defects which have been known for a long time, but are still least understood. A grain boundary separates two regions of the same crystal structure but of different orientation. In 3-dimensional space a general grain boundary has eight degrees of freedom or eight quantities which are required to unambiguously define it. Three values are required to specify the orientation difference between the adjacent grains, for instance the Euler angles φ_1, Φ, φ_2 , two values are required to specify the spacial orientation of the boundary plane by means of the normal to the grain boundary plane $\mathbf{n} = (n_1, n_2, n_3)$, with respect to one of the grains (keeping in mind that $|\mathbf{n}| = 1$). In addition to these five macroscopic degrees of freedom, there are three independent microscopic values of the translation vector $\mathbf{t} = (t_1, t_2, t_3)$.

The properties, in particular the mobility and energy of a grain boundary are, in principle, functions of all eight parameters. However, only five of these eight can be impacted externally, i.e. the disorientation between the adjoining grains and the spatial orientation of the grain boundary plane. The translation vector is constrained by the atomic nature of the crystals so as to minimize the total energy. To determine the dependence of grain boundary properties, for instance, the mobility, on the 5 macroscopic parameters, it would be necessary to keep all parameters but one fixed to systematically

vary that free parameter.[1] In reality, only few of these external parameters are varied, and usually this is the disorientation in terms of a fixed rotation axis and a variable rotation angle, and for a given rotation axis and a rotation angle, the inclination of the grain boundary plane with respect to a reference position.

The orientation relationship between two crystal lattices is a transformation which has to be applied to one of the crystals to make both crystal lattices coincide. If a common origin is assumed, this transformation is a pure rotation, since the relative positions of crystal axes in both crystals are the same. There are many ways to define a rotation, the easiest way is to represent a grain boundary by the rotating in terms of an axis <hkl> and angle θ of rotation. If the grain boundary plane is perpendicular to the rotation axis (Fig. 1.1a), the boundary is referred to as a *twist* grain boundary. In that case the choice of a grain boundary plane is unambiguous and does not depend on the rotation angle θ. In contrast, if the rotation axis is parallel to the boundary plane, the grain boundary is called a *tilt* boundary. Since there is an infinite number of possible boundary planes parallel to a given direction, there is an infinite number of tilt grain boundaries for a given rotation angle. The simplest type of grain boundaries are *symmetrical* tilt grain boundaries (Fig. 1.1b), where two grains of both sides of the boundary are related by symmetrical rotation around an axis in the boundary plane. In other words, the adjacent crystals 1 and 2 are mirror images of each other, and the boundary plane is the symmetry plane. All other tilt boundaries are called *asymmetrical* tilt grain boundaries (Fig. 1.1c).

1.1.2 Grain boundary structure and energy

Low angle grain boundaries

If the rotation angle θ between two adjacent grains is small, the entire boundary is comprised of a periodic set of crystal dislocations. The symmetrical tilt grain boundary consists of a single set of dislocations with the Burgers vector b (Fig. 1.2a). The number of dislocations per unit length in the grain boundary, $1/D$, increases with misorientation angle θ

$$\frac{1}{D} = \frac{2sin(\theta/2)}{b} \approx \frac{\theta}{b}, \tag{1.1}$$

[1] It is to note, that in recent works [1, 2] energy distribution of grain boundaries was measured as a function of all 5 macroscopic parameters

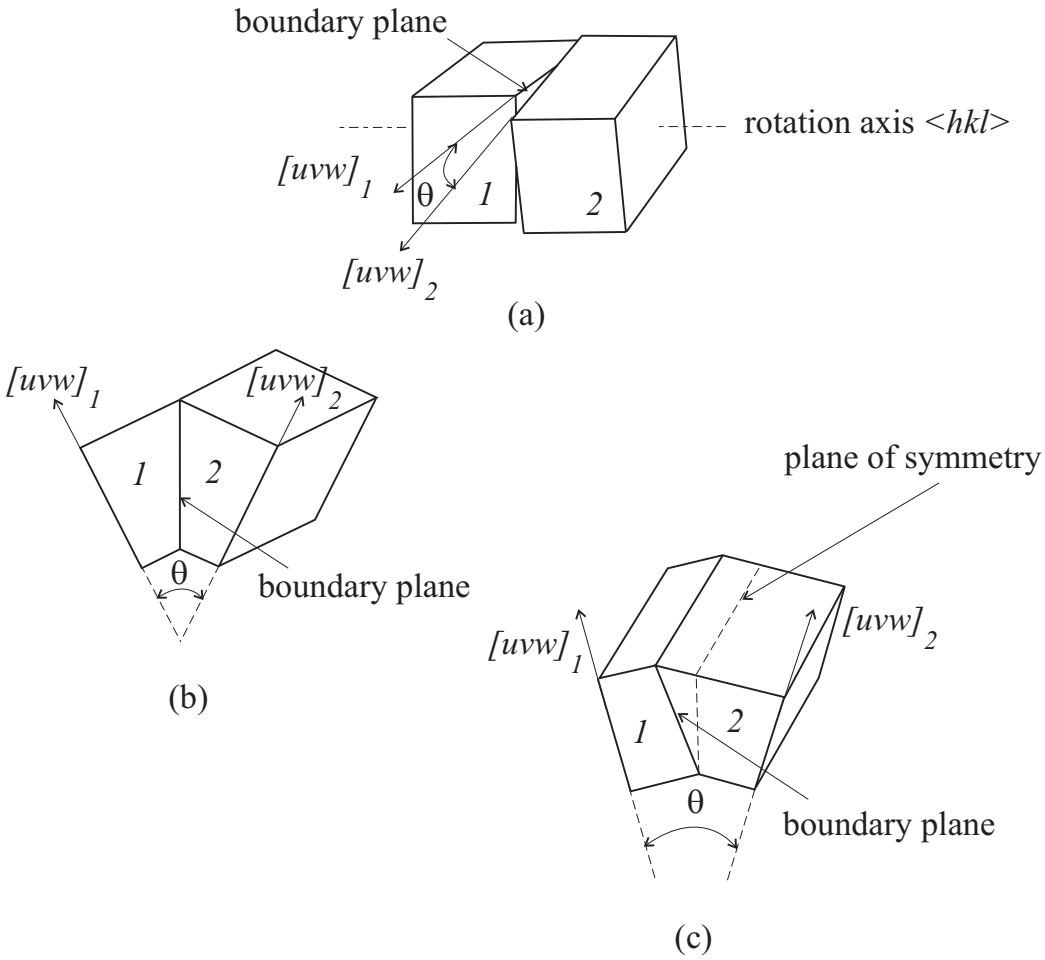

Figure 1.1: Various types of grain boundaries. (a) twist boundary, (b) symmetrical tilt boundary, (c) asymmetrical tilt boundary

where D is the distance between the grain boundary dislocations. If the symmetrical tilt boundary is turned of its symmetrical position by rotating it about the tilt axis through an angle ϕ (Fig. 1.2c), this boundary becomes an asymmetrical tilt boundary (Fig. 1.1c). The angle ϕ between grain boundary plane and symmetry plane is the inclination angle. As pictured in Fig. 1.2b, the boundary makes an angle $\phi - 1/2\ \theta$ with direction [100] in grain 1 and $\phi + 1/2\ \theta$ – in grain 2. In a special case ($\phi = 0$ or $\phi = 1/2\ \pi$) one obtains symmetrical grain boundary (Fig. 1.2a). For an asymmetrical grain boundary, at least two sets of dislocations are required (Fig. 1.2b). General boundary requires three sets of dislocations. The number of dislocations of each set can be calculated. In particular, for the asymmetrical tilt grain boundary the number of dislocations with Burgers vectors b_1 and b_2 (Fig. 1.2b) is given by

$$\frac{1}{D_2} = \frac{b_2}{\theta \sin \phi}, \tag{1.2}$$

whereas the number of dislocations in the original set is reduced to

$$\frac{1}{D_1} = \frac{b_1}{\theta \cos \phi}. \tag{1.3}$$

As a result, new dislocations increase the free energy of the boundary sharply as ϕ increases from zero since they are far apart.

The free energy of a low angle grain boundary can be calculated exactly. The stress field of a dislocation in an infinite periodic arrangement is confined to a range in the order of the dislocation spacing, D [3]. The energy of an edge dislocation per unit length is given by

$$E_d = \frac{\mu b^2}{4\pi(1-\nu)} \ln \frac{d}{r_0} + E_c, \tag{1.4}$$

where ν is the Poisson ratio, μ is the shear modulus, $r_0 \approx b$ is the radius of dislocation core, E_c is the energy of dislocation core. For a symmetrical tilt grain boundary with the tilt angle θ the energy per unit area is given by

$$\gamma_{gb}^{symm} = \frac{\theta}{b} \left(\frac{\mu b^2}{4\pi(1-\nu)} \ln \frac{1}{\theta} + E_c \right) = \theta(A - B \ln \theta), \tag{1.5}$$

where $A = E_c/b$ and $B = \mu b / 4\pi(1-\nu)$.

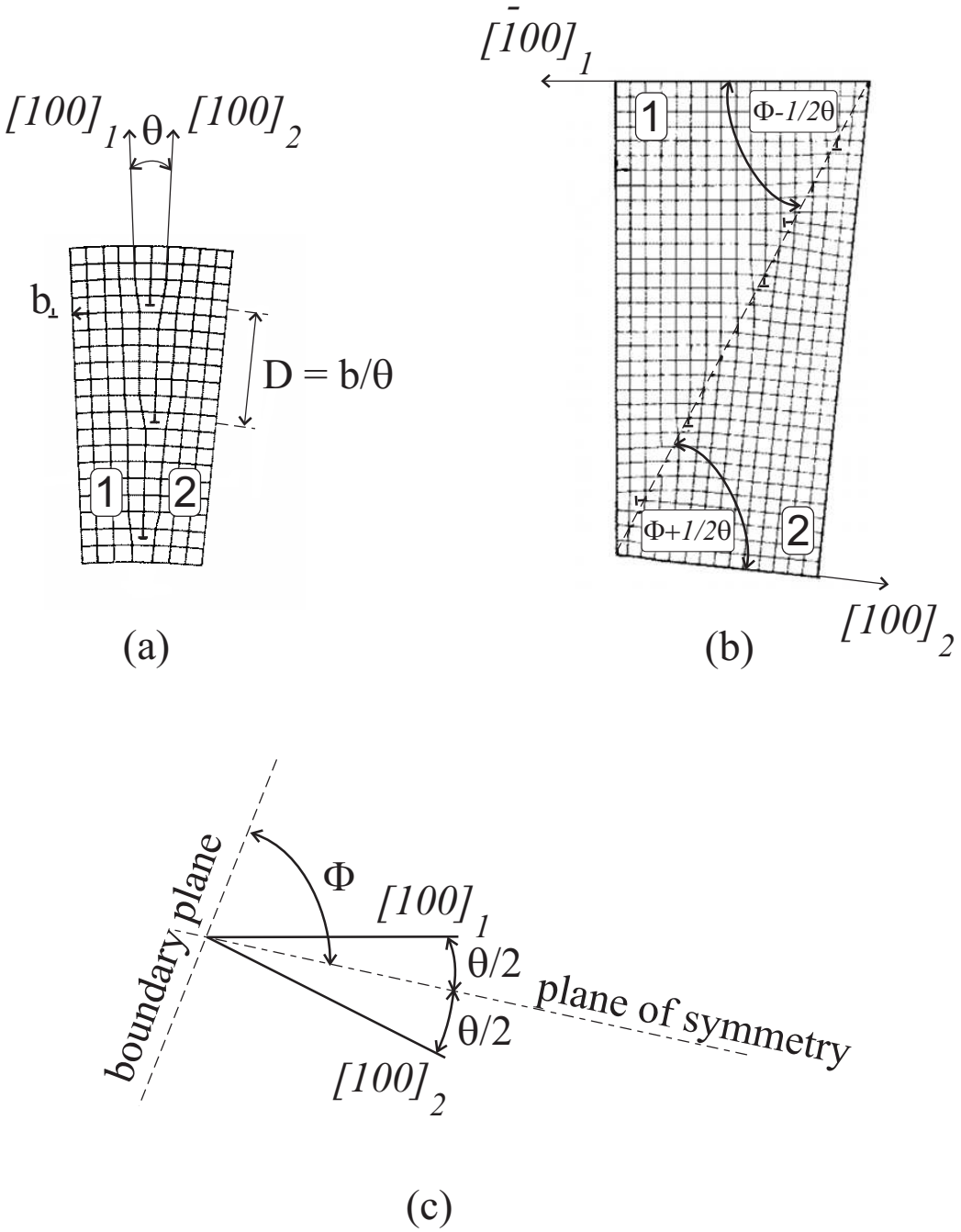

Figure 1.2: Lattice dislocations in (a) symmetrical and (b) asymmetrical tilt low angle boundaries. (c) Rotation angle θ and inclination Φ of asymmetrical boundary

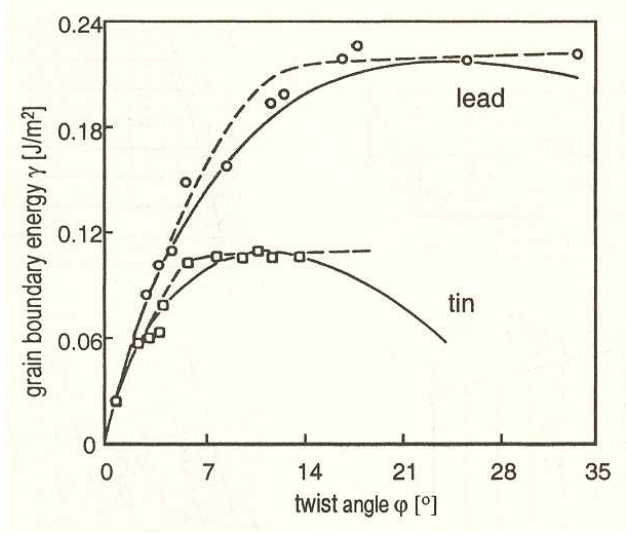

Figure 1.3: Measured (points and dashed line) and calculated (using dislocation theory) grain boundary energy vs. misorientation angle [4]

High angle grain boundaries

No further change of the grain boundary energy was revealed with increasing the rotation angle in excess of 15° (Fig. 1.3). Contrary to these results, the dislocation model predicts energy decrease for large angles of rotation because the dislocation cores tend to overlap [5]. The dislocations lose their identity as individual lattice defects and, thus, the dislocation model becomes unphysical and an alternative description of high angle grain boundaries is required.

Modern understanding of the structure of high angle grain boundaries is based on dislocation models of low angle grain boundaries and atomistic computer simulations. Firstly, we consider two methods for the description of grain boundary structure related to the previous dislocation models. These are so called O-lattice and Coincident Site Lattice/Displacement Shift Complete (CSL/DSL) descriptions of the grain boundary structure.

Bollmann developed a technique for analyzing the structure of interfaces that is quite general and has a number of useful properties [6]. This method is based on the concept of the O-lattice, which describes the matching and mismatching of neighboring lattices at the interface. Let us consider two

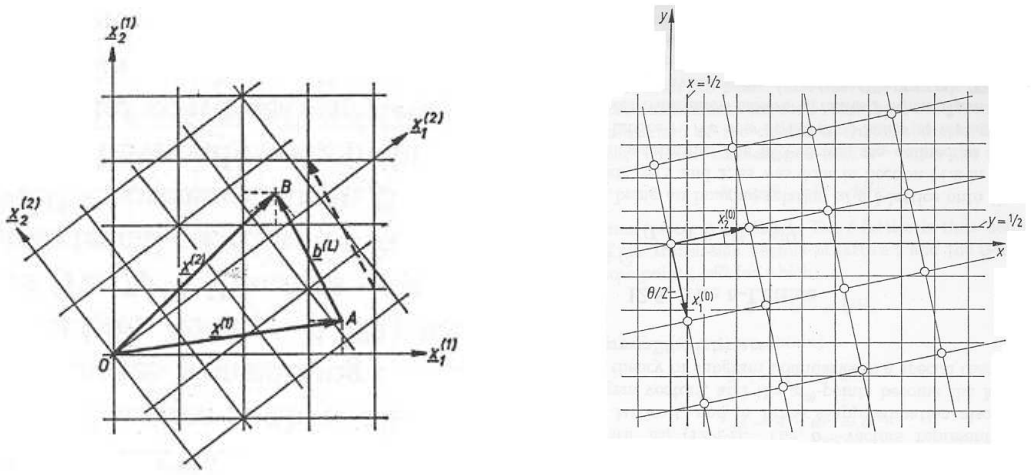

Figure 1.4: (a) Coincidence of cell elements of adjoining lattices $x^2 = Ax^1$. (b) Construction of O-lattice

misoriented crystal lattices, specified as 1 and 2 (Fig. 1.4a). Both lattices form a periodic set of points in space, where, for each point, the internal coordinates in a cell of lattice 1 are identical with the internal coordinates of a cell of lattice 2. This set of points defines Bollmann's O-lattice. It should be underlined that, generally, the crystal lattice nodes do not coincide with the O-lattice points (Fig. 1.4b). The basic equation of the O-lattice theory is

$$b^{(l)} = (I - A^{-1})x^O, \tag{1.6}$$

where x^O is the O-lattice vector, b^l is the translation vector of lattice 1 (Fig. 1.4a), A is the transformation (rotation) matrix, which transforms lattice 1 into 2. Eq. (1.6) gives O-lattice vectors in terms of the vectors of crystal lattice 1.

The physical interpretation of O-lattice in terms of grain boundaries is that the O-points in Eq. (1.6) are points of geometrical registry, which have minimum strain, between crystal lattice 1 and 2. Between these O-points the disregistry accumulates and reaches the value b^l at a neighboring O-point. Thus, the misfit between any O-points is concentrated in planes between the O-points. The O-lattice theory provides a convenient mathematical method for describing possible dislocation structures between two arbitrary lattices.

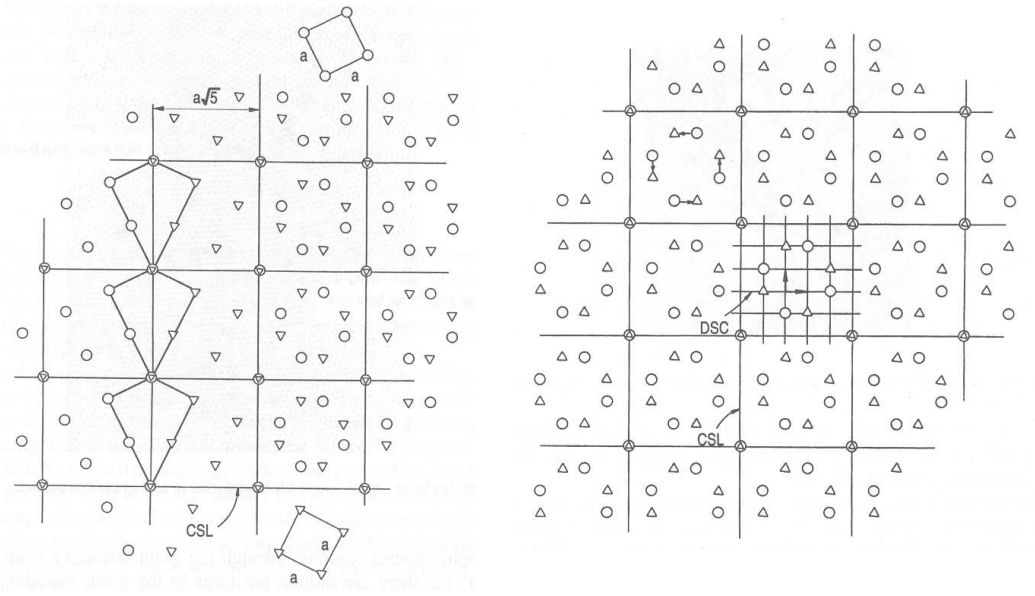

Figure 1.5: (a) Coincidence site lattice of 36.9° <110> (Σ=5) boundary in a cubic crystal lattice. Left side of figure: tilt boundary, grain boundary plane is perpendicular to the plane of page; right side of figure: twist boundary, grain boundary plane is parallel to the plane of page. (b) Displacement shift complete lattice and coincidence site lattice at 36.9° <100> rotation in a cubic lattice

The O-lattice is a useful technique, but it cannot predict certain aspects of interfacial structure, such as ledges and partial dislocations. An alternative method to quantify the structure of interfaces is provided by the CSL/DSL lattice constructions. Let us consider two identical interpenetrating 3-dimensional lattices which are rotated from initial coincidence position. There are always orientation relationships where crystallographic planes continue through the boundary from one crystal to the other. Thus, there are atomic positions in the boundary which coincide with ideal positions of both crystal lattices. Such lattice points are called *coincidence sites*. An example of the coincidence site lattice (CSL) is given in Fig. 1.5a. A rotation of one of cubic lattices of 36.87° around a <100> generates a periodic set of coincidence sites – the coincidence site lattice. The density of coincidence sites

is described by the function

$$\Sigma = \frac{\text{volume of elementary cell of CSL}}{\text{volume of elementary cell of crystal lattice}}. \tag{1.7}$$

For 36.87° <100> rotation is $\Sigma = \frac{a(\sqrt{5})^2}{a^3}$=5. Grain boundaries between crystallites which have an orientation relationship corresponding to a high density of coincidence sites are called CSL boundaries or special boundaries. The smaller the Σ, the more ordered the grain boundary. Low angle grain boundaries can be characterized by Σ=1, since almost all lattice nodes, except for the atoms of the dislocation cores, are coincidence sites.

Note that O-lattice model can be used for mathematical description of the CSL lattice since any lattice vector of the CSL is the solution x^O of the O-lattice equation Eq. (1.6). However, not all O-lattice vectors x^O are CSL vectors.

The application of the CSL concept to real boundaries is difficult. There is a fundamental problem that the coincidence site lattice occurs for very special rotations and Σ does not change continually with the angle of rotation. Geometrically, high angle grain boundaries can be treated as small deviations from the nearest CSL. They are then similar to low-angle grain boundaries, where small deviations from the perfect single crystal are compensated by lattice dislocations. Any deviations from a CSL are accommodated by lines of dislocations in between regions of undistorted CSL. These dislocations are called secondary grain boundary dislocations (SGBD) and the boundary between them is the perfect CSL boundary generated by the periodic arrangement of primary (lattice) dislocations. Burgers vector of SGDB is a translation vector of the DSC lattice. As a result, the DSC lattice is a coarsest grid which contains all lattice points of both crystal lattices (Fig. 1.5b).

The most sophisticated and effective method to study grain boundary structure are atomistic simulations. The main purpose of the atomistic studies of grain boundary structure is to relate the structure to other grain boundary properties. Two important fundamental insights were provided by the atomistic calculations of the structure and energies of grain boundaries in metals. Firstly, it was shown that the structure of grain boundaries can be described as being composed of several periodic structural (polyhedral) units [7]. Secondly, it was shown, that the grain boundary energy is directly correlated with the free volume of grain boundary (and with the boundary structure, accordingly). This subject is examined in greater details in Chapter 6.

1.2 Grain boundary motion

1.2.1 Fundamentals

Until now there is no unified theory of grain boundary migration. For a long time theoretical descriptions of migration of high-angle grain boundaries were based on the rate theory of atoms crossing the boundary.[2] This theory is overdated, but due to its simplicity and widespread use we discuss it here.

It is tacitly assumed that the atom diffuses through the boundary by the simple "vacancy-atom" exchange mechanism considered in [8] and the grain boundary motion is reduced to the diffusive motion of atoms across the boundary. It is also assumed that the boundary can be crossed by a single atomic jump and each transferred atom displaces the boundary by the diameter of an atom, b. The grain boundary velocity is given by

$$v = b\left(\Gamma_+ - \Gamma_-\right), \tag{1.8}$$

where Γ_+ and Γ_- are the jump frequencies in the opposite directions. If there is no Gibbs free energy difference between the neighboring grains, the atomic flux $(\Gamma_+ - \Gamma_-) = 0$, and the boundary will not move. If the Gibbs free energies of the grains are different then the driving force for grain boundary migration appears as

$$P = -\frac{dG}{dV}. \tag{1.9}$$

Each atom of volume $\Omega_a \approx b^3$ will gain the free energy Pb^3 if it detaches from the shrinking grain and subsequently attaches to the growing grain. But it has to increase the free energy when moving in the opposite direction. The free energy variation across the boundary is shown in Fig. 1.6. The velocity of a grain boundary is the displacement per unit time due to the difference of thermally activated diffusional jumps from the shrinking to growing grain

$$v = b\left(\nu_+ \exp\left(-\frac{G_m^+}{kT}\right) - \nu_- \exp\left(-\frac{G_m^- + Pb^3}{kT}\right)\right). \tag{1.10}$$

If the atom oscillation frequencies $\nu_+ = \nu_- \approx \nu_D$, where ν_D is Debye-frequency, and the migration free energy G_m is the same in both jump direc-

[2] The only known exception was the motion of twin grain boundaries which does not involve any diffusion

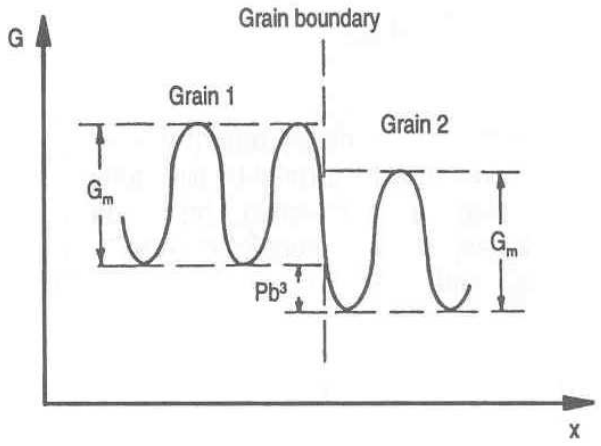

Figure 1.6: Schematic free energy curve at a grain boundary

tions, Eq. (1.10) takes the following form

$$v = b\nu_D \exp\left(-\frac{G_m}{kT}\right)\left(1 - \exp\left(-\frac{Pb^3}{kT}\right)\right). \tag{1.11}$$

In all practical cases, including recrystallization in heavily cold worked metals, because of the small driving forces $Pb^3 \ll kT$ [9] and, thus,

$$\exp\left(-\frac{Pb^3}{kT}\right) \cong 1 - \frac{Pb^3}{kT}, \tag{1.12}$$

which yields

$$v = \frac{b^4 c_v \nu_D}{kT} \exp\left(-\frac{G_m}{kT}\right) \cdot P \equiv m \cdot P, \tag{1.13}$$

where m is referred to as the grain boundary mobility. The relation between grain boundary mobility and diffusion of jumps through the grain boundary is given by Nernst-Einstein equation

$$m = \frac{b^2 D_m}{kT} = \frac{b^2 D_0}{kT} \exp\left(-\frac{Q_m}{kT}\right) = m_0 \exp\left(-\frac{Q_m}{kT}\right), \tag{1.14}$$

where D_m is the diffusion coefficient for diffusion jumps through the boundary, D_0 and Q_m are the pre-exponential factor and the activation enthalpy, respectively.

It has been recently shown that the volume "swept" by a moving grain boundary undergo a shear [10, 11] and the grain boundary motion is coupled to tangential translation of the grain. It was found that there is a big class of high-angle grain boundaries which move by deformation of their structural units, accompanied by relatively small and highly correlated displacement of the atomic sites. During the motion of the grain boundary the atoms can diffuse but must eventually settle on geometrically prescribed sites once the boundary has passed. However, diffusion and coupled motion does not exclude each other.

1.2.2 Driving force for grain boundary migration

A driving force for grain boundary migration appears if the boundary displacement leads to the decrease of the total free energy. The driving force is conceptually equivalent to the pressure – force acting per unit area of a grain boundary, it has the dimension of energy per unit volume. In principle, the gradient of any intensive thermodynamic variable offers a source of the driving force: the gradient of temperature, pressure, density of defects, density of energy, magnetic field strength. It is obvious that not all theoretically possible driving forces can be realized experimentally. The detailed report on different types of driving forces utilized in grain boundary migration experiments was done by Gottstein and Shvindlerman in their book [9]. Present work exclusively focuses on the steady-state motion of *curved* grain boundaries, therefore, we restrict our review to the capillary driving force only.

The most frequently used method to study grain boundary motion in bicrystals is the displacement of curved grain boundary. In this case the driving force is provided by the reduction of the boundary area. Several bicrystal geometries were designed to move a boundary with a constant driving force (Fig. 1.7). A constant driving force in our experiments is provided by the energy γ_b of the grain boundary. Let us consider the motion of initially symmetrical grain boundary with rotation axis <hkl> and angle of misorientation θ in quarter-loop configuration (Fig. 1.8). The free energy of the system in a quasi-two dimensional approximation can be represented as the sum of boundary and surface energies. In this case, the reduction of the

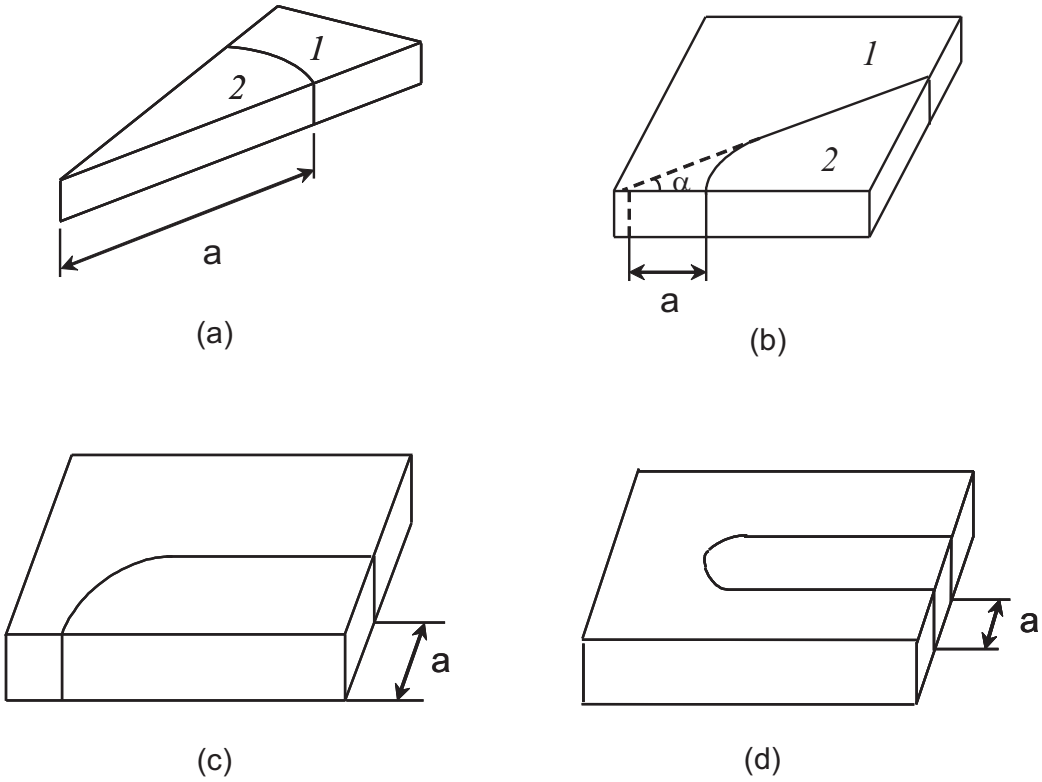

Figure 1.7: Grain boundary geometries for grain boundary motion with a controlled driving force. (a) Wedge technique [12] ($P = \gamma_b/a$), (b) reversed-capillary technique [13] ($P = \gamma_b/a \cdot f(\alpha)$), (c) quarter-loop ($P = \gamma_b/a$) and (d) half-loop [14] ($P = 2\gamma_b/a$)

free energy due to grain boundary migration can be written as

$$-\Delta G = \int_{x_1}^{x_1^*} \left[2\Delta\gamma^s y(x) + \delta\gamma_b\sqrt{1-y'(x)}\right] dx - \delta\Delta\gamma_L^s\Delta x, \qquad (1.15)$$

where $\Delta\gamma_s = \gamma_1 - \gamma_2$ and $\Delta\gamma_s^L = \gamma_1^L - \gamma_2^L$ are the differences in (specific) free energy of top/bottom and of lateral surfaces of specimen, respectively, γ_b is the grain boundary energy, $\Delta x = x_1^* - x_1$ is the boundary displacement, $y(x)$ is a function describing the shape of the grain boundary, δ is the specimen thickness.

Since the shape of the grain boundary does not change during its steady-

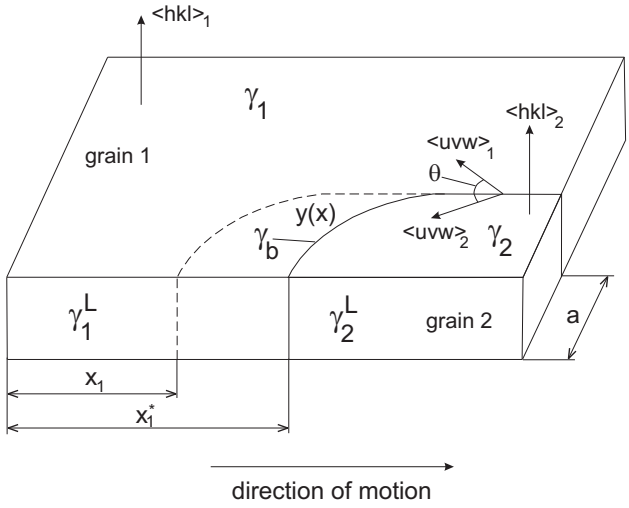

Figure 1.8: Quarter-loop bicrystal geometry utilized for measurements of grain boundary motion under a constant driving force. The solid line represents the current, the dashed line a prior grain boundary location

state motion, the volume of the grain 2, which is "swept" by the moving grain boundary, is given by

$$V = \delta \cdot a \cdot \sqrt{1 - y'(x)}, \tag{1.16}$$

where, a is the width of the shrinking grain. Usually, $\Delta\gamma_s$ and $\Delta\gamma_s^L$ tend to zero (for instance, for the motion of initially *symmetrical* tilt grain boundary (Fig. 1.8)) and can be neglected. Thus, Eq. (1.15) can be simplified and the driving force can be written as

$$P = -\frac{\Delta G}{\Delta V} = \frac{\gamma_b}{a}. \tag{1.17}$$

The curved grain boundary implies that its structure changes along the boundary, since it is composed of different grain boundary planes. It is worth emphasizing that the averaged velocity over different grain boundary planes is measured in experiments. Therefore, the obtained mobilities cannot be related to a specific grain boundary structure.

Since the exact magnitude of the boundary energy in not known, we use the *reduced* boundary mobility

$$A_b \equiv v \cdot a = m \cdot \gamma_b. \tag{1.18}$$

The reduced mobility is the product of mobility and grain boundary energy. Thus, it also reflects the orientation and temperature dependence of the grain boundary energy. According to computer simulations and experimental studies, the grain boundary surface tension may change by 20% or less but the reduced grain boundary mobility may change a factor of 10 and more. Therefore, the change of the grain boundary surface tension can be neglected. The activation parameters of boundary migration can be obtained from measurements of the reduced mobility and the mechanisms of grain boundary migration can be explored.

1.2.3 Drag effect during grain boundary motion

The moving grain boundary always interacts with other imperfections in the crystal. This interaction affects the grain boundary motion. Such imperfections can be vacancies, dislocations, triple junctions, external crystal surfaces. Various types of interactions were treated by Gottstein and Shvindlerman comprehensively in their book [9].

In the present work we consider only some of them in detail. The interaction of the moving grain boundary and the external surface of a specimen (drag effect of "surface" triple junction, groove dragging and effect of outer surface anysotropy on grain boundary motion) is discussed in Chapter 4. Impurity and triple junction drag are addressed in Chapter 5.

Chapter 2

Measurement of grain boundary mobility

The grain boundary migration determines to a large extent many technological processes in materials in which recrystallization and grain growth are involved. Thus, it seems reasonable to extract data on grain boundary motion, i.e. the grain boundary mobility, considering temporal evolution of the grain size during recrystallization or grain growth in polycrystals. However, these data fail to explain physical processes underlying grain boundary migration. Averaging over a large number of grains "spreads" the mobility over many different moving grain boundaries. As a result, the correlation between grain boundary properties and structure cannot be obtained from recrystallization and grain growth experiments. Many specific problems, i.e. correlation between kinetic properties of boundaries and their structure, effect of pressure, temperature, solute elements on the motion of grain boundaries, the influence of triple junctions on the grain growth kinetics, the mechanisms of grain boundary migration etc, cannot be studied in polycrystals. However, all of these problems can be addressed in bicrystal/tricrystal experiments.

2.1 Bicrystal/tricrystal method

The reliable and reproducible physical data on grain boundary and triple junction properties (diffusivity, mobility etc) can be obtained only by the bicrystal/tricrystal method. In particular, the experiments on the migration of individual grain boundaries and triple junctions are best realized

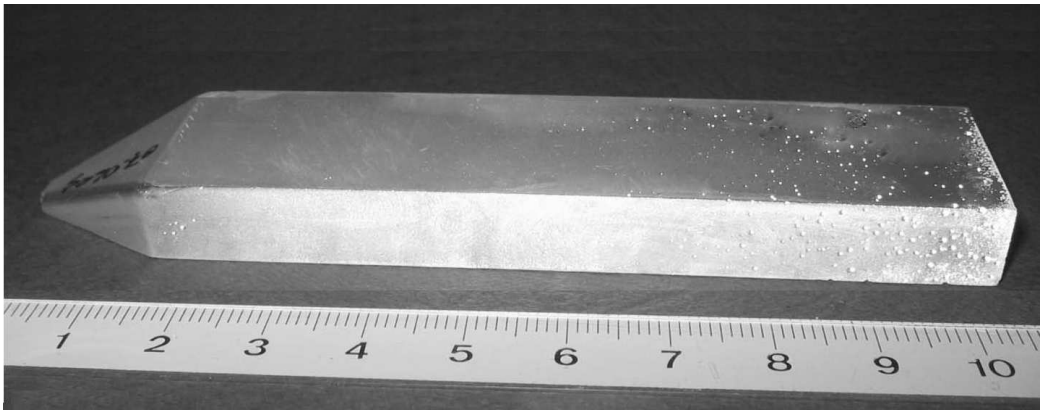

Figure 2.1: Aluminum single crystal grown by the Bridgman method (scale is given in cm)

in specially grown bicrystals/tricrystals. However, this method requires essential efforts to fabricate crystals with given and precise orientation and misorientation as well as to produce specimens for investigations in chosen experiemental techniques. The whole process of specimen fabrication can be separated into three consequent stages: the growth of oriented single crystals to use them as "seeds" for the growth of bicrystals/tricrystals, the growth of planar bicrystals/tricrystals with specified boundary(-ies), the production of specimens from grown planar crystals. Below we consider these three stages and the utilized experimental equipment.

2.1.1 Fabrication of planar bicrystals

As mentioned above, the first step is the fabrication of single crystals. Single crystals (Fig. 2.1) were grown using directional solidification method with the cooling seed in a vertical crucible (Bridgman method). Seeds were cut out of the massive single crystal to satisfy the orientation and misorientation requirements for the desired bicrystal. In order to avoid mechanical deformation the electrical discharge machine (EDM) was used for cutting. The crystallographic orientation of the massive single crystal was determined by the X-Ray Laue method with the accuracy of $\pm$ 0.1°. Since in the current work various problems of grain boundary migration were addressed, many different types of planar bicrystals/tricrystals were fabricated.

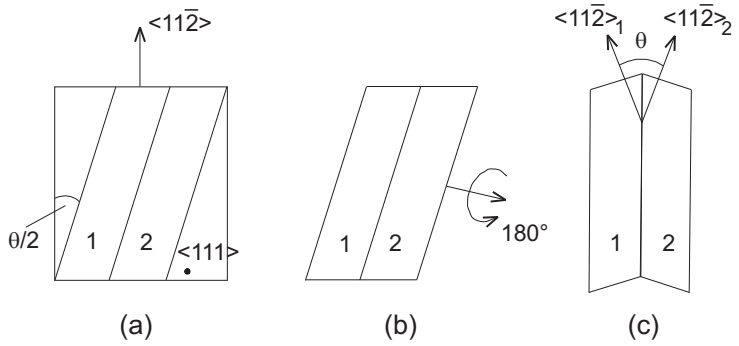

Figure 2.2: (a) Cutting procedure and (b) arrangement of single crystal seeds for the growth of bicrystal. (c) Grown bicrystal contains symmetrical tilt grain boundary with <111> rotation axis and misorientation angle θ

For the sake of simplicity we consider here only fabrication of single crystal seeds for bicrystals with a symmetrical <111> *tilt* boundary. The processing chain is shown in Fig. 2.2. Two identical seeds were cut out under the angle $\theta/2$ to the direction $<11\bar{2}>$ of initial single crystal. One of the seeds was rotated around the axis perpendicular to the surface of the cutting on 180°. After this operation the angle of misorientation between the two seeds is equal to θ. The seeds were connected with a planar polycrystal (Fig. 2.3) by welding together two contact ends of seeds and polycrystal using the specially designed SiC-hot stage for the local melting. The bicrystals were grown by directional solidification with the cooling seeds in horizontal crucible. Details of bicrystal growth are given elsewhere [15, 16]. The melted zone, however, might have different welding defects like porosity and solidification cracking. Any of these defects are potentially disastrous as they can affect the nucleation of undesirable grains. The roughness of the external surface also provides nucleation sites for unwanted grains. To reduce the risk of nucleation of new grains the area behind the melted zone has to be shrunken by cutting out the "growth-help" slit separating two seeds (Fig. 2.3c) and the external roughness has to be smoothed out. The grown bicrystal (Fig. 2.3d,e) might be utilized for growing next bicrystal that will have the same misorientation. The final crystallographic orientation of each of the adjoining grains was checked again by the Laue method. After all operations of electrical discharged machining single and bicrystal specimens were etched in a solution of 18 ml HCl, 9 ml HNO_3, 2 ml HF to remove the deformed surface layer.

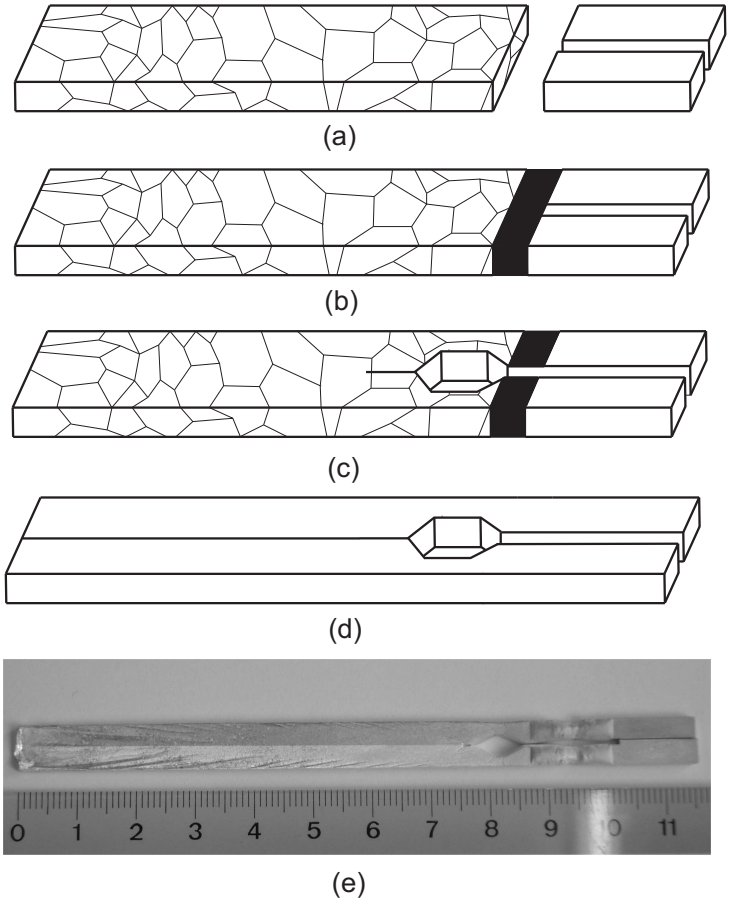

Figure 2.3: (a)-(d) Fabrication process of planar bicrystal, (e) grown Al-bicrystal (scale is given in cm)

2.1.2 Fabrication of planar tricrystals

There is no principal difference between fabricating of bicrystals and tricrystals. Therefore, we only show here the processing chain for planar tricrystals (Fig. 2.4). It is necessary to underline that the width of the middle grain, which is important for experiments, can be roughly achieved by adjusting the gap between two "growth-help" slits (Fig. 2.4c). As in the case of bicrystals, the Laue method was used to examine the final crystallographic orientation of the neighboring grains.

2.1.3 Manufacture of specimens for the study of grain boundary migration

As mentioned before, the most frequently used bicrystal technique to study the boundary motion is the displacement of curved grain boundary under a capillary driving force.[1] Figs. 2.5a-2.5d show how a curved grain boundary was obtained experimentally in the present work. First, one grain was reduced in size 0.3-0.6 mm (Fig. 2.5b) since this size is the necessary condition for the right driving force. In the next step one corner of the smallest grain was cut off (Fig. 2.5c). During the annealing treatment, a curvature was automatically induced by the sloping specimen corner. As a result of the curvature the boundary migrates from right to left. During boundary motion grain 1 consumes grain 2.

Figs. 2.5e-2.5g show the sequence of steps in fabrication of the final specimen from the grown tricrystal. The V-shaped wedge is cut out of the specimen. Recently, it was proposed by Molodov to cut a slanting slit at the the tip of a V-shaped gap (Fig 2.5f). This improved procedure was applied in the present work. During the annealing treatment, both grain boundaries get a curvature and start moving toward the tip of the V-shaped gap forming a triple junction (Fig. 2.5g). As a consequence of the curvature of adjoining boundaries, the boundary system with a triple junction migrates, grain 1 and 3 consume grain 2.
Prior to experiments the specimens were mechanically ground and electrolytically polished to improve the surface quality.

[1] Studies of migration of connected grain boundaries, i.e. grain boundaries with a triple junction, can be performed only by utilizing curvature as a driving force

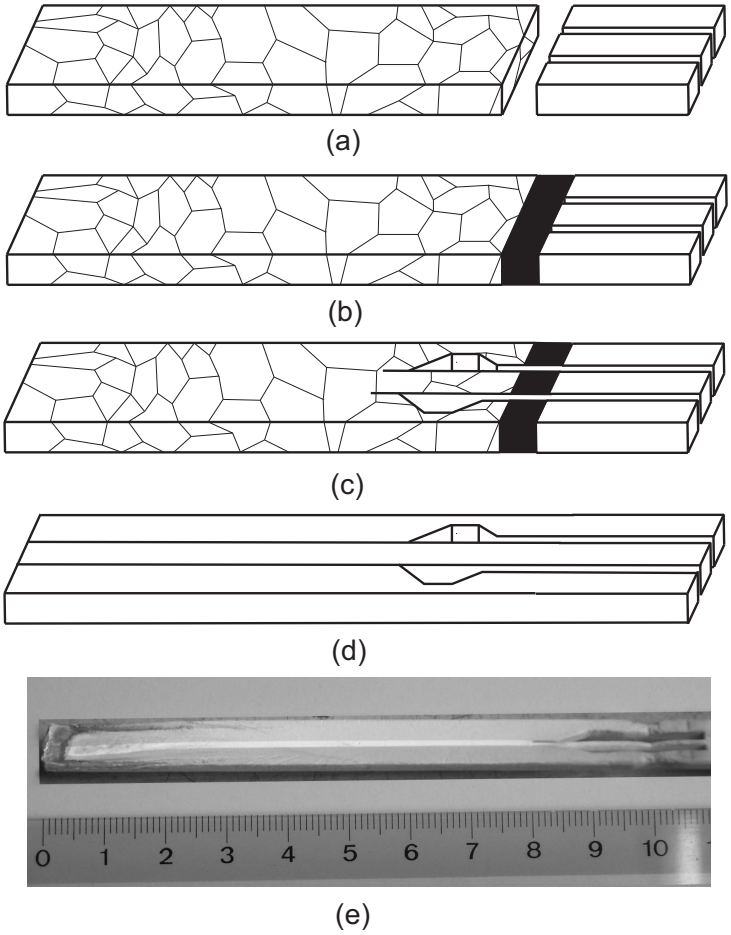

Figure 2.4: (a)–(d) Fabrication process of planar tricrystal, (e) grown Al-tricrystal (scale is given in cm)

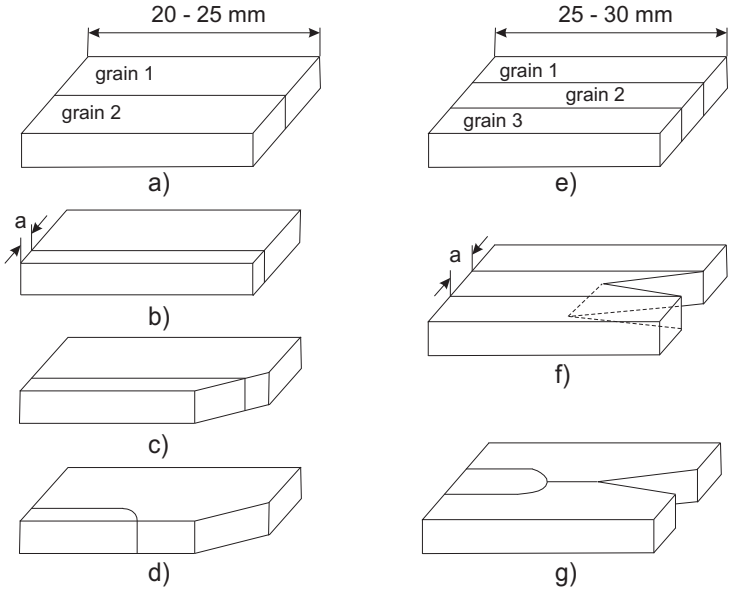

Figure 2.5: Sequence of the sample fabrication from (a)-(d) planar bicrystal and (e)-(f) planar tricrystal

2.2 Experimental technique

In order to determine the velocity of grain boundary motion the displacement of the macroscopic segment of the boundary in a time interval has to be measured. For this purpose the position of the grain boundary segment has to be located. There are two different methods to determine the position of a grain boundary: the discontinuous method and the continuous method.

In the discontinuous method the position of the boundary is determined after discrete time intervals by the position of the boundary groove at the crystals surface. The boundary groove can be observed under an optical microscope. The advantage of this method is its simplicity; the major disadvantage is that the velocity measured is averaged over a large time interval between successive observations.

In contrast, in the continuous method the position of the boundary is determined at any moment of time. The method requires automation of the procedure to locate the boundary position and therefore is more complicated than the discontinuous one. The determination of the grain boundary posi-

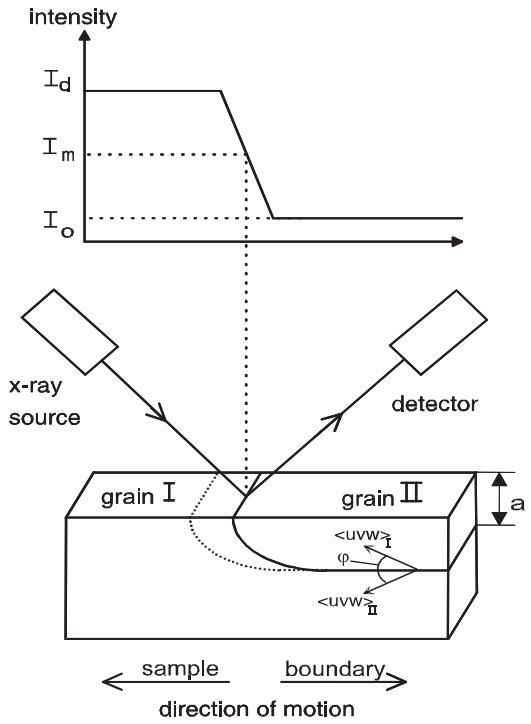

Figure 2.6: The change of intensity of a diffracted X-ray beam with displacement of the specimen relative to the X-ray spot.

tion is achieved by utilizing discontinuity of grain orientation at the boundary. Several different physical principles can be applied to determine the difference in crystal orientation.

In what follows, we consider comprehensively two techniques used in the present work: based on X-ray and backscattered electrons diffraction.

2.2.1 X-ray method for continuous tracking of moving interfaces in crystalline solids

A simple, precise and multi-purpose technique to track the location of a boundary uses X-ray diffraction. X-ray diffraction is very sensitive to the structure and orientation of crystalline materials and, therefore it is an excellent tool to distinguish the difference in crystal structure and crystal orientation. The principle of the method is shown in Fig. 2.6. A bicrystal

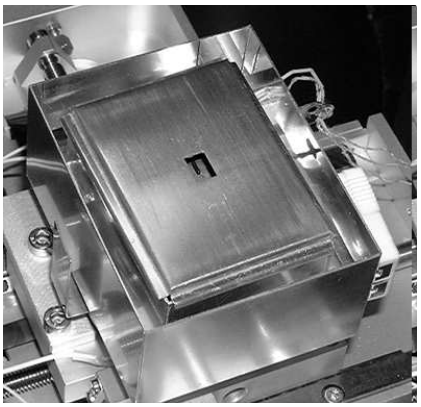

Figure 2.7: Electrical resistance oven for a SEM

specimen is placed in an X-ray goniometer such that one grain is in Bragg position. An X-ray scan across the boundary (generally speaking, interface) reveals a steep gradient of the reflected intensity. The maximum intensity I_d is measured as long as an X-ray spot solely located on the surface of grain I. If the spot is located on the grain boundary, the intensity of the reflected X-ray beam should be intermediate between I_d and I_0. I_0 is the intensity measured on the surface of grain II, which is not in Bragg position. When the boundary moves, the specimen must be displaced that the reflected intensity remains constant during the measurement. Thus, the velocity of the moving grain boundary is equal to the speed of specimen movement at any moment during the experiment. This procedure does not interfere with the process of boundary migration.

All major functions of the X-ray Interface Continuous Tracking Device (XICTD) are software controlled, enabling an automated data acquisition and data visualization. The measurable velocity ranges are from 1 to 1000 μm/s with a temporal resolution of 4 measurements per second. In Figs. 4.17-4.18 the distance – time diagrams are shown for the motion of curved grain boundary in Al-bicrystals under a constant driving force. The different hot stages designed for the XICTD allow to heat the specimens up to 1200°C in a gas atmosphere (nitrogen, argon); the temperature is kept constant within $\pm 0.3°$. The accuracy of the velocity measurements of grain boundary motion is better than 2%. Other details of the XICTD, like the range of application, measuring algorithms, sensitivity and accuracy, can be found in [15, 17].

2.2.2 In-Situ annealing procedure in the SEM

An X-ray based technique cannot visualize the shape of moving boundary. However, Electron Backscattered Diffraction is nowadays widely used for the investigation of grain structure evolution and in particular for grain boundary migration studies. Since the contrast by backscattered electrons (BSE) is very sensitive to orientation, the shape of moving grain boundary can be easily visualized in the scanning electron microscope (SEM). The hot stage set-up was purposely designed at the IMM some years ago for the study on grain boundary migration in the SEM [16]. To reduce the heat radiation and to protect the BSE-detector from overheating, the hot stage is surrounded by the double reflected walls (Fig. 2.7). Everhart-Thornley backscattered electron detector is used to obtain the orintation contrast. To obtain a high yield of electrons the hot stage with a specimen has to be tilted under 30°. The video frame grabber system by Point Electronics records a sequence of BSE-images with the scanning rate from 1 to 30 seconds per frame.

In the present work this technique was used to study the migration of grain boundaries with a triple junction. The recorded video frames are shown in Fig. 4.4 and Fig. 5.8. Post-processing of this recording provides all information to determine triple junction and grain boundary mobility: time dependence of triple junction displacement, the shape and radius of curvature of the moving boundaries. The electrical resistance oven allows to heat the specimens up to 640°C; the temperature is held constant within ±2° (in temperature interval 200-640° and constant press force applied to the specimen). A more detailed report on this technique is available in [16].

Chapter 3

Effect of grain boundary character on the motion of curved boundaries in Al-bicrystals

In this chapter effect of grain boundary character (grain boundary plane orientation) is explored for the particular case of steady-state boundary migration – motion of grain boundaries under a constant driving force in a quarter-loop geometry. Curvature driven motion of individual grain boundaries was experimentally studied. The curved boundary containes different boundary planes. Therefore, it is impossible to measure the effect of boundary inclination on the mobility utilizing boundary curvature as a driving force. However, the migration of boundaries with different sets of boundary planes comprising curved moving part can be measured and compared. In the present research, the motion of <111> boundaries which consist of *tilt* boundary planes (boundary elements) with various inclination and of *mixed* tilt-twist elements was studied.

3.1 Anisotropy of grain boundary mobility. General aspects and previous studies

Previous studies on bicrystals showed that the mobility of high angle grain boundaries depends on the rotation axis <hkl> and the angle of misorientation θ [18, 19]. The non-monotonic dependence of grain boundary mobility was also confirmed by computer simulations of grain boundary migration

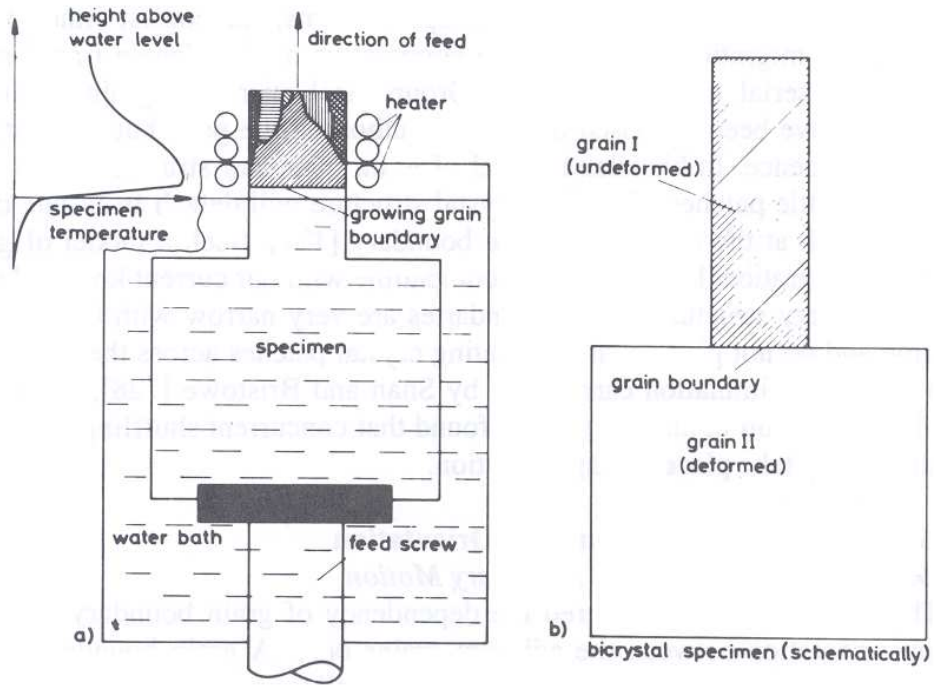

Figure 3.1: (a) Experimental set-up for the production of a bicrystal specimen from a deformed single crystal in a gradient furnace; (b) geometry of used bicrystal

performed using molecular dynamics [20, 21]. A grain boundary, however, is defined not only by misorientation between the adjacent grains, but also by the spatial orientation (inclination) of the boundary plane. As repeatedly mentioned, the motion of the grain boundaries under its own surface tension is frequently used to study grain boundary migration . Most bicrystal experiments, as well as computer simulations in [20], were conducted on curvature driven *tilt* grain boundaries, where the boundary inclination changes along the moving grain boundary. To simplify this problem, one is tempted to assume that the spatial orientation of grain boundary does not seriously affect grain boundary mobility. This is not always true and there is a pronounced evidence of the fact that some boundaries exhibit an anisotropy of mobility for a given misorientation relationship.

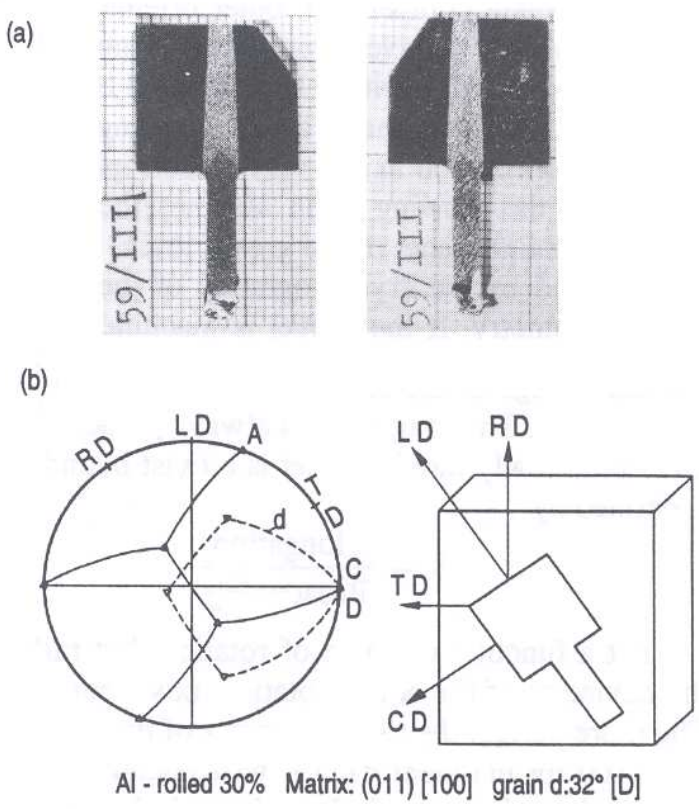

Figure 3.2: (a) Rectangular shaped planar growth of grain boundary with <111> rotation axis; (b) a shovel was cut in such a way that {111} plane is parallel to longitudinal direction

Anisotropic grain growth in aluminum was observed in experiments of Gottstein et al. [22] where boundary was allowed to freely expand to the deformed volume of the specimen (Fig. 3.1). A slightly deformed single crystal with the shape of a shovel was placed in a gradient furnace. Growth selection set off at the top of the handle and was stopped when the remaining single grain boundary had reached the bottom of the handle. Afterwards, the grain boundary freely expanded into the deformed blade of the shovel exerted by the annealing treatment applied to the entire specimen. These experiments manifested that grain boundaries with <110> and <100> rotation axes grow isotropically, i.e. the final shape of the growing grain is a semicircle. For a

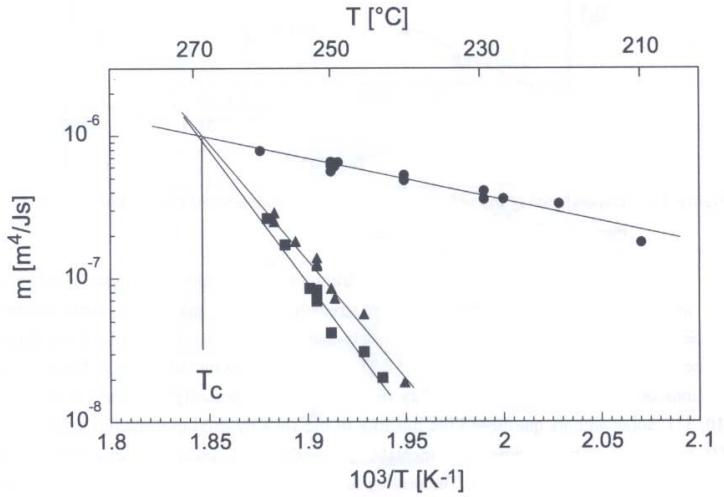

Figure 3.3: Temperature dependence of mobility of 90° {112} symmetrical and asymmetrical tilt grain boundaries in Bi-bicrystals

<111> rotation axis, a very anisotropic grain boundary mobility was discovered, the growing grain assumed the shape of a rectangle (Fig. 3.2a). The long straight facet of the grown grain is a slowly moving boundary. The facet is perpendicular to the <111> rotation axis, i.e. this "slow" boundary is a *twist* grain boundary (Fig. 3.2b). The *non-twist* grain boundary migrating in longitudinal direction moved orders of magnitude faster and "disappeared" from the specimen. These experiments showed for the first time that grain boundary mobility may strongly depend on crystallographic orientation of the boundary plane in a bicrystal.

In [23] the impact of boundary inclination on the mobility of planar tilt boundaries in Bi-bicrystals was studied comprehensively. The motion of symmetrical and asymmetrical tilt 90° <112> grain boundaries caused by the magnetic driving force was measured. In contrast to the symmetrical tilt boundary for the asymmetrical one the measured mobility was found to be distinctly different for the motion in opposite directions. For the chosen crystallography of bicrystals the boundary was less mobile, when the trigonal c-axis {111} of growing grain was perpendicular to the direction of motion (Fig 3.3). Symmetrical tilt boundary exhibited much higher mobility than asymmetrical tilt boundary and did not show dependence of boundary mo-

bility on the direction of the motion. This results showed that in materials of low-symmetry crystal structure the inclination of the tilt boundary plane has a pronounced effect on the boundary mobility and the mobility may even be asymmetric with respect to the direction of motion.

Recently, molecular dynamics simulations were performed to examine the effect of grain boundary inclination in FCC metals [24]. Motion of flat $\Sigma 5$ <110> asymmetrical boundaries in Ni was studied. To drive planar grain boundaries an elastic driving force was utilized. The results revealed that the mobility of differently inclined tilt boundaries exhibits local maxima and minima at all temperatures studied. The mobility varied by a factor of 2–4 with inclination, depending on temperature (4 at 727°C, 2 at 1127°C). The boundary mobility tends to decrease from a maximum for the symmetrical boundary to a minimum at the greatest inclination of 40°.

The motion of flat grain boundaries is more an exception than a rule. Grain structure evolution during grain growth is usually controlled by the motion of curved grain boundaries. Below we consider experiments where the motion of curved grain boundaries was studied. The general case of steady-state motion of a grain boundary under the action of its own energy was considered in [25]. Although that study was devoted to a U-shaped boundary (half-loop), the results can be applied to any other type of steady-state motion of grain boundaries, either quarter-loop or connected grain boundaries with a triple junction. The steady-state velocity of a half-loop boundary is given by

$$V = \frac{1}{a} \int_{-\frac{\pi}{2}}^{+\frac{\pi}{2}} A_b \, d\Theta, \tag{3.1}$$

where $A_b = m_b(\gamma + d^2\gamma_b/d\Theta^2)$ is the reduced mobility of the boundary element, Θ is the angle between the normal to the boundary element and the direction of the motion (Fig. 3.4a). As a matter of fact, the reduced mobility of a boundary element depends on its orientation. Therefore, the velocity of steady-state motion of the entire half-loop boundary has to be affected by its orientation in a crystal. Let us rotate the entire half-loop by the angle β with respect to a crystal direction parallel to the x-axis (Fig. 3.4b). Eq.(3.1) can be rewritten as

$$V = \frac{1}{a} \int_{\beta-\frac{\pi}{2}}^{\beta+\frac{\pi}{2}} A_b \, d\Theta, \tag{3.2}$$

i.e. the velocity of half-loop motion may depend on its orientation. In the case of a linear relationship between the velocity and the driving force (there

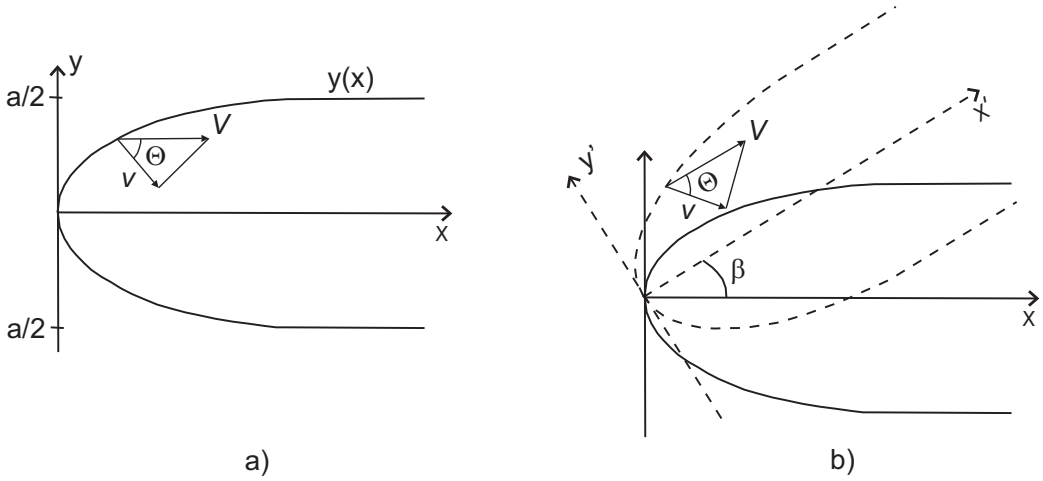

Figure 3.4: Grain boundary shape for the half-loop geometry. V – velocity of steady-state motion, v – normal velocity of boundary element

is no effect of grain boundary detachment from impurities – grain boundary breakaway), the dependence of the steady-state velocity on the half-loop orientation is determined by the difference between the mobilities of two straight (unmoving) boundary segments

$$\frac{dV}{d\beta} = \frac{A_b(\beta + \frac{\pi}{2}) - A_b(\beta - \frac{\pi}{2})}{a}. \tag{3.3}$$

If the crystal lattice has inversion symmetry, $A_b(\beta + \frac{\pi}{2}) = A_b(\beta - \frac{\pi}{2})$, then the velocity does not depend on half-loop orientation. This requirement is satisfied, for instance, for the motion of <100> tilt grain boundary in a half-loop geometry in cubic materials. In crystal materials without inversion symmetry, the velocity of the half-loop may depend on its orientation relative to given crystallographic direction.

This dependence was revealed for migration of 86° <11$\bar{2}$0> tilt boundaries in Zn-bicrystals [26]. The measured reduced mobility was found to depend non-monotonically on half-loop orientation (Fig. 3.5).

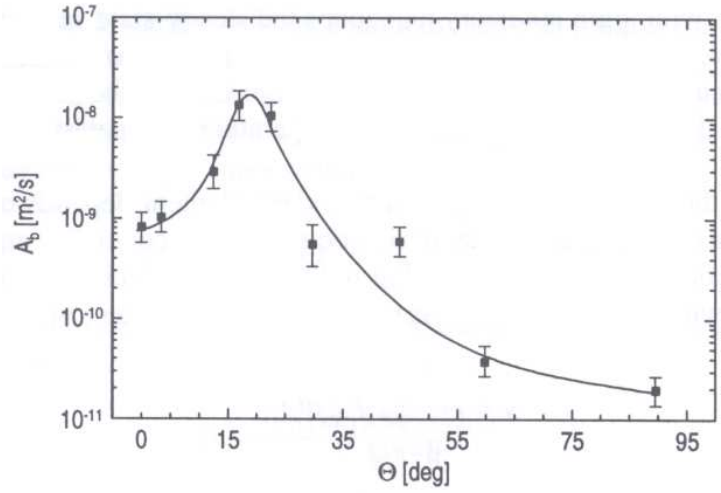

Figure 3.5: The reduce mobility of 86° <11$\bar{2}$0> tilt grain boundaries in Zn-bicrystals vs. the half-loop inclination

3.2 Experimental

Grain boundary motion under a constant driving force was measured in high pure Al-bicrystals (99.9995 wt. %, Al I , see Appendix A) with total impurity content of 5 wt. ppm. The driving force was provided by the free energy γ_b of the grain boundary (Eq. (1.17). For the initial flat grain boundary with the misorientation angle θ and the rotation axis <hkl> (Fig. 3.6) the ability of the curvature driven motion is not confined by configuration I shown in Fig. 3.6a. The same grain boundary can move in configuration II shown in Fig. 3.6b. The curved grain boundary in configuration I remains *tilt* and only the inclination of boundary planes changes (Fig. 3.6a) In contrast, the character of the curved boundary in the configuration II becomes *mixed* and changes along the boundary from symmetrical tilt to almost pure twist at the tip of the boundary (Fig. 3.6b). The motion of grain boundaries was studied in both configurations over the temperature range between 310°C and 610°C.

The migration of curved *mixed* tilt-twist boundaries was measured in the vicinity of $\Sigma 7$ CSL boundary (37° – 42°). The motion of symmetrical and asymmetrical curved *tilt* boundaries was measured as well. The

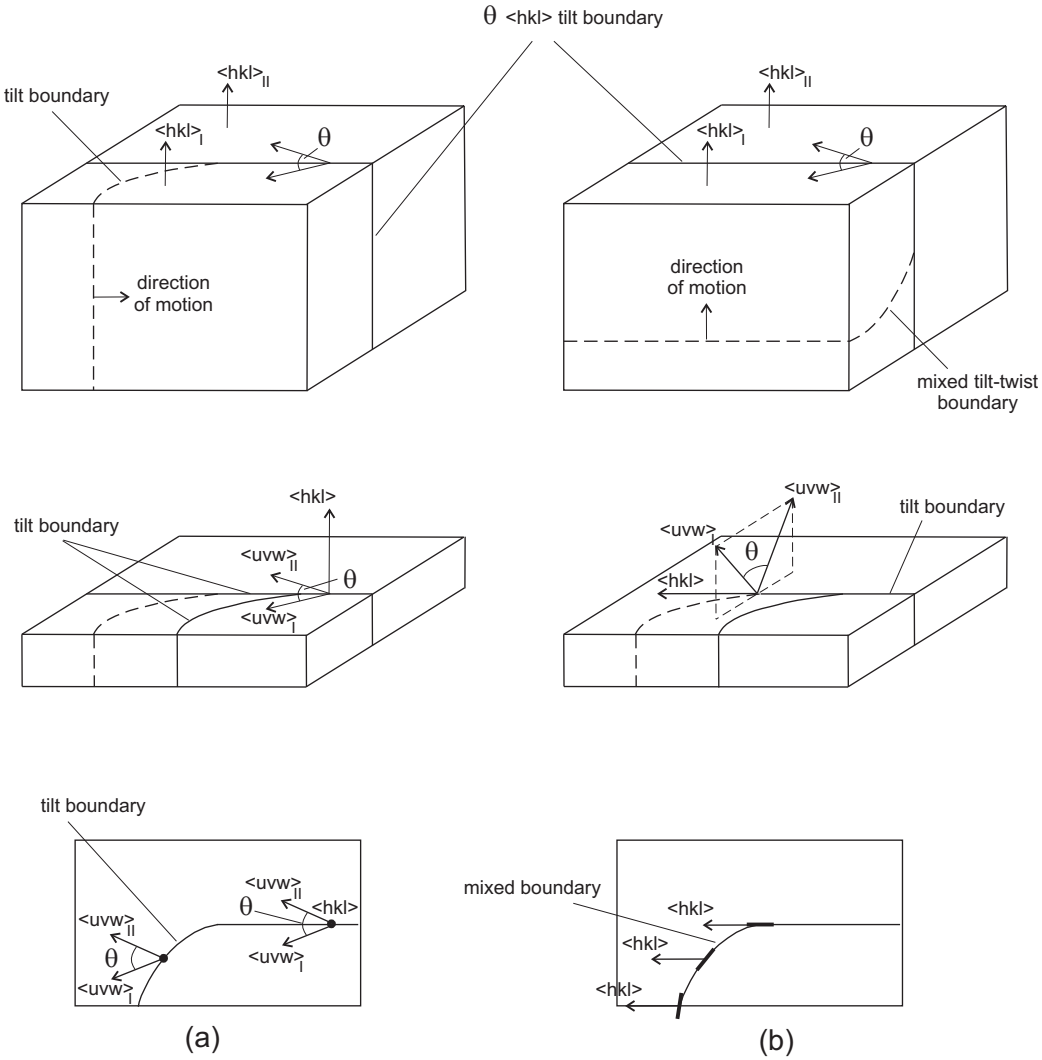

Figure 3.6: Bicrystal with initially straight symmetrical θ <hkl> grain boundary which moves under the capillary driving force as (a) pure tilt and (b) mixed tilt twist boundary

measured quantity is the steady-state boundary velocity v, from which the reduced mobility A_b and activation parameters (activation enthalpy H and pre-exponential factor A_0) were determined

$$A_b \equiv v \cdot a = m \cdot \gamma_b = A_0 \exp\left(-\frac{H}{kT}\right), \tag{3.4}$$

where a is the size of the shrinking grain, k is the Bolzmann constant.
The XICTD was utilized to record the grain boundary position.

3.3 Effect of boundary orientation on the motion of <111> tilt boundaries in Al

In this subsection the results on migration of tilt grain boundaries are reported. The purpose of this study was to examine the effect of orientation of the curved boundary on the steady-state motion of tilt grain boundaries. For the case of quarter-loop boundary motion Eq. (3.2) should be substituted by

$$V = \frac{1}{a}\int_{\beta}^{\beta+\frac{\pi}{2}} A_b \, d\Theta, \tag{3.5}$$

and Eq. (3.3) by

$$\frac{dV}{d\beta} = \frac{A_b(\beta+\frac{\pi}{2}) - A_b(\beta)}{a}. \tag{3.6}$$

One can see that the dependence of steady-state velocity on quarter-loop inclination is defined by the difference between the mobilities of the straight (unmoving) boundary section, $A_b(\beta+\frac{\pi}{2})$, and the boundary section aligned normally to the direction of the motion, $A_b(\beta)$.[1] If the crystal has inversion symmetry, then $A_b(\beta+\frac{\pi}{2}) = A_b(\beta)$, and the steady-state velocity does not depend on the quarter-loop orientation. In any other case the steady-state velocity may depend on quarter-loop orientation relative to a given crystallographic direction. In other words, the steady-state velocity of a curved grain boundary with rotation axis other than <100> is expected to depend

[1] For the sake of convenience we restrict here our discussion by the simplified situation where the grain boundary comes up with the angle of 90° to the specimen edge. Below we demonstrate that this approach is correct only for a particular case of grain boundary migration.

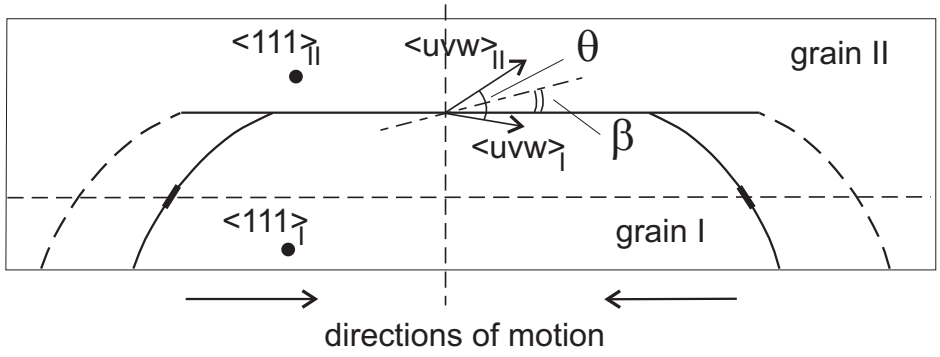

Figure 3.7: Motion of curved tilt boundary with different set of boundary planes. The straight section is symmetrical tilt boundary which can be inclined from its symmetrical position by an angle β

on its inclination in a crystal. To verify this concept, the motion of grain boundaries with high-symmetry rotation axis was experimentally measured.

We stress that in the used technique boundary inclination changes along the curved boundary and the measured velocity is averaged over all differently inclined boundary planes comprising the curved boundary.[2] As mentioned above, it is impossible to directly study the effect of grain boundary inclination on its mobility utilizing curvature as a driving force. In such experiments the orientation of the whole moving curved boundary can be changed by inclining the initial flat grain boundary from its symmetrical position (Fig. 3.7). The motion of different sets of boundary planes for the same θ <111> grain boundary can be measured and compared.

It is seen that the curved boundaries moving in opposite directions comprise the different sets of boundary planes even for an initially symmetrical <111> grain boundary. The greater the quarter-loop rotation angle β, the greater the difference between the orientations of the correspondent curved sections. If the boundary mobility depends on boundary inclination, this may affect the velocity of the steady-state motion of the entire curved boundary.

The mobility of <111> tilt grain boundaries moving in opposite directions

[2]The determined averaged mobility differs in principle from so-called "average" grain boundary mobility obtained in polycrystalline experiments, since in a polycrystal the average is taken over all boundaries with different boundary planes and misorientation angles

Table 3.1: Activation parameters for motion of quarter-loop shaped boundary in opposite directions

		forwards		backwards	
θ [°]	β [°]	H [eV]	A_0 [m^2/s]	H [eV]	A_0 [m^2/s]
36.8	0	1.79±0.14	$1.67{\cdot}10^3$ $^{+1.29{\cdot}10^4}_{-1.48{\cdot}10^3}$	1.79±0.08	$1.63{\cdot}10^3$ $^{+4.03{\cdot}10^4}_{-1.16{\cdot}10^3}$
34.3	7.1	1.95±0.12	$2.00{\cdot}10^4$ $^{+9.87{\cdot}10^4}_{-1.66{\cdot}10^4}$	1.91±0.07	$1.41{\cdot}10^4$ $^{+2.64{\cdot}10^4}_{-9.27{\cdot}10^3}$
36.3	5.5	1.88±0.25	$4.57{\cdot}10^3$ $^{+1.60{\cdot}10^5}_{-4.44{\cdot}10^3}$	2.05±0.09	$7.79{\cdot}10^4$ $^{+2.14{\cdot}10^5}_{-5.71{\cdot}10^4}$

was measured. It is shown in Fig. 3.8. As seen in this figure, practically no difference in mobility was found neither in the case of initially symmetrical nor in the case of initially asymmetrical boundary with the inclination angle β=5.5° and β=7.1°.

The independence of the quarter-loop motion of its orientation was also observed by Molodov [27] for the motion of 46.5° <111> tilt boundary in Al. In that study, orientation of the quarter-loop was changed by inclinating the straight boundary from its symmetrical position. The boundary velocity measured at a given temperature was found to be independent of the inclination angle β.

The activation parameters (activation enthalpy H and pre-exponential factor A_0) for the studied grain boundaries are shown in Tabl. 3.1. Evidently, the orientation of curved boundary does not affect its steady-state motion in the quarter-loop technique. As a result, we confirmed the independence of the reduced mobility for the <111> tilt boundary in Al-bicrystals (the *uniform mobility* of grain boundary) of its orientation.

3.4 Motion of mixed tilt-twist curved grain boundaries

When the boundary moves in configuration II (Fig. 3.6b), its moving curved part is not a tilt boundary anymore, but it has a *mixed tilt-twist* character. Note that the driving force is determined by the energy γ_b of the *flat* boundary and thus it is the same for both the *mixed* or for the *tilt* boundary motion.

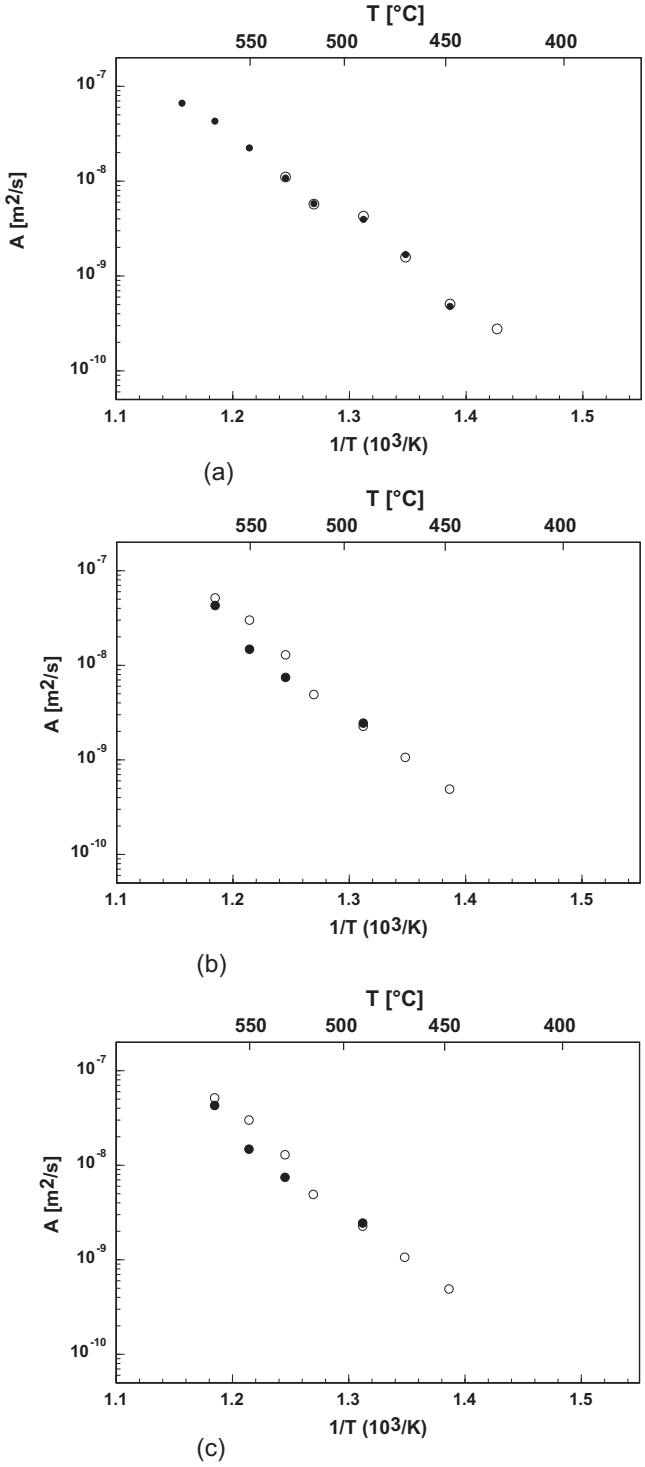

Figure 3.8: Reduced grain boundary mobility measured in opposite directions for (a) symmetrical 36.8° <111>, for (b) asymmetrical 36.3° (β=5.5°) and for (c) 34.3° (β=7.1°) <111> tilt grain boundaries. Solid dots – forwards, open dots – backwards

The motion of tilt grain boundaries in configuration I was comprehensively studied by Molodov et al. and by Aristov et al. [15, 18]. The motion of individual grain boundaries in the configuration shown in Fig. 3.6b has not been measured so far neither in experiment nor by computer simulation.

The strong inclination anisotropy of grain boundary properties (grain boundary energy and grain boundary mobility) leads to grain boundary faceting [22].[3] Let us consider the steady-state motion of a quarter-loop boundary which comprises both tilt and twist components (Fig. 3.6b). In such configuration the character of curved boundary changes along the boundary from tilt and becomes mixed with increasing the fraction of twist and decreasing the fraction of tilt components. We can expect that steady-state motion of curved grain boundary which comprises both tilt and twist components is essentially different from the tilt boundary motion with respect to mobility or the tendency of faceting. Grain boundary mobility of mixed boundaries and their shape were measured and the results are presented below.

3.4.1 Shape of moving grain boundary

The shape of the moving grain boundary is a source of very useful data with regard to the orientation dependence of boundary energy and boundary mobility or interaction between the moving grain boundary and impurities. In what follows we analyze the shape of the moving boundaries measured in the experiments. The shape of a steadily moving grain boundary was considered by Fradkov et al. [25] for a half-loop and by Verhasselt et al. [28] for a quarter-loop. Let us remind basic the idea and the assumptions made to obtain the analytical shape of the boundary [25, 28].

- The reference coordinate system is attached to the steadily moving boundary. That means that all boundary elements are at rest with regard to the coordinate system (Fig. 3.9).
- The grain boundary moves together with the line where the curved boundary intersects the lateral surface of the specimen. At this line a triple junction is formed by three surfaces (the grain boundary and two

[3] In recent studies on faceting it has been shown that anisotropy of grain boundary mobility has a little effect on parameters of grain growth, while anisotropy of grain boundary energy leads to substantial deviations from the parabolic low

external surfaces) and its geometrical comfiguration is established by equilibrium of the surface energies γ_b, γ_1^s and γ_2^s. Since the system is homogenious through the bicrystal, this leads to a quasi-two-dimentional problem.

- The energy γ_b and the grain boundary mobility m_b are independent of the orientation of the grain boundary plane with regard to the crystallographic directions in a crystal.

The velocity of normal displacement of the boundary element is given by

$$v = m_b \gamma_b k, \tag{3.7}$$

where k is the Laplace curvature of the considered boundary element. For a steadily moving grain boundary, its shape is invariant and every element of boundary moves parallel to the x-axis with velocity V. The normal velocity v and grain boundary displacement rate V are related by the angle φ (Fig. 3.9)

$$v = V \cos\vartheta = V \frac{y'}{\sqrt{1 + (y')^2}}, \tag{3.8}$$

where $y(x)$ is the function describing the shape of the moving grain boundary. Combining Eq. (3.7) and Eq. (3.8) and using the equation for the radius of the curvature,

$$k = \frac{y''}{\sqrt{1 + (y')^2}}, \tag{3.9}$$

we derive the equation of the boundary shape

$$y'' = -\frac{V}{\gamma_b m_b}[1 + (y')^2]. \tag{3.10}$$

Integration of Eq. (3.10) then yields

$$y = y_0 + \frac{m_b \gamma_b}{V} \arccos\ \exp(-\frac{(x - x_0)V}{m_b \gamma_b}), \tag{3.11}$$

where x_0 and y_0 are the integration constants. With the boundary conditions

$$\begin{aligned} &y(0) = 0, \\ &y(\infty) = a/2, \\ &y'(0) = \tan\theta, \end{aligned} \tag{3.12}$$

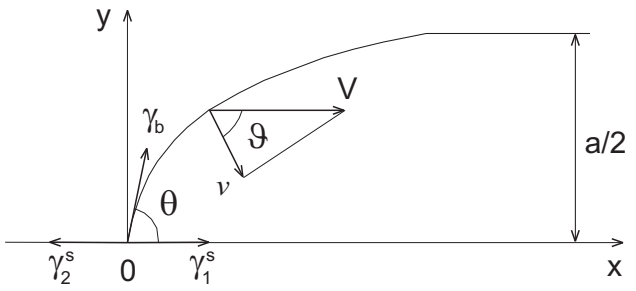

Figure 3.9: Shape of a moving grain boundary

we obtain the solution of Eq. (3.10):

$$y(x) = \frac{a}{2\theta}\left(\theta - \frac{\pi}{2}\right) + \frac{a}{2\theta}\arccos\exp\left(-\frac{2\theta}{a}x + \ln\sin\theta\right), \tag{3.13}$$

where $a/2$ is the grain width. According to Eq. (3.10) the grain boundary displacement rate is given by

$$V = 2\frac{\theta m_b \gamma_b}{a}. \tag{3.14}$$

Eq. (3.13) and (3.14) describe the shape and the velocity of a moving quarter-loop grain boundary under its own curvature.

It is worth emphasizing that the grain boundary mobility m_b is an *intrinsic* mobility. Eq. (3.13) describes the shape of a freely moving quarter-loop. In other words the interaction between impurity atoms or other obstacles and the moving boundary is neglected. For the quarter-loop affected by impurity drag this has to be taken into account.[4]

It follows from Eq. (3.7) that the normal velocity of grain boundary changes locally. It reaches maximum at the front line and tends to zero where the loop section becomes parallel to x-axis. In accordance with the theory of Lücke and Detert [29] there is a limiting velocity v^* where impurities can still move together with the boundary. Sections of the quarter-loop, whose velocity v exceeds v^*, consist of boundary segments detached (free) from impurities as well as loaded segments ($v < v^*$) moving together with impurities. These two parts differ in their mobilities, i.e. the mobility of

[4] In [28] it has been shown that even in very pure metals the impurity interaction has to be taken into account to avoid misinterpretention of experimental data

the "loaded" part m_b^l is lower then the mobility of the "free" part m_b^f, i.e. $0 < \frac{m_b^l}{m_b^f} < 1$. Since the boundary cannot be discontinuous or contain kinks, the following conditions must be satisfied at the point x^* on the boundary, which moves exactly with the velocity v^*:

$$\begin{aligned} y_b^l(x^*) &= y_b^f(x^*), \\ {y'}_b^l(x^*) &= {y'}_b^f(x^*). \end{aligned} \tag{3.15}$$

For the sake of convenience m_b^l and m_b^f are substituted by

$$\begin{aligned} b_l &= \frac{m_b^l \gamma_b}{V}, \\ b_f &= \frac{m_b^f \gamma_b}{V}. \end{aligned} \tag{3.16}$$

In conjuction with the boundary conditions (Eq. (3.12)) Eq. (3.10) is solved

$$y = \begin{cases} -(b_f - b_l)\arccos\left(\frac{\sin\theta}{\exp\left(x^*/b_f\right)}\right) + \frac{a}{2} - b_l\frac{\pi}{2} + \\ \quad + b_f \arccos\left(\exp\left(\frac{b_f \ln(\sin\theta) - x}{b_f}\right)\right), & 0 \le x \le x^*, \\ \frac{a}{2} - b_l\frac{\pi}{2} + b_l \arccos\left(\exp\left(\frac{b_l \ln(\sin\theta) - x^*(b_l/b_f - a) - x}{b_l}\right)\right), & x \ge x^*, \end{cases}$$

where b_l is a function of b_f and x^*:

$$b_l = \frac{b_f\left(\arccos\left(\frac{\sin\theta}{\exp(x^*/b_f)}\right) + \theta - \frac{\pi}{2}\right) - \frac{a}{2}}{\arccos\left(\frac{sin\theta}{\exp\left(x^*/b_f\right)}\right) - \frac{\pi}{2}}. \tag{3.17}$$

The calculated shape was fitted to the experimental data obtained for the 40.6° <111> *mixed* grain boundary. The grain boundary mobility was extracted from in-situ experiments of grain boundary motion. After measuring the grain boundary mobility the specimen was rapidly cooled to room temperature and the boundary shape was recorded with an optical microscope (Fig. 3.10). The boundary mobility was measured at the temperature of 602°C and was found to be $A_b^l = 2.7 \cdot 10^{-7}$ m^2/s. To analyze the boundary shape we also need the grain boundary mobility A_b^f which can be associated with the mobility of the "free" moving boundary. In this content "free" means that there is no difference in concentraion of impurity atoms at the boundary and in the bulk. The migration of mixed boundaries has not been

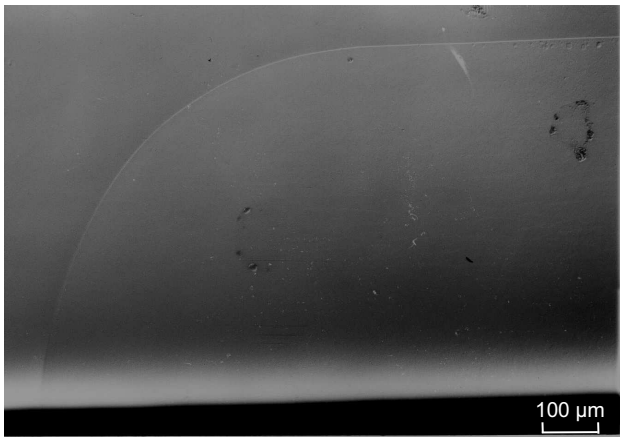

Figure 3.10: Shape of a moving grain boundary recorded with a optical microscope after fast cooling

studied so far in Al with different impurity content, therefore the exact value of the ratio b_l/b_f is unknown. However, this value can be obtained from the analysis of the boundary shape. Both b_l/b_f and x^* were used as fitting parameters (Fig. 3.11a). The calculated curve is plotted for $b_l/b_f = 0.2$ and $x^* = 336$ μm. Consistency between measured and calculated grain boundary shapes allows concluding that different elements of the investigated boundary have the same mobilty *irrespective* of their composition of tilt and twist components. That means that an increase of the twist component along the curved mixed boundary does not affect its steady-state motion.

It is interesting to compare the motion of tilt and mixed tilt-twist grain boundaries with regard to their shape. The motion of curved tilt grain boundaries was studied by Molodov et al. [15] in Al-bicrystals of the same total impurity content (99.9995 wt. %) as in our work. The reduced mobility of 40.6° <111> *mixed* boundary measured in the present work and that of 40.5° <111> *tilt* boundary measured in [15] at the same temperarure of 602°C are almost equal ($A^l_{mixed} = 2.7 \cdot 10^{-7}$ m^2/s and $A^l_{tilt} = 1.8 \cdot 10^{-7}$ m^2/s). Thus, the values of b_l^{tilt} and b_l^{mixed} determined by Eq. (3.16) are also the same. As mentioned above, to analyze the grain boundary motion we also need the mobility A^f_b of "free" grain boundary (without segregated impurities). Since there are no experimental data on mobility of mixed grain boundaries, A^f_{mixed}, we use data obtained in [15] for the motion of <111> tilt bound-

aries in bicrystals of ultra-pure aluminum with total impurity concentration of 0.4 wt. ppm. Correspondent mobility A_b^f of 40.5° <111> *tilt* boundary is $4.9 \cdot 10^{-5}$ m^2/s. In this case the ratio $b_l^{mixed}/b_f^{tilt} = 5.5 \cdot 10^{-3}$, and to fit the shape we vary only parameter x^*. Best fit was found for x^*=461 μm. The ratio b_l/b_f varies by the factor of two orders from that obtained by "fitting" (Fig. 3.11a). The calculated in accordance with Eq. (3.17) and experimental shapes are plotted in Fig. 3.11b.

It is obvious that there is some difference between the experimental and theoretical shapes of the moving grain boundary. Let us consider possible reasons for this discrepancy. The reduced mobilities A_{mixed}^l of 40.6° <111> *mixed* boundary measured in the present work and A_{tilt}^l of 40.5° <111> *tilt* boundary measured in [15] at 602°C in the material of the same purity are almost *equal*. Therefore, this discrepancy may be only due to the difference in mobilities A_{tilt}^f and A_{mixed}^f of correspondent "free" sections of *tilt* and *mixed* boundaries. In other words the ratio b_l/b_f for the *mixed* boundary is different from that for the *tilt* boundary.

Such analysis shows that the change of boundary character may affect grain boundary mobility, but this effect can only be noticeable in *ultra-pure* materials. In the studied material no influence of boundary character on grain boundary mobility and grain boundary shape was found. We stress that critical point x^* should be a function of impurity adsorption at the grain boundary and therefore, it should be related to the total impurity concentration. A direct comparison of x^* for each content of impurities is not possible because of the variation in the width $a/2$ of the shrinking grain and in turn the variation in the driving force. Assuming that the grain boundary energy γ_b does not depend on impurity content, we can determine the ratio $x^*/(a/2)$. The measured value of $x^*/(a/2)$ was found to be equal to 0.56. For the motion of correspondent tilt boundary [28] in the same material this parameter was equal to 0.58. Thus, while the grain boundary mobility in ultra-pure materials certainly reflects the boundary character, it is not affected by the boundary character in high – although not ultra-pure materials.

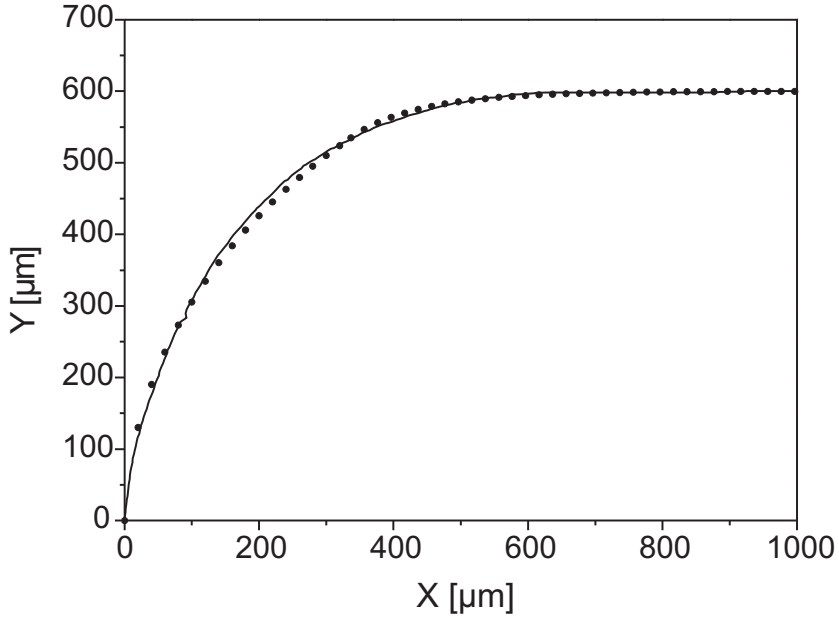

(a)

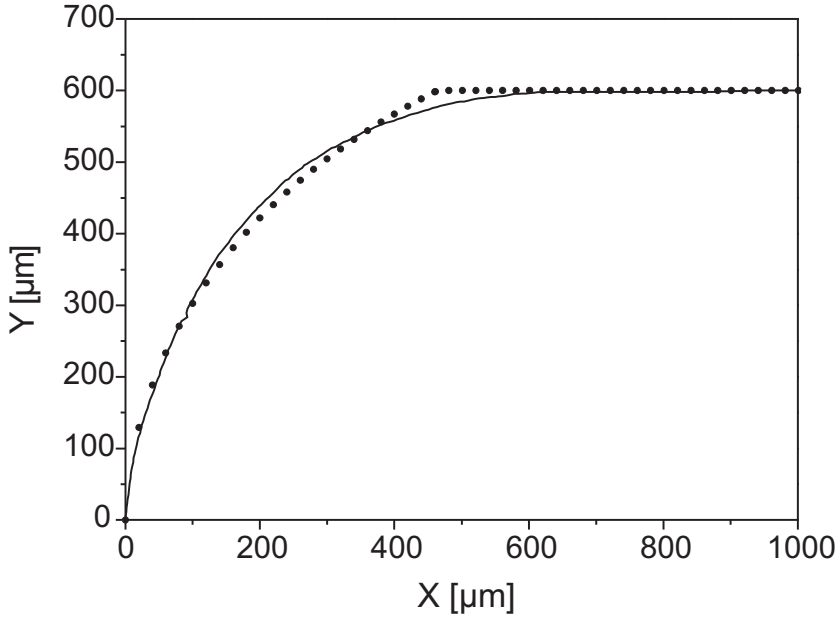

(b)

Figure 3.11: (a) Fitting curve ($\theta = 88°$, $b_l/b_f = 0.2$, $x^* = 336\ \mu m$). Both b_l/b_f and x^* are fitted. (b) Fitting curve for $b_l^{mixed}/b_f^{tilt} = 5.5 \cdot 10^{-3}$ ($\theta = 88°$, $x^* = 461\ \mu m$), only x^* is fitted

3.4.2 Misorientation dependence of grain boundary mobility

The migration of <111> mixed boundaries was measured in the vicinity of $\Sigma 7$ CSL boundary in the angular interval of misorientations between 37° and 42°. The experiments revealed that misorientation dependence of activation parameters (activation enthalphy and pre-exponetial factor) are non-monotonous and the minimum corresponds to the $\Sigma 7$ misorientation of the CSL-lattice (Fig. 3.12, Tabl. 3.2). Such misorientation dependence is very similar to the respective misorientation dependence obtained in the past for <111> tilt boundaries in Al (Fig. 3.13). However, the magnitude of the oscillations for the mixed boundaries is less then that for tilt boundaries.

One is tempted to attribute the observed difference to variance in the grain boundary structure, i.e. in grain boundary character, which determines the *intrinsic* boundary mobility. However, in [15] the grain boundary migration was studied in ultra-pure Al with a total impurity content of 0.4 wt. ppm. Misorientation dependence of grain boundary mobility has not not studied so far in Al of the same purity. Therefore, it is impossible to distinguish between the influence of impurity segregation and boundary structure on the mobility.

To solve this problem the specimens should be produced from the same "thick" bicrystal to study the migration of tilt and mixed boundaries, identical in terms of misorientation and chemistry.

3.4.3 Compensation effect

In this subsection, we briefly review fundamentals of the compensation effect and the activated state. The comprehensive review dedicated to the compensation effect can be found in [8] or [9].

It is a textbook knowledge that the temperature dependence of grain boundary mobility follows the Arrhenius relation:

$$m_b = m_0 \exp\left(-H_m/kT\right). \tag{3.18}$$

For evaluation of experimental data the activation enthalpy H_m is determined from the slop H_m/k of the Arrhenius plot ln m_b vs. $1/T$. Much less attention is devoted to the pre-exponential factor m_0. However, there are numerous experiemens which demostrate that the pre-exponential factor is strongly

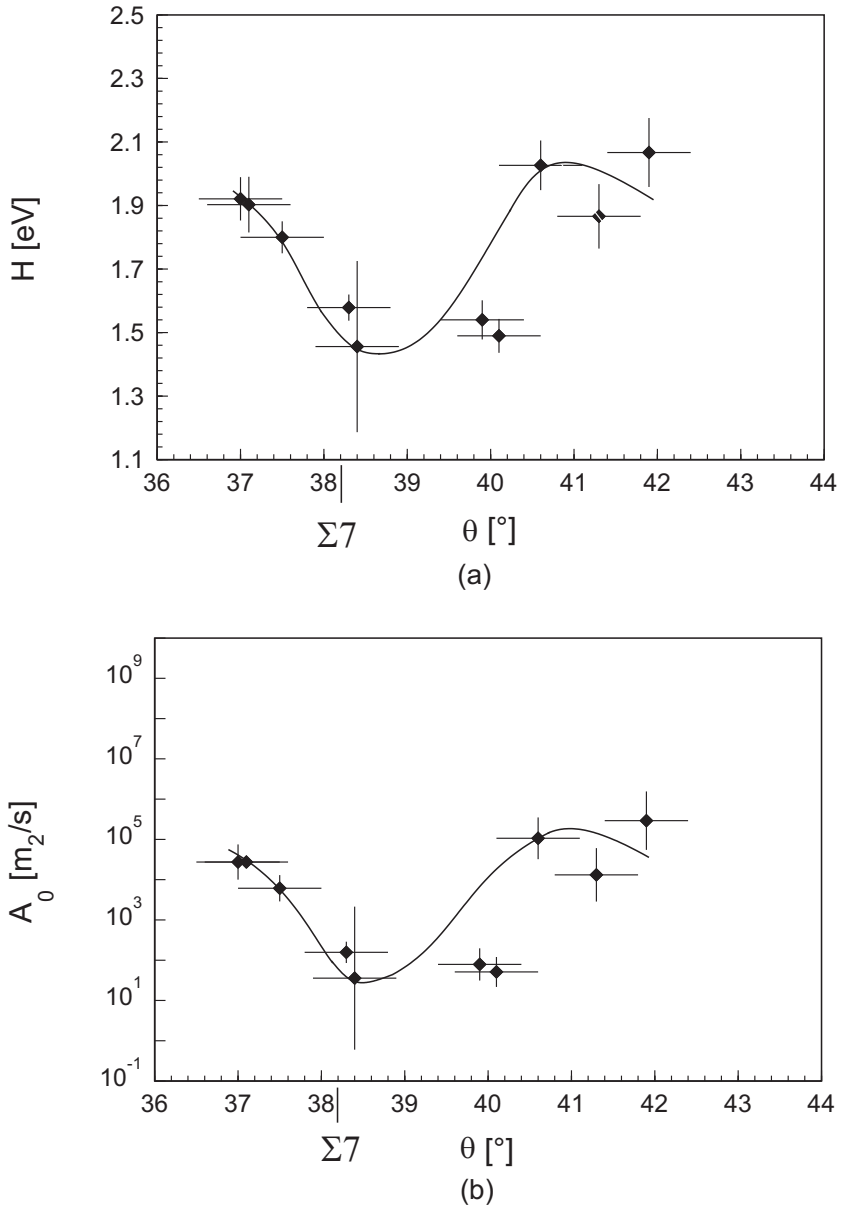

Figure 3.12: Measured (a) migration activation enthalpy H and (b) pre-exponetial factor A_0 vs. misorientation angle for <111> mixed boundaries in Al

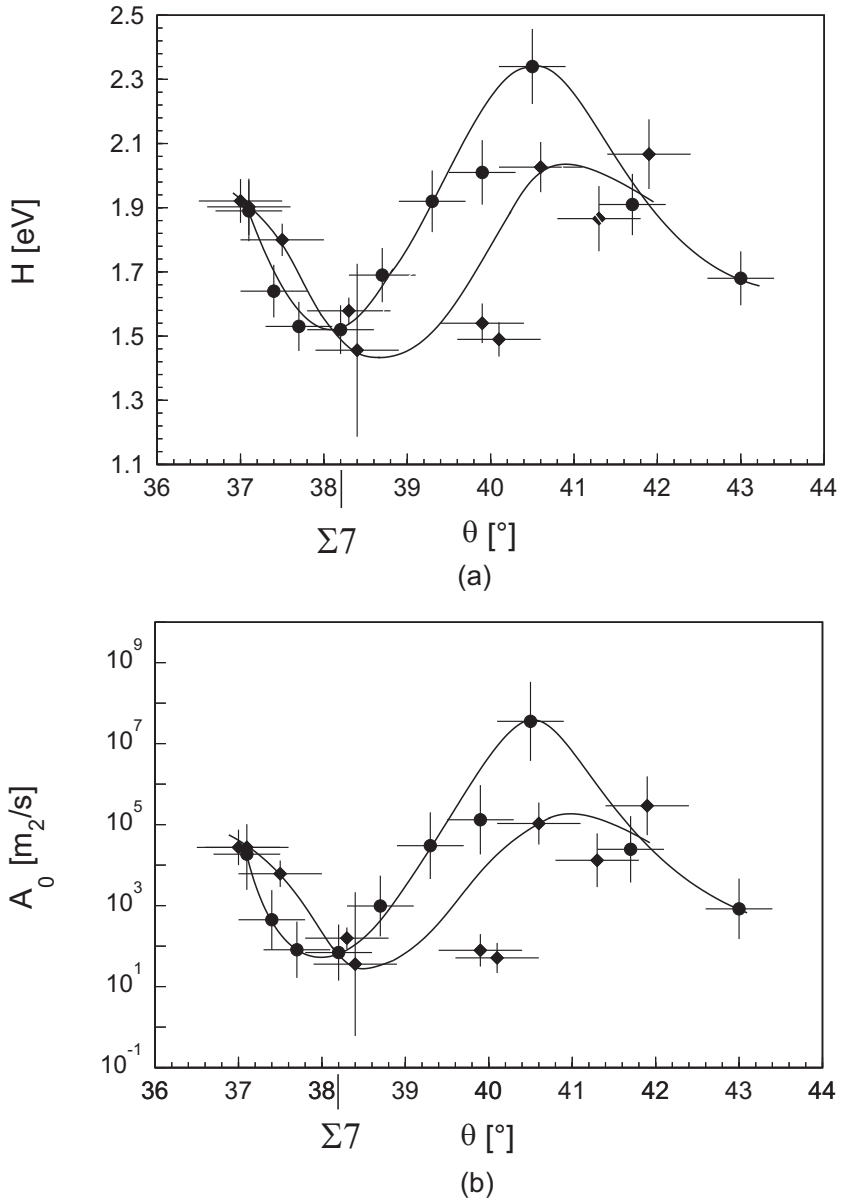

Figure 3.13: Misorientation dependencies of (a) migration activation enthalpy H and (b) pre-exponetial factor A_0 for <111> mixed boundaries (rhombus dots) measured in current study and for <111> tilt boundaries (circle dots) [15] in Al

Table 3.2: Activation parameters for motion of <111> mixed boundaries in Al

θ [°]	H [eV]	A_0 [m^2/s]
37.0 ± 0.4	1.92 ± 0.35	$2.74 \cdot 10^4$ $^{+4.71 \cdot 10^4}_{-1.74 \cdot 10^4}$
37.1 ± 0.4	1.90 ± 0.09	$2.74 \cdot 10^4$ $^{+3.42 \cdot 10^4}_{-5.47 \cdot 10^3}$
37.5 ± 0.4	1.80 ± 0.05	$6.12 \cdot 10^3$ $^{+1.24 \cdot 10^4}_{-3.23 \cdot 10^3}$
38.3 ± 0.4	1.58 ± 0.04	$1.57 \cdot 10^2$ $^{+1.32 \cdot 10^2}_{-7.16 \cdot 10^1}$
38.4 ± 0.4	1.46 ± 0.27	$3.59 \cdot 10^1$ $^{+2.11 \cdot 10^3}_{-3.53 \cdot 10^1}$
39.9 ± 0.4	1.54 ± 0.06	$7.86 \cdot 10^1$ $^{+1.19 \cdot 10^2}_{-4.73 \cdot 10^1}$
40.1 ± 0.4	1.49 ± 0.05	$5.11 \cdot 10^1$ $^{+6.90 \cdot 10^1}_{-2.93 \cdot 10^1}$
40.6 ± 0.4	2.03 ± 0.08	$1.06 \cdot 10^5$ $^{+2.45 \cdot 10^5}_{-7.43 \cdot 10^4}$
41.3 ± 0.4	1.87 ± 0.10	$1.32 \cdot 10^4$ $^{+4.75 \cdot 10^4}_{-1.03 \cdot 10^4}$
41.9 ± 0.4	2.07 ± 0.11	$2.92 \cdot 10^5$ $^{+1.26 \cdot 10^6}_{-2.37 \cdot 10^5}$

related to the activation enthalphy according to the relation

$$H = \alpha \ln m_0 + \beta. \tag{3.19}$$

Here α and β are constant. Eq. (3.19) is refered to as the compensation effect. This equation implies the existence of a specific temperature $T_c = \alpha/k$, the compensation temperature, at which the mobilities m_b of the grain boundaries with different misorientation angles are the same.

Let λ denote some intensive structural property, like surface tension, excess free volume etc. Eq. (3.19) can be substituted by

$$\ln m = \ln m_0 - H_m/kT = \frac{S_m}{k} - \frac{H_m}{kT}, \tag{3.20}$$

where $S_m = k \ln m_0$ is the activation entropy of grain boundary mobility.

If λ changes slightly from the reference ground state λ_0, then H_m and S_m change accordingly:

$$\ln m_0(\lambda) = S_m(\lambda)/k = \frac{1}{k}\left(S_m(\lambda_0) + dS_m/d\lambda|_{\lambda=\lambda_0} \cdot (\lambda - \lambda_0) + \ldots\right), \tag{3.21}$$

$$H_m(\lambda) = H_m(\lambda_0) + dH_m/d\lambda|_{\lambda=\lambda_0+\ldots} \tag{3.22}$$

Since $G = H - TS$ is at minimum, S_m and H_m change only slightly, and a linear approximation is sufficient. Solving Eq. (3.22) for $\lambda - \lambda_0$ yields:

$$\ln m_0(\lambda) = \frac{S_m(\lambda_0) - H_m(\lambda_0)/T_c}{k} + \frac{H(\lambda)}{kT_c}, \tag{3.23}$$

where

$$T_c = \frac{dH_m/d\lambda|_{\lambda=\lambda_0}}{dS_m/d\lambda|_{\lambda=\lambda_0}} = \frac{dH}{dS}|_{\lambda=\lambda_0} \tag{3.24}$$

is the compensation temperature, i.e. the equilibrium temperature between ground state and activated state. This result implies that the activated state is closely related to the ground state. It corresponds to an atom configuration with the smallest increase of potential energy with respect to the ground state. It seems obvious that the ground state or the equilibrium state in the vicinity of the compensation temperature most easily satisfies this requirement. This conclusion is supported by the observation that the compensation temperature is often close to the equilibrium temperature of a nearby phase transformation.

According to thermodynamics of the activated state considered above, the compensation effect opens up the possibilities to look at the mechanisms of grain boundary migration. Below we discuss the misorientation dependence of grain boundary mobility in terms of the compensation effect.

The compensation dependence for migration of <111> mixed boundaries is shown in Fig. 3.14a. Fig. 3.14b exhibits compensation dependence for both mixed and tilt <111> boundaries in Al. As can be easily seen, there is a good consistence between the activation parameters for both types of curved boundaries: mixed and tilt. This result indicates that the activation enthalpy H_m and the activation entropy S_m of migration change similarly with the angle of misorientation for both types of boundaries: tilt and mixed (tilt-twist).

This suggests the conclusion that the mechanism of grain boundary migration does not change if the boundary changes its character from pure tilt to mixed tilt-twist. The determined compensation temperature T_c=500±70°C is very close to the compensation temperature measured for migration of <111> tilt boundaries T_c=485±50°C.

3.5 Summary

Grain boundary migration of curved <111> tilt and mixed tilt-twist grain boundaries was studied over the wide temperature range. The shape of a moving mixed tilt-twist boundary was analyzed. The following results were obtained.

From the temperature dependence of grain boundary mobility the activation enthalpy H_m and pre-exponential factor A_0 were determined. It was revealed that the change of the set of boundary planes in the curved moving part of the boundary does not affect its steady-state motion. This study was achieved by using specimens with different inclination of the initial straight boundary from its symmetrical position. Subsequently, the motion of such symmetrical and asymmetrical *tilt* boundaries was measured in the same specimen but in the opposite directions. The independence of reduced mobility for <111> tilt boundary of the orientation of the entire curved boundary in Al-bicrystals was confirmed.

The migraion of curved <111> mixed tilt-twist grain boundaries was also studied. The shape of moving mixed boundary was measured and compared with the calculated one. The results manifest that there is no effect of the

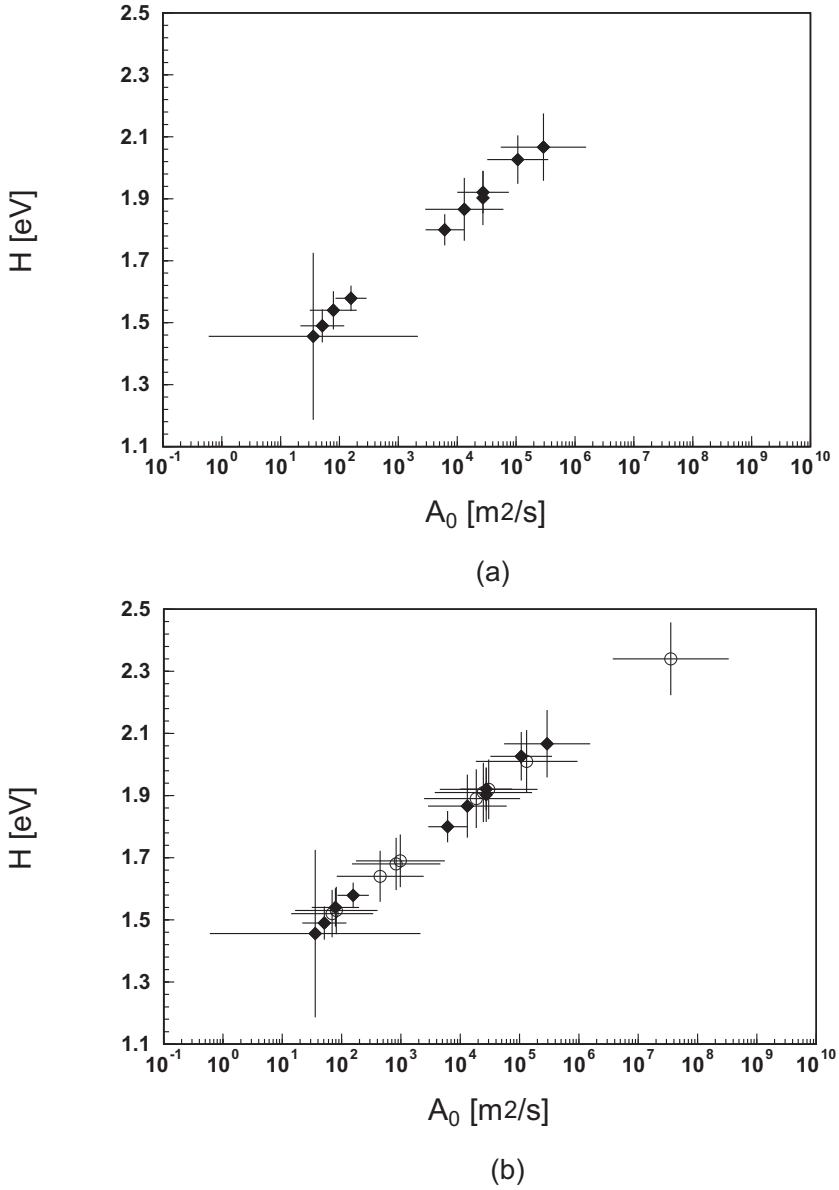

Figure 3.14: (a) dependence of migration activation enthalpy H_m on the (reduced) pre-exponential mobility factor A_0 for <111> mixed grain boundaries in Al, (b) same as (a), but also for <111> tilt grain boundaries (open dots) [15]

boundary character on steady-state grain boundary motion in high, although not ultra-pure aluminum. In addition, it was predicted that the effect of boundary character can be important in ultra-pure materials.

Both the misorientation and compensation dependencies of grain boundary mobility reinforce the conclusion that a change of boundary character of the curved moving boundary does not influence its steady-state motion.

Chapter 4

Impact of external crystal surface on the motion of solitary grain boundaries in bicrystals

The migration of a *truly* free grain boundary, i.e. the motion of a grain boundary without any interaction with other imperfections in the crystal, is only possible in a hypothetical case of an ideal spherical grain shrinking in a defects-free crystal body. In a polycrystal a moving grain boundary always interacts with imperfections like particles, dislocations, external surfaces etc. Their interaction with the moving boundary has a very different nature and thus must be treated separately. The basic factors which can drag grain boundary motion have been briefly reviewed in Chapter 1. In this chapter we discuss the interaction between the moving grain boundary and the external surface of a specimen.

Recent experimental [30, 31] and theoretical studies [32, 33, 34] have demonstrated that a grain boundary triple junction can have a *finite* mobility that results in a marked decrease of the grain boundary migration rate. In the majority of bicrystal experiments grain boundary migration was measured in quarter-loop geometry (Fig. 4.1). The boundary in this geometry intersects the external surface of the specimen forming a "surface" triple junction (free surface – grain boundary – free surface). The role of the surface triple junction (STJ) is usually reduced to maintaining the thermodynamic equilibrium in terms of the contact angle θ (Fig. 4.1) during the grain boundary migration. If however, the STJ possesses its own *finite* mobility, the boundary migration will be influenced by the junction velocity.

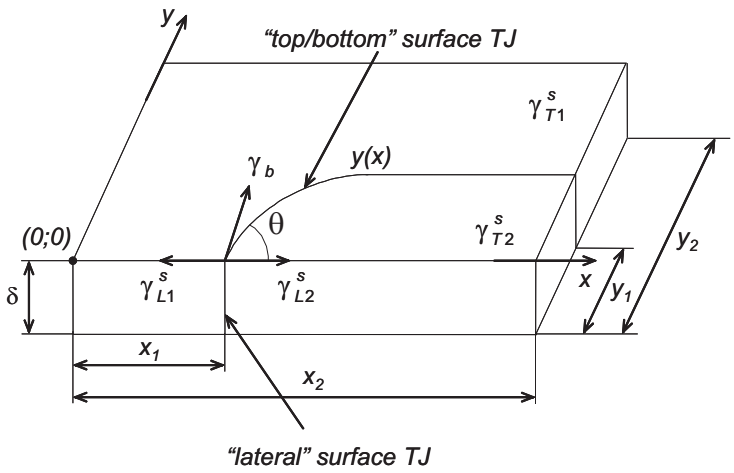

Figure 4.1: Bicrystal geometry and the surface tensions

So far, the steady-state motion of individual grain boundaries was studied in bicrystals where the (specific) surface free energy of the adjoining grains was only slightly different. Therefore, the anisotropy of (specific) free surface energy was always neglected. In reality, however, there are configurations with the the strong anisotropy of surface energy of the adjoining grains.

In what follows both the effect of surface triple junction and the effect of external surface anisotropy on grain boundary motion in bicrystals are addressed. It is mandatory to note that interaction of the moving grain boundary with a free surface leads to another surface defect – thermal groove. We also discuss the interaction between the boundary and the thermal groove.

4.1 Interaction of moving grain boundary with external crystal surface

The curved grain boundary moves together with the triple junction line where it intersects the specimen surface. During its motion, the boundary forms "lateral" and "top/bottom" surface triple junctions on the lateral and top/bottom specimen surfaces, as in Fig. 4.1. For the sake of convenience we consider, one by one, the interaction of grain boundary with the lateral and with the top/bottom surface of the specimen.

4.1.1 Effect of "lateral" STJ on boundary migration

The line of the "lateral" surface junction is formed by grain boundary and two external surfaces, and, as it shown below, its geometrical configuration is established by the equilibrium of the three energies γ_b, γ^s_{L1}, γ^s_{L2}. The triple junction line runs straight through the specimen from the top to the bottom surface. Close to this line the grain boundary is considered to be planar. This leads to a quasi-two-dimensional configuration.

The free energy of the system G in a quasi-two-dimensional approximation can be presented as the sum of boundary (γ_b) and (specific) surface energies of external surfaces ($\gamma^s_{T_1}$, $\gamma^s_{T_2}$, $\gamma^s_{L_1}$, $\gamma^s_{L_2}$) (Fig. 4.1)

$$G = \int_{x_1}^{x_2} \left[2\Delta\gamma^s_T y + \delta\gamma_b\sqrt{1-y'}\right] dx + \Delta\gamma^s_L x_1\delta + C = \int_{x_1}^{x_2} U dx + W, \quad (4.1)$$

where $\Delta\gamma^s_T = \gamma^s_{T_2} - \gamma^s_{T_1}$, $\Delta\gamma^s_L = \gamma^s_{L_1} - \gamma^s_{L_2}$ are the differences between the (specific) free energies of top/bottom and lateral surfaces of the specimen, respectively, C is a constant equal to the sum of bulk energy and part of the surface energy which does not depend on the coordinate x, U and W are defined by this equation.

The curved boundary moves freely along the lateral surface of the specimen defined by $y = 0$. For the "boundary – free surface" equilibrium at the point $x = x_1$ it can be expressed by

$$\left|\frac{dU}{dy'} - \frac{\partial W}{\partial x}\right|_{y=0} = 0. \quad (4.2)$$

Eq. (4.1) and Eq. (4.2) render the equilibrium condition

$$\left|\frac{\gamma_b y'\delta}{\sqrt{1+(y')^2}} - \Delta\gamma^s_L\delta\right|_{y=0} = 0 \quad (4.3)$$

or, expressing y' as a function of the contact angle θ,

$$\gamma_b\cos\theta = \Delta\gamma^s_L. \quad (4.4)$$

It can be seen in Eq. (4.4), the contact angle θ is defined by the ratio of the boundary energy to the difference in (specific) energies of the external surfaces on the lateral side of the specimen.[1]

[1]Evidently, the angle θ does not need to be equal to $\pi/2$. According to Eq. (4.4) the angle $\theta \neq \pi/2$ can be due to $\Delta\gamma^s_L \neq 0$ irrespective of the presence of a thermal groove on the specimen surface, contrary to [35]

The shape of the moving grain boundary has been considered in Chapter 3. It has been shown that solution of Eq. (3.10) with boundary conditions Eq. (3.12) provides the shape of the moving grain boundary $y(x)$, and then the velocity of steady-state motion is given by

$$V_{gb} = \frac{\theta m_b \gamma_b}{a}. \tag{4.5}$$

On the other hand, the velocity of a "lateral" surface triple junction (Fig. 4.1) can be described with the surface triple junction mobility m^s_{tj} analogous to the mobility m_{tj} of the grain boundary triple junction [42]

$$V_{tj} = m^s_{tj} \left(\gamma_b \cos\theta - \gamma^s_{L2} + \gamma^s_{L1} \right). \tag{4.6}$$

Since the boundary velocity V_{gb} must be equal to the velocity of the surface triple junction V_{tj}, Eq. (4.5) and Eq. (4.6) yield an expression

$$\frac{\theta}{\cos\theta - (\Delta\gamma^s_L/\gamma_b)} = \frac{m^s_{tj} a}{m_b} = \Lambda. \tag{4.7}$$

Eq. (4.7) links the steady-state value of the angle θ with dimensionless criterion $\Lambda = m^s_{tj} a / m_b$, which reflects the drag influence of a surface triple junction on grain boundary migration. For the low mobility of the surface junction ($\Lambda \to 0$) grain boundary migration is governed by the *junction kinetics*. In contrast, for the infinite junction mobility ($\Lambda \to \infty$) the motion of the boundaries with the surface triple junction is controlled by the grain boundary mobility (*boundary kinetics*) and the equilibrium angle θ can be expressed as:

$$\theta_{eq} = \arccos\left(\frac{\Delta\gamma^s_L}{\gamma_b} \right). \tag{4.8}$$

The state of the motion of the boundary with the surface junction can be determined experimentally by the measurement of the contact angle θ.

Notice that there is another way to analyze steady-state motion of grain boundaries with respect to the controlling kinetics, i.e. boundary or surface junction control. Since the grain boundary migration is a drift motion to reduce the total free energy of the system, the boundary velocity V has to be proportional to the driving force P:

$$V = m_b P. \tag{4.9}$$

The linear relation between the boundary velocity and the driving force was confirmed in many experiments for both: planar grain boundaries moved by a small magnetic driving force [36] and for curved grain boundaries in bicrystals with half-loop geometry [37, 38]. According to Eq. (4.6) junction velocity V_{tj} does not change with the driving force and, therefore, for $V_{tj} < V_b$ there will be no linear relationship between the boundary velocity and the driving force.

4.1.2 Effect of "top/bottom" STJ on boundary migration

The parameter Λ, however, cannot be utilized to examine the influence of the "top/bottom" triple junctions. As mentioned in Chapter 3, the grain boundary shape is an important source of knowledge on grain boundary properties. Simple qualitative analysis of the grain boundary shape on the lateral surface ("lateral" junction line) can be successfully applied to check the possible drag effect of the "top/bottom" junction.

If that junction affects grain boundary motion, the "lateral" junction line will not run straight through the thickness of the bicrystal, but because of the drag effect on the "top/bottom" surfaces it becomes curved in the direction of the boundary motion. In this case, the velocity of moving grain boundary changes through the specimen thickness δ: $V = V(z)$, where the z-axis is perpendicular to the xy plane (Fig. 4.1). We stress that in such a complicated situation the grain boundary motion cannot be considered as quasi-two-dimensional problem and, as is demonstrated below, a 3-dimensional shape analysis has to be applied.

4.1.3 Groove dragging

Moving grain boundary also forms another surface defect at the line of its intersection with a free surface – a thermal groove. The displacement of this defect requires an additional mass transport and consequently energy dissipation, which makes itself felt as a drag force on the boundary.

The effect of the surface groove on grain boundary motion was first understood by Mullins [39, 40]. He maintained the principal assumption that the angle θ at the root of a groove remains constant during grain boundary motion and is determined by the equilibrium values of the energy of grain

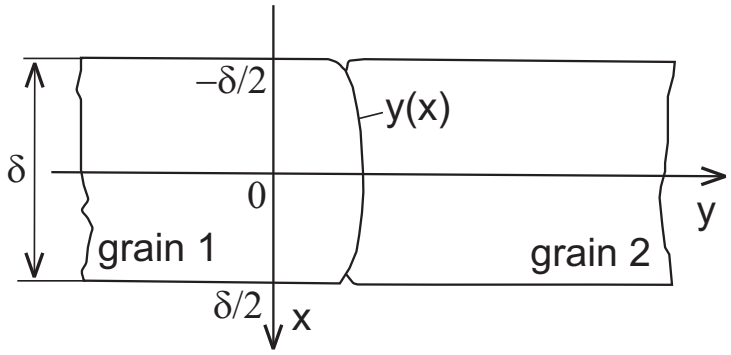

Figure 4.2: Shape $y(x,t)$ of grain boundary (through the thickness of specimen) under the action of a driving force for migration and surface grooves

boundary and a free surface. However, the evolution of thermal groove contributes to the change of the angle θ. A different approach was proposed by Shvindlerman et al. [41]. The equation of motion of a uniform isotropic boundary under the action of a driving force P and a curvature K can be written

$$\dot{y} = m_b \left(P - \gamma_b K\right) \frac{ds}{dx},$$
$$\dot{y} = m_b \left\{ P + \gamma_b y'' \left[1 + \left(y'\right)^2\right]^{3/2} \right\} \left[1 + \left(y'\right)^2\right]^{1/2}, \tag{4.10}$$

where s is the line element, $y(x,t)$, $-\delta/2 \leq x \leq \delta/2$, is the function describing the shape of the boundary, δ is the thickness of the specimen (Fig. 4.2). For a moderately curved boundary $(y')^2 \ll 1$ and Eq. (4.10) simplifies to

$$\dot{y} = m_b \left(P + \gamma_b y''\right), \tag{4.11}$$

with three boundary conditions

$$y(-\delta/2, t) = y(\delta/2, t),$$
$$y'(0,t) = 0,$$
$$V_y = \dot{y}(-\delta/2, t) + V_x y'(-\delta/2, t), \tag{4.12}$$

where V_y is the horizontal and V_x is the vertical velocity component of the bottom of the groove (Fig. 4.3a). The first two conditions are dictated by

the symmetry of the system and the last is due to coincidence of the bottom of the groove and the terminal of the boundary. To determine the velocities V_y and V_x, we should consider the thermal groove evolution: its formation, growth and migration.

In general form, the kinetics of groove formation in a steadily moving coordinate system with a grain boundary is given by

$$\dot{Y} = \frac{\delta Y}{\delta t} + V_x Y^{'},$$
$$\dot{Y} = -\Omega_a \left(J_s + J_g + J_v\right) \left[1 + \left(Y^{'}\right)^2\right]^{-1/2} + V_x Y^{'}, \tag{4.13}$$

where $Y(x,t)$ is the shape of the groove (Fig. 4.3b), Ω_a is the atomic volume, $J_s(x,t)$ is the surface diffusion flux, $J_g(x,t)$ is the flux of atoms carried through the gas phase perpendicular to the surface, $J_g(x,t)$ is the vacancy diffusion flux through the crystal, $V_x Y^{'}$ is the convection flux due to the moving coordinate system. The magnitude of each flux depends on the shape of the surface in the vicinity of the groove. The equilibrium at the bottom of the thermal groove (Fig. 4.3b) requires

$$\gamma_s = (\cos\theta_+ - \cos\theta_-) = \gamma_b \sin\theta,$$
$$\gamma_s = (\sin\theta_+ - \sin\theta_-) = \gamma_b \cos\theta. \tag{4.14}$$

The increment of $\tan\theta$ consists of two parts [41], the first due to the change of the slope of the boundary and the second due to the increasing depth of the groove

$$\frac{d\left(\tan\theta\right)}{dt} = y^{'}\left(-\delta/2, t\right) + V_x^{''}\left(-\delta/2, t\right). \tag{4.15}$$

Assuming that the specimen is quite "thick" ($h/\delta \ll 1$), where h is the depth of the groove, one obtains by integration

$$\theta \cong \tan\theta = y^{'}\left(-\delta/2, t\right). \tag{4.16}$$

Due to its mathematical complexity, the problem was only solved in approximation of "symmetrical groove" [41]. In this case the shape of a moving groove was replaced by the shape of a groove at unmovable grain boundary and the motion of a boundary groove was considered analogically to the motion of a pore in a solid. The velocity of the groove can be written as

$$V = m_g \gamma_b \sin\theta, \tag{4.17}$$

where m_g is the mobility of the grain boundary groove. The function $m_g(t)$ can be determined from the following. At the beginning of the motion the smooth, flat surface does not drag the boundary motion, that means $m_g(t) \rightarrow \infty$. As the groove grows, the mobility $m_g(t)$ decreases and the surface section of the boundary begins to move slower than that in the specimen interior. As a result, the boundary becomes tilt with regard to the specimen surface. Once it exceeds a certain critical angle it can detach from the groove without increasing its own area. This is achieved when the angle between the tangent to the boundary at the surface and that to the surface of the crystal at the bottom of the groove is 90°. Strictly speaking, such a situation is impossible if the angle between the free surfaces and the grain boundary is in equilibrium. However, a slight change of the groove shape makes this situation possible and the boundary can detach from the groove. The mechanism of this process is also given in [41].

Since the velocities $\dot{y}(x,t)$ of different points of the boundary differ very little, the boundary can be considered to move as a whole with a velocity $V = \dot{y}(x,t)$. Integration of Eq. (4.11) leads to

$$\int_{-\delta/2}^{\delta/2} \dot{y}(x,t)dx = m_b \left\{ P\delta + \left[y^{'}(\delta/2,t) - (-\delta/2,t) \right] \gamma_b \right\}. \tag{4.18}$$

Replacing $\dot{y}(x,t)$ by $V(t)$ and utilizing Eqs. (4.10) and (4.16) we obtain boundary velocity

$$V(t) = \frac{Pm_b}{1 + \frac{2m_b}{\delta m_g(t)}}. \tag{4.19}$$

Eq. (4.19) describes the velocity of the boundary with a thermal groove. It is evident from this equation that the joint motion of the boundary and the groove depends on the mobility of the boundary m_b, the mobility of the groove m_g and the specimen thickness δ. The boundary is able to detach from the groove if it flexes to the angle θ that exceeds the critical angle $\theta_c = \pi/2 - \theta_-$ (Fig. 4.3b).

Thus, the criterion ρ reflects the state of the grain boundary motion:

$$\rho = \frac{2P\delta}{\gamma_b \theta_c} \geq 1. \tag{4.20}$$

In a "symmetrical groove" approximation, the critical angle θ_c can be estimated as

$$\theta_c = \arcsin \frac{\gamma_b}{2\gamma_s}. \tag{4.21}$$

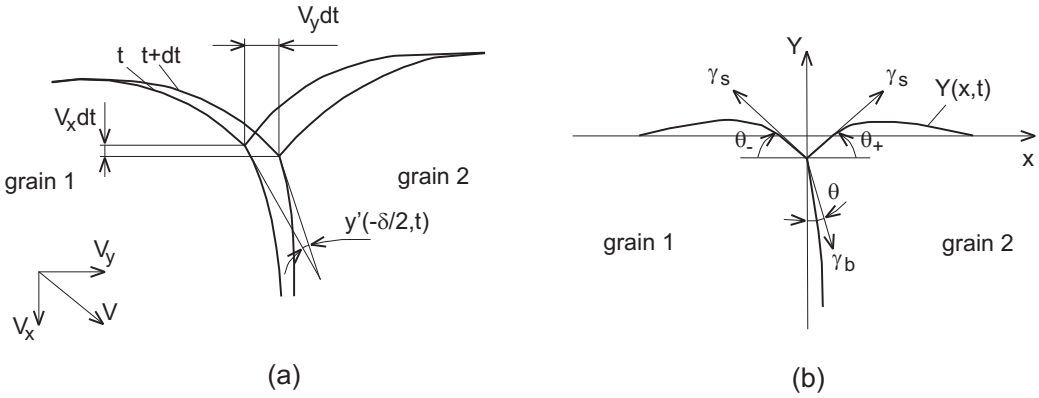

Figure 4.3: (a) Variation of the surface profile during grain boundary migration with formation of a thermal groove. (b) Forces equilibrium due to surface and grain boundary tension

If Eq. (4.20) is satisfied, the boundary moves detached from the groove. In our experiments the specimen thickness was δ=2 mm, the driving force $P = \gamma_b/a$, where $\gamma_b \cong 0.5$ J/m^2, $a \cong 0.5$ mm. Assuming $\gamma_s/\gamma_b \cong 3$,

$$\rho = \frac{2P\delta}{\gamma_b \arcsin\left(\frac{\gamma_b}{2\gamma_s}\right)} \approx 50, \tag{4.22}$$

i.e. the boundaries in our migration experiments move unaffected by the thermal groove.

The mobility of the groove $m_g(t)$ is determined by the controlling mechanism of the groove development and can be calculated if this mechanism is known. In [41] a groove evolution by the surface diffusion was considered.

4.2 Experimental

The migration of quarter-loop shaped grain boundaries was investigated in Al-bicrystals of high purity (99.9995 wt. %, Al I, see Appendix A). The bicrystal geometry (Fig. 3.6b) and the peculiarities of the migration of mixed tilt-twist grain boundaries have been discussed in Chapter 3. In the present research the motion of mixed tilt-twist grain boundaries with the rotation axis <111> and misorientation angles θ of 37.5°, 39.9° and 40.6° was examined.

Such bicrystal geometry was chosen since the orientation contrast by backscatter electrons in a SEM is much better from a bicrystal with a mixed boundary than from a bicrystal with a tilt boundary and since no essential difference was also found for the motion of both curved tilt and curved mixed tilt-twist boundaries (Chapter 3). The shape of moving grain boundary was recorded in-situ utilizing SEM set-up described in Chapter 2. The dependence of the grain boundary velocity on driving force was measured in real-time by X-ray diffraction equipment (XICTD, Chapter 2). It is stressed that due to the symmetry of the initial flat boundary there is only a very slight difference in the (specific) surface energies of the corresponding crystal surfaces (top/bottom and lateral).

4.3 Migration of <111> mixed grain boundaries in Al-bicrystals

The migration of mixed 37.5°, 39.9°, 40.6° <111> grain boundaries was studied. The angle θ was recorded as a function of time for several temperatures (Fig. 4.4). The contact angle θ as a function of time is shown in Fig. 4.5. For all investigated boundaries the velocitiy V and the angle θ were found to be constant at a given temperature in the entire investigated temperature range. Evidently, the assumption of a steady-state motion of the grain boundary was justified.

It is obvious from Fig. 4.6a that θ does not change with increase of temperature. The criterion Λ, determined by Eq. (4.7) was also found to be constant for a given temperature and does not increase with temperature (Fig. 4.6b).

In general, there are two possible reasons for the change in the angle θ with the temperature. Firstly, the angle θ can change due to temperature dependence of surface energies γ_b and γ_s. This dependence, however, is known to be very slight hence the impact of surface energy variance on the contact angle θ can be neglected. Secondly, surface junction drag on the lateral surface may affect the steady-state motion, and, accordingly, the steady-state value of θ. The drag effect is described in terms of the criterion Λ. For all temperatures, used in this study, the criterion Λ was equal to $\Lambda = 22$ for the 37.5° <111> grain boundary and $\Lambda = 19$ for the 40.6° <111> grain boundary (Fig. 4.6b). This shows that $m_{tj}a \gg m_b$ and the "lateral" triple junction does

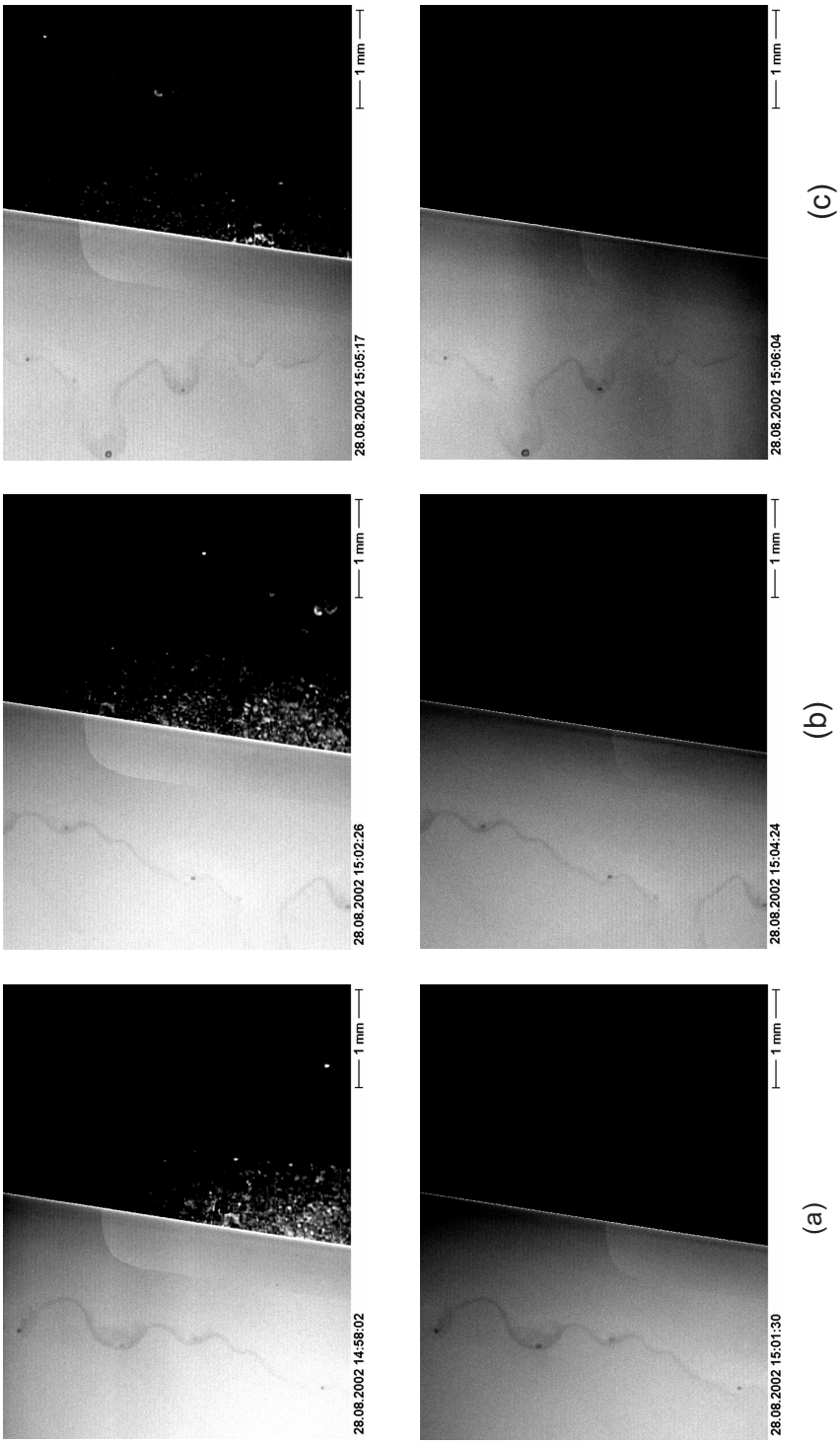

Figure 4.4: Boundary shape for a moving 37.5° <111> grain boundary at different temperatures: (a) 440°, (b) 460°, (c) 480°. Top micrograph corresponds to starting boundary position, bottom – final position

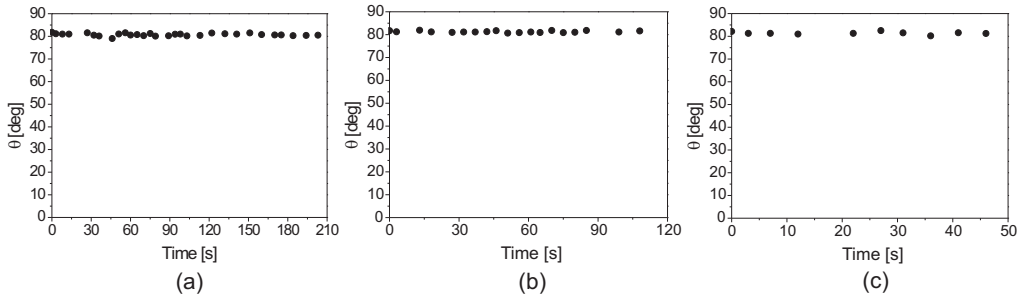

Figure 4.5: Measured contact angle θ vs. time for 37.5° <111> grain boundary for different temperatures (a) 440°C, (b) 460°C, (c) 480°C

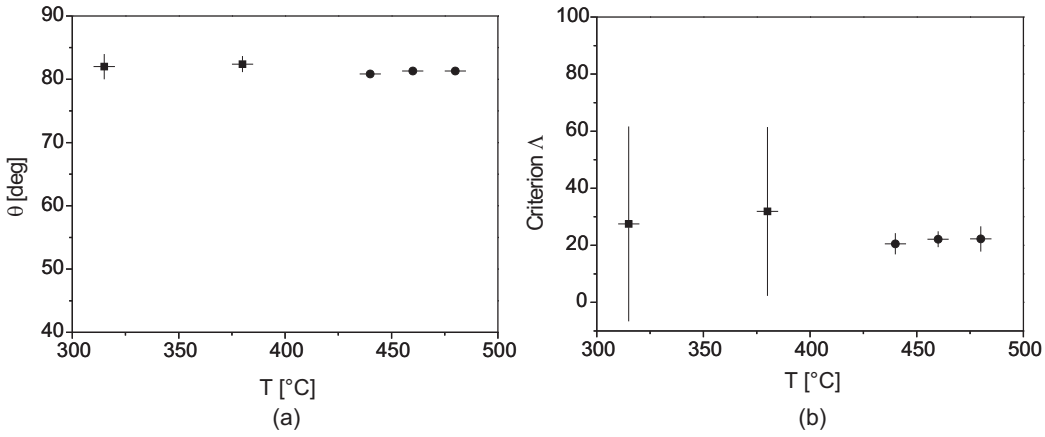

Figure 4.6: (a) Contact angle θ and (b) calculated parameter Λ vs. temperature (circles – 37.5° <111> grain boundary, squares – 40.6° <111> grain boundary

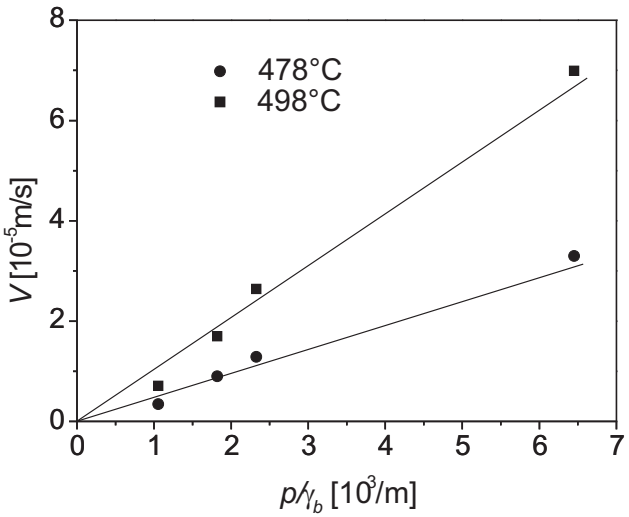

Figure 4.7: Measured grain boundary velocity of a 39.9° <111> boundary vs. driving force

not affect the boundary motion in the entire investigated temperature range.

As mentioned above, to analyze the motion of the curved grain boundary with respect to the controlling kinetics, the boundary velocity was also measured as a function of the driving force. The different driving forces were achieved by utilizing specimens with different widths y_1 of the disappearing grain ($y_1 = 155 \div 950\ \mu m$) (Fig. 4.1). The experiments revealed that the grain boundary velocity at a given temperature rises in linear proportion to the driving force (Fig. 4.7). This proportionality substantiates that the boundary motion is not affected by any surface junction ("top/bottom" or "lateral"), this also reinforces the assumption that the entire boundary system moves in the steady-state.

Since Λ fails to reveal the possible influence of the "top/bottom" triple junctions, the "lateral" junction line was examined. After grain boundary mobility measurements were taken, the specimen was rapidly cooled to the room temperature and the "lateral" line was recorded. This line was straight in all experiments (Fig. 4.8). This observation manifests that the "top/bottom" surface junctions do not affect the motion of the grain boundary as well as the "lateral" surface triple junction in the investigated temperature range.

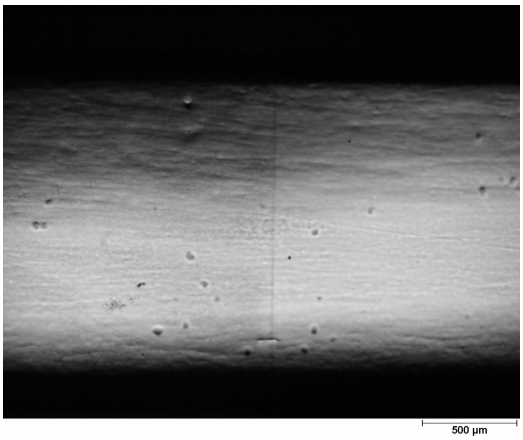

Figure 4.8: Lateral surface of Al-bicrystal with 39.9° <111> boundary

It is reasonable to question whether the magnitude of Λ ($\Lambda = 22$ and $\Lambda = 29$) is high enough to guarantee a drag-free grain boundary motion, or, to what extent the boundary migration depends on the junction mobility. Substituting Eq. (4.8) into (4.7)

$$\frac{1}{\Lambda} = \frac{\cos\theta + (\Delta\gamma_s/\gamma_b)}{\theta} = \frac{\cos\theta - \cos\theta_{eq}}{\theta}, \tag{4.23}$$

and expanding $1/\Lambda$ into a power series in the vicinity of θ_{eq} and neglecting the terms higher than the 2^{nd} order, we derive

$$\frac{1}{\Lambda} = \frac{(\theta_{eq} - \theta)\sin\theta_{eq}}{\theta}, \tag{4.24}$$

and, finally,

$$\theta = \theta_{eq} - \frac{\theta_{eq}}{\sin\theta_{eq}}\frac{1}{\Lambda}. \tag{4.25}$$

From Eqs. (4.5) and (4.25) the ratio of the boundary velocities for the motion "affected" and "unaffected" by surface triple junction is derived:

$$\lambda = \frac{V_{\Lambda=\infty}}{V_{\Lambda\neq\infty}} = \frac{\theta_{eq}}{\theta_{eq} - (\theta_{eq}/\sin\theta_{eq})\,(1/\Lambda)} = \frac{1}{1 - (1/\sin\theta_{eq})\,(1/\Lambda)} = \frac{\Lambda}{\Lambda - 1}. \tag{4.26}$$

This equation allows us to quantify the extent of the triple junction drag on the grain boundary motion. For instance, for the motion of the 40.6° <111>

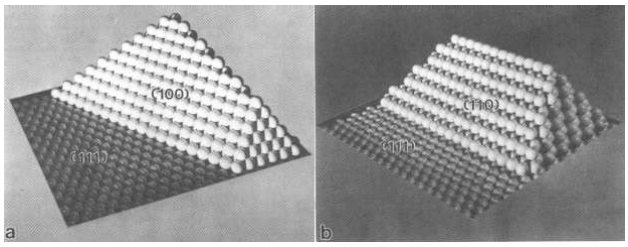

(a) (b)

Figure 4.9: Hard sphere models of (a) the {111} and {100}, (b) {110} crystal surfaces for an FCC metal

boundary in the present experiments ($\Lambda = 29$) the drag effect did not exceed $\lambda = 4\%$.

4.4 Motion of solitary grain boundaries in Al-bicrystals with strong anisotropy of external free surface

4.4.1 Anisotropy of surface energy. Correlation of surface energy with surface orientation

From previous studies summarized in [5] it is clear that the surface energy of a solid varies as a function of the crystal surface orientation. The dependence of the surface energy on the surface structure can be demonstrated in terms of a hard-sphere model in cubic metals. If the surface is parallel to a low-index crystal plane, the atomic arrangement of the planes can be assumed to be the same as in a bulk, except for a small change in the lattice parameter. The hard-sphere models of the {111}, {100}, and {110} crystal planes are shown in Fig. 4.9. Except for the close packed {111} plane, the atom density in FCC metals generally decreases as the {hkl} Miller indexes of the plane increases. The surface energy of a pure solid FCC metal can be calculated using a simple nearest-neighbor broken-bond model of the surface under the following assumptions:

1. Each atom has z nearest neighbors and only the energies of the nearest

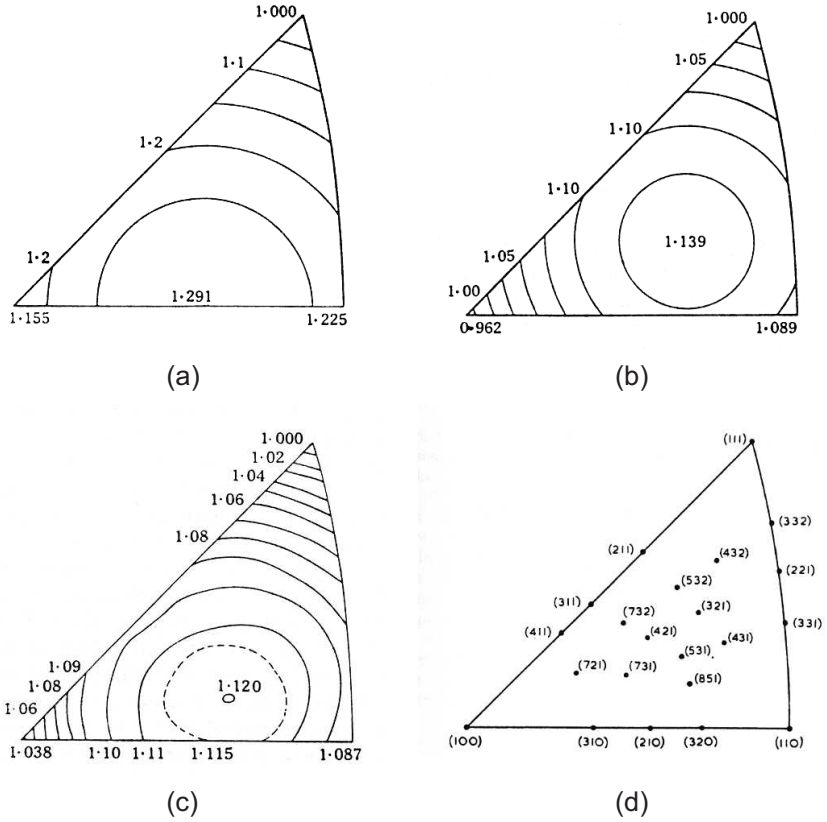

Figure 4.10: Theoretical contour plots of surface energy for an FCC crystal when (a) nearest-neighbor, (b) second-nearest neighbor and (c) many-neighbor interactions are considered. (d) Stereographic plot of the normals to the surfaces for a cubic structure

neighbors are considered.[2]

2. Each bond has an energy ϵ_b, which does not depend on temperature

3. The energy of each bond is determinded by

$$\epsilon_b = 2\Delta H_s / zN_A, \tag{4.27}$$

where ΔH_s is the heat of sublimation, z - the number of bond, N_A - Avogadro's number.

4. The enthalpies and internal energies are equal.

The broken-bond approach can be utilized to estimate the energy of any {hkl} crystal surface. Let us consider {111} plane in FCC crystal with z=12 (Fig. 4.9a). There are six nearest neighbors in the plane, three atoms above the plane and three below. In result, three bonds are broken for each surface atom when the crystal is separated forming two {111} planes. Therefore, every surface atom has an excess internal energy of $3\epsilon_b/2$ over the atom in the bulk. Correspondingly, the energy of a {111} surface is

$$E_{\{111\}} = \frac{3\epsilon_b}{2} = \frac{3\Delta H_s}{12N_A} = \frac{\Delta H_s}{4N_A}, \tag{4.28}$$

if there are $N_{s\{hkl\}}$ atoms per unit surface and there are no surface strains, the (specific) surface free energy is

$$\gamma_{111} = N_{s\{111\}} E_s = N_{s\{111\}} \frac{\Delta H_s}{4N_A}. \tag{4.29}$$

Similarly, we obtain for {100}

$$\gamma_{100} = N_{s\{100\}} E_s = N_{s\{100\}} \frac{\Delta H_s}{3N_A} \tag{4.30}$$

and for {110}

$$\gamma_{110} = N_{s\{110\}} E_s = N_{s\{110\}} \frac{\Delta H_s}{2N_A}. \tag{4.31}$$

As can be seen from Eqs.(4.29 – 4.31) the (specific) surface energy of a {110} surface is higher than that of a {100} surface , which is higher than that of a {111} surface. A convenient way to display surface energy data is to use so called γ-plot (Fig. 4.10). According to Fig. 4.10 the difference in surface energies between the {111} and {110} planes is about 20% considering nearest-neighbor and is about 10% considering many-neighbor interactions.

[2] z is also called as coordination number

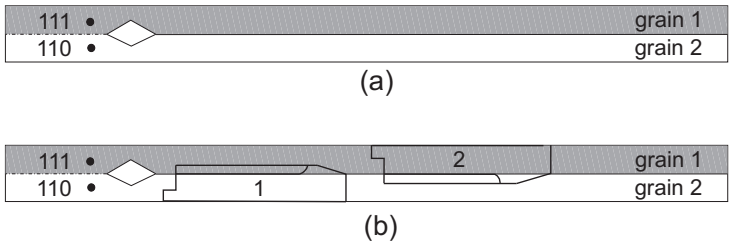

Figure 4.11: Scheme of (a) grown bicrystal and (b) specimen preparation

4.4.2 Experimental

As shown above, the maximum difference of about 10-20% in the (specific) surface energy is achieved between {110} and {111} external surfaces in FCC metals (Fig. 4.10). Al-bicrystals (99.9995 wt. %, Al I, see Appendix A) were grown from single crystal seeds which had {110} and {111} planes parallel to the seed planes (Fig. 4.11). Two types of specimens were investigated. We characterize them in terms of the normal to the shrinking grain: *configuration 1* with <111> normal to the shrinking grain and *configuration 2* with <110> normal to the shrinking grain (Fig. 4.12). It was expected that in accordance with Eq. (4.4) the boundary would demonstrate difference in the shape (with the contact angle over then 90° in configuration 1 and less then 90° in configuration 2). We describe disorientation between two crystallites in terms of rotation axis and misorientation angle. Thus, the planar boundary between grain 1 and grain 2 (Fig. 4.11) is an asymmetrical <112> *tilt* grain boundary with the misorientation angle of 90°. In its curved part (Fig. 4.12) the boundary acquires mixed tilt-twist character.

The migration of the mixed grain boundary in both types of specimens was studied by a quarter-loop technique. Over 20 specimens from 10 bicrystals were measured. The orientation contrast in an SEM was utilized to reveal the shape and the position of the moving boundary. In the studied bicrystal configuration a large difference in surface energies attained on both: on the top (or bottom) and on the lateral surfaces of the specimen.

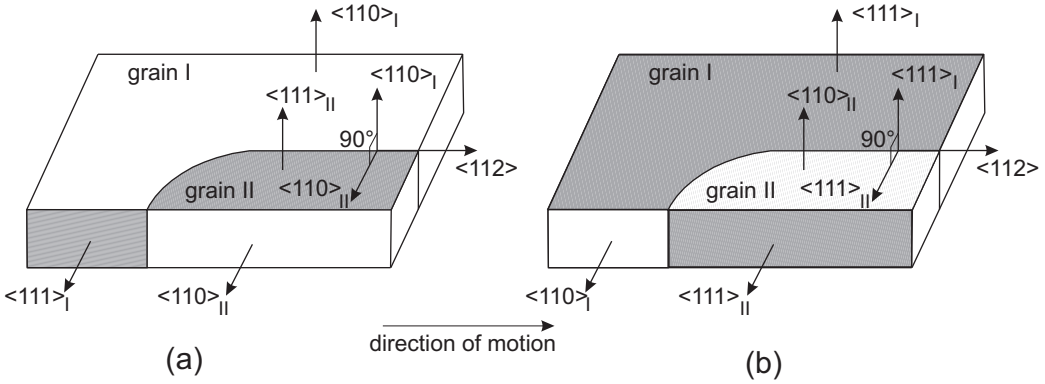

Figure 4.12: Bicrystal with <112> mixed grain boundary in (a) configuration 1 and in (b) configuration 2. Surfaces parallel to {111} planes are shown in gray color

4.4.3 Migration of <112> mixed grain boundaries in Al-bicrystals

The motion of <112> mixed grain boundaries in bicrystals with strong surface anisotropy was studied. The behavior of the grain boundary motion in those bicrystals is essentially different from the grain boundary motion investigated in our experiments and in previous studies. Some peculiarities of grain boundary migration were observed, which had not been reported so far.

The grain boundary shape changed continuously when the temperature in the experiment increased. The grain boundary motion is considered in details for both bicrystal configurations below.

Boundary motion in bicrystals of configuration 1

Contrary to our expectations, the shape of the moving grain boundary depends on the temperature (Figs. 4.13a, 4.13b). The shape was analyzed with respect to the contact angle θ. The same tendency was also observed in different specimens at the same temperature (Fig. 4.13c, 4.13d). The measurement results are summarized in Fig. 4.14 and in Tabl. 4.1. One can see that contact angles over 90° and below 90° were observed. A temperature increase can lead to both a decrease and an increase in the contact angle. At

Table 4.1: Measured contact angle and calculated absolute grain boundary mobility (assuming γ_b=0.5 J/m^2) in configuration 1

specimen	T [°]	m_b $[J^4/m^2s]$	angle θ [°]
4_1	400	$5.18 \cdot 10^{-10}$	63
	420	$2.30 \cdot 10^{-10}$	61
	440	$4.27 \cdot 10^{-9}$	61
6_1	450	$5.57 \cdot 10^{-9}$	86
	500	$1.20 \cdot 10^{-8}$	83
	520	$3.08 \cdot 10^{-8}$	96
7_1	520	$4.90 \cdot 10^{-8}$	89
18_2	440	$1.93 \cdot 10^{-9}$	69
	460	$5.85 \cdot 10^{-9}$	74
	480	$9.44 \cdot 10^{-9}$	74
19_2	420	$5.46 \cdot 10^{-10}$	69
	440	$1.92 \cdot 10^{-9}$	67.5
	460	$2.74 \cdot 10^{-9}$	68
	480	$7.53 \cdot 10^{-9}$	67
	500	$2.38 \cdot 10^{-8}$	64

constant temperature *no change* in the contact angle and accordingly in the shape was observed (Fig. 4.17a). The velocity of he moving grain boundary was also constant at a given temperature (Fig. 4.17b).

Boundary motion in bicrystals of configuration 2

The character of the grain boundary motion observed in configuration 2 was similar to that in configuration 1: the contact angle changes randomly with an increase in temperature (Fig. 4.15), no change in boundary shape and velocity was discovered at a constant temperature (Fig. 4.18).

Effect of surface anisotropy on grain boundary migration

The experiments revealed that grain boundaries in considered bicrystal configurations move in *steady-state* at a given temperature; the boundary did not change its shape and the grain boundary velocity was constant at a fixed temperature. However, a change in the temperature led to an immediate change

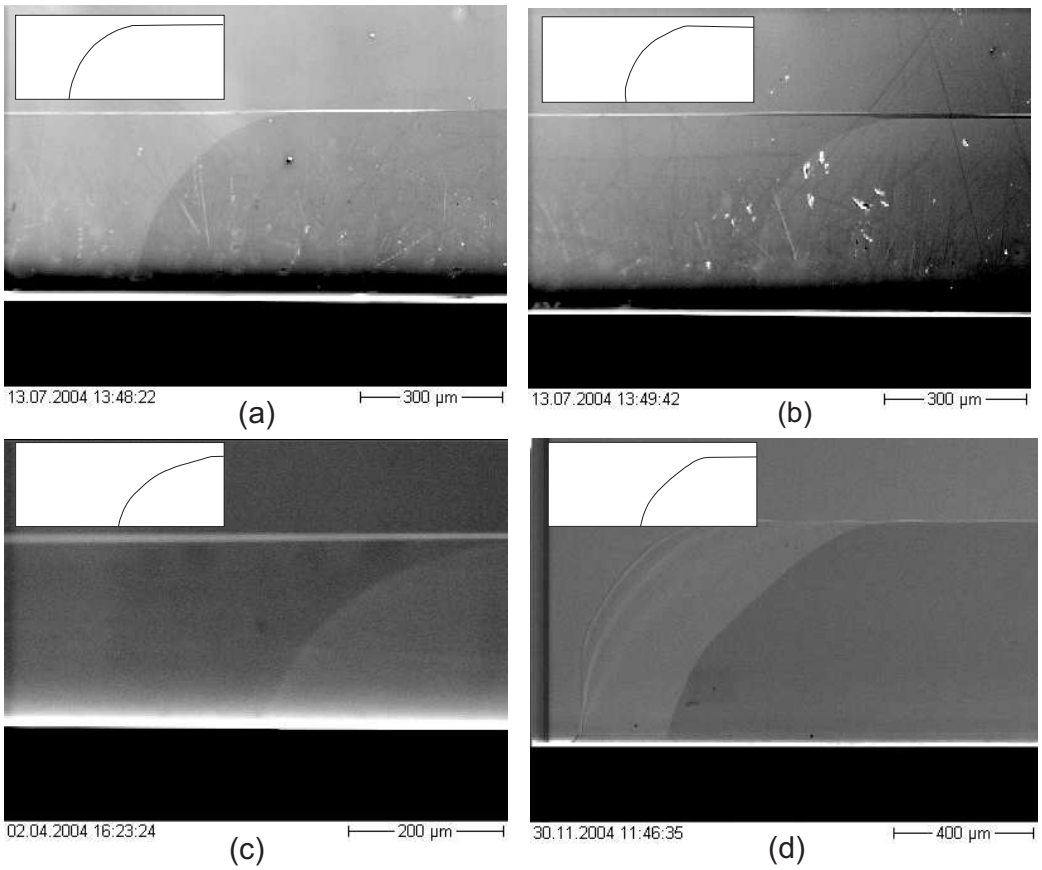

Figure 4.13: Grain boundary shape (SEM images and sketches) in specimen 6_1 at (a) 500°C ($\theta = 83°$) and (b) 520°C ($\theta = 96°$) and at 420°C in specimens (c) 4_1 ($\theta = 61°$) and (d) 18_2 ($\theta = 69°$) in configuration 1

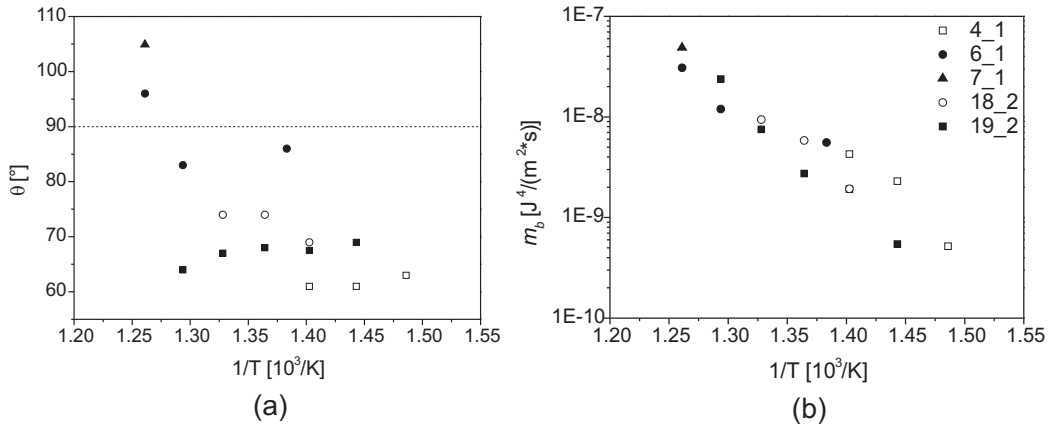

Figure 4.14: (a) Measured contact angle θ and (b) calculated absolute grain boundary mobility m_b for $\gamma_b = 0.5\ J/m^2$ vs. temperature in configuration 1

Table 4.2: Measured contact angle and calculated absolute grain boundary mobility (assuming γ_b=0.5 J/m^2) in configuration 2

specimen	T [°]	m_b $[J^4/m^2s]$	angle θ [°]
11_2	400	$4.63 \cdot 10^{-10}$	67
	420	$1.17 \cdot 10^{-9}$	64
	440	$2.94 \cdot 10^{-9}$	62
	460	$5.16 \cdot 10^{-9}$	61
	480	$1.00 \cdot 10^{-8}$	60
18_1	460	$8.68 \cdot 10^{-9}$	91
	480	$8.99 \cdot 10^{-9}$	95
	500	$1.10 \cdot 10^{-8}$	95
19_1	540	$4.40 \cdot 10^{-8}$	96
21_1	530	$1.23 \cdot 10^{-8}$	82
	550	$2.00 \cdot 10^{-8}$	85

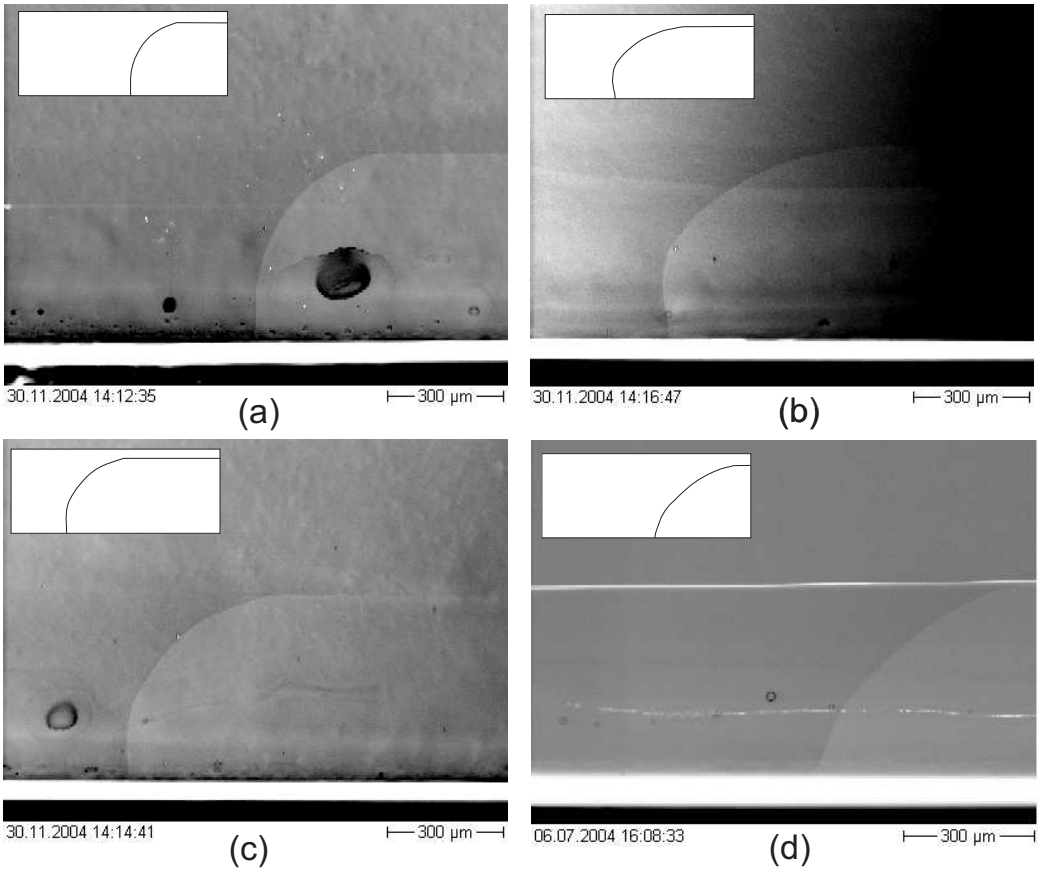

Figure 4.15: Grain boundary shape (SEM images and sketches) in specimen 18_1 at (a) 460°C ($\theta = 91°$) and at (b) 500°C ($\theta = 95°$) and at 480°C in specimens (c) 18_1 ($\theta = 95°$) and (d) 11_2 ($\theta = 60°$) in configuration 2

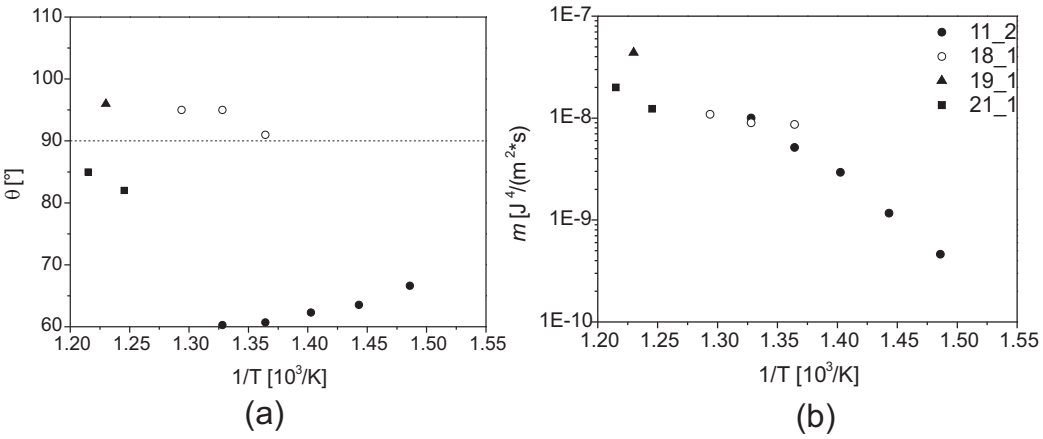

Figure 4.16: (a) Measure Contact angle θ and (b) calculated absolute grain boundary mobility m_b (assuming γ_b=0.5 J/m^2) vs. temperature in configuration 2

of the boundary shape. The measured contact angle reflects this change. One can see that the contact angle changes randomly (Figs. 4.14a, 4.16a). Thus, the shape of the moving grain boundary can not be predicted by Eq. (4.4) in the framework of the model considered above in Paragraph 4.1.1 and more detailed analysis is required.

In our treatment we represent the surface free energy of the system, G^s, as a sum of boundary and surface energies. Note that in the present experiments the boundary demonstrated the complex shape not only on the observed (top) specimen surface, but also on the lateral and bottom ones (Fig. 4.19). The total surface free energy of an isolated, single-component crystalline system is given by

$$G^s = \sum_{i=1} \gamma_i^s A_i + \gamma_b A_b, \tag{4.32}$$

where γ_i^s is the (specific) surface free energy of the i-th crystal face with an area A_i, γ_b is the grain boundary energy, and A_b is the grain boundary area. In our case, the total surface free energy is written as:

$$G^s = S_1^T\gamma_1^T + S_2^T\gamma_2^T + S_1^B\gamma_1^B + S_2^B\gamma_2^B + s_1^L\gamma_1^L + s_2^L\gamma_2^L + A_b\gamma_b + C, \tag{4.33}$$

where S_1^T, S_2^T, S_1^B, S_2^B, s_1^L, s_2^L are the areas of grain 1 and grain 2 on the top, bottom and lateral surfaces of the specimen, γ_1^T, γ_2^T, γ_1^B, γ_2^B, γ_1^L, γ_2^L are

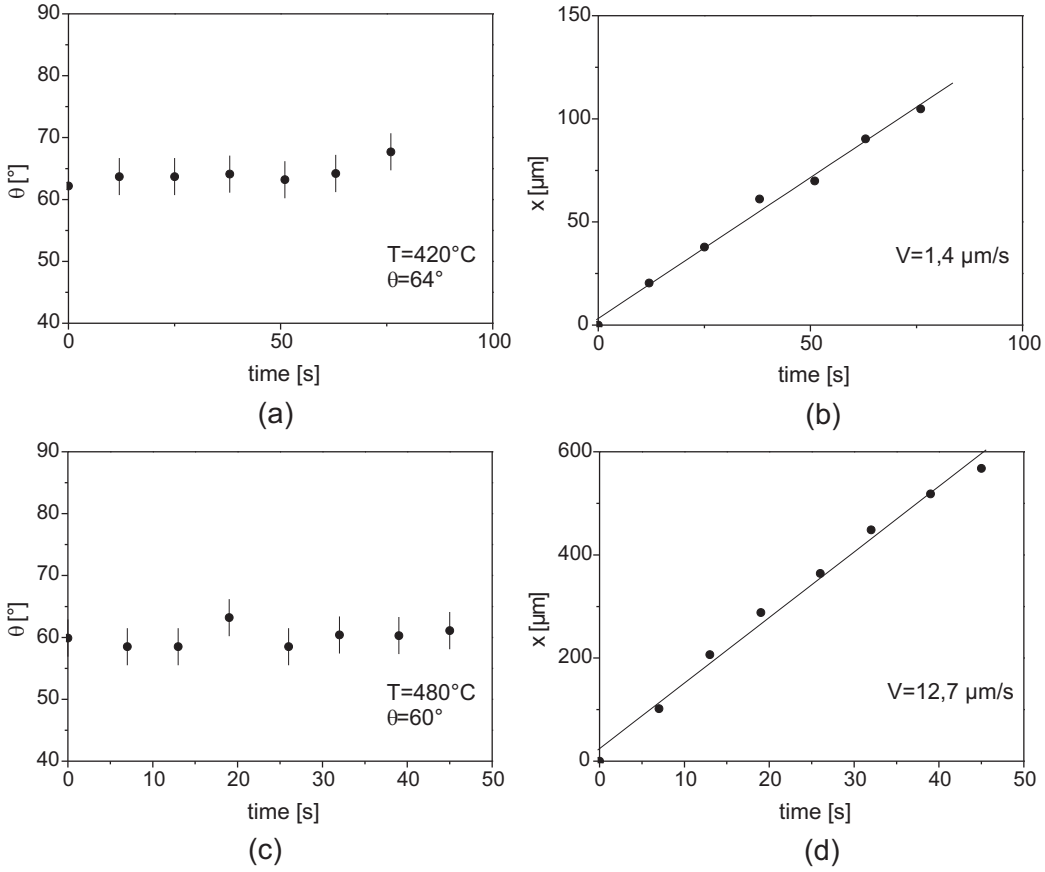

Figure 4.17: Contact angle θ and (b) measured grain boundary velocity for specimen 19_2 (configuration 1) at (a), (b) 420 ° C and at (c), (d) 480 °C

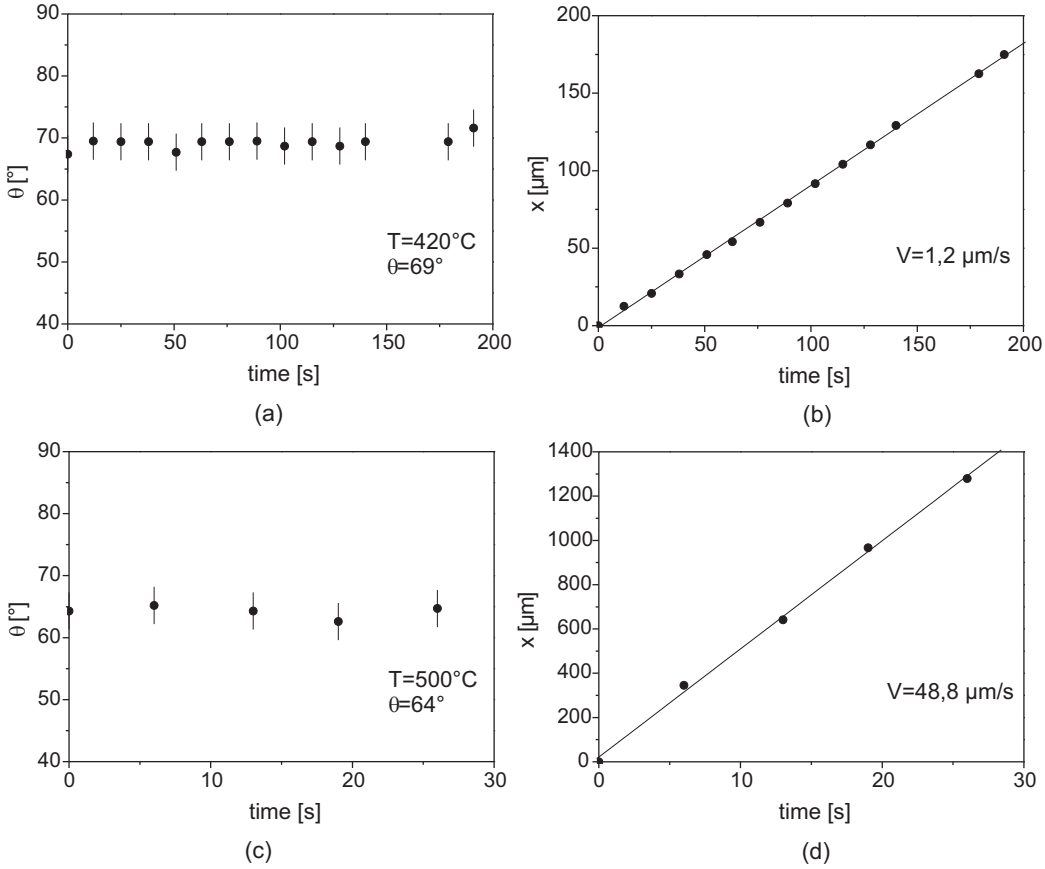

Figure 4.18: Contact angle θ and (b) measured grain boundary velocity for specimen 11_2 (configuration 2) at (a), (b) 420°C and at (c), (d) 500°C

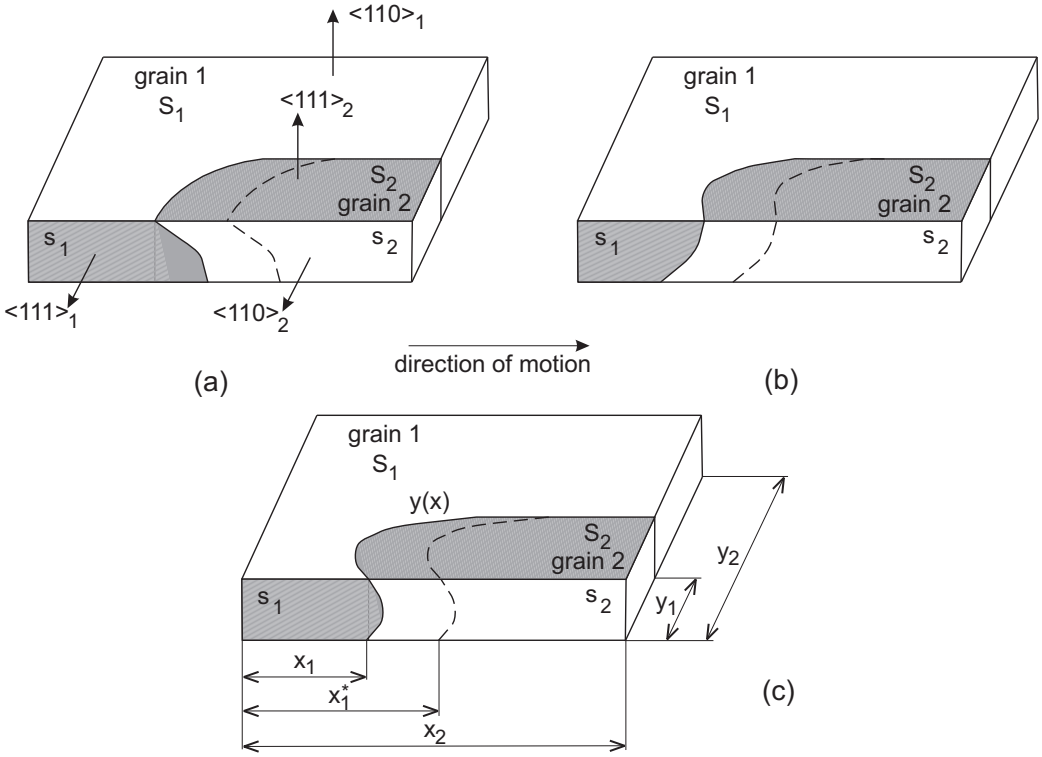

Figure 4.19: Possible shapes of moving grain boundary in bicrystals of configuration 1. Configuration 2 can be considered similar

the corresponding (specific) energies of the external surfaces and the grain boundary ($\gamma_1^T = \gamma_1^B$, $\gamma_2^T = \gamma_2^B$), C is a constant containing part of the surface energy which does not change during grain boundary motion.

The equilibrium state of the system requires a specific minimum in the total free energy. Let us consider the surface free energy of the system G^s as a function of the parameter η, which reflects the shape of the grain boundary and its position in the 3-dimensional crystal. One can see that if the surface free energy changes only slightly in the vicinity of its minimum (Fig. 4.20) there is a range of possible values of η, where the surface free energy of the system is still close to its minimum. Consequently, due to random energy fluctuations there is a number of possible configurations in which the bicrystal system is very close to its equilibrium.

One can imagine that the configurations shown in Fig. 4.19 have the

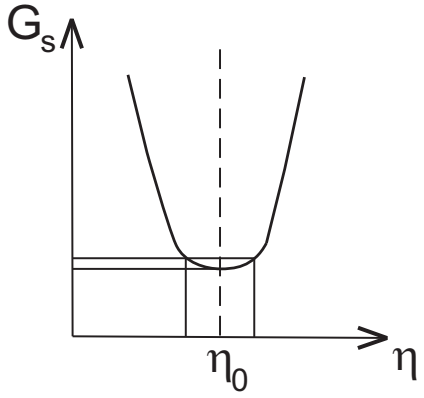

Figure 4.20: Dependence of surface free energy on parameter η representing the shape of grain boundary

same free energies. In this respect the grain boundary can move in any of the shown in Fig. 4.19 or similar configurations. We stress that such unstable equilibrium can be modified easily by a slight change of any thermodynamic parameter (P, T etc). As a result, the increase in the temperature may affect the change of the grain boundary shape.

It should also be noted, that the moving grain boundary holds its shape (and thus "swept volume" δV remains constant) at a given constant temperature and therefore the driving force $P = -\delta G/\delta V$ is constant during the whole process of the grain boundary migration. Since there is a large difference between (specific) surface energies of the neighboring grains in the bicrystal, the diving force cannot be calculated using Eq. (1.17) and the anisotropy of the surface energy must be taken into account. As discussed in Paragraph 1.2.2, the driving force of the grain boundary steady-state motion does not depend on the boundary shape. For the sake of simplicity we derive the equation for the driving force for the "symmetrical" grain boundary motion (Fig. 4.19c). In this case the areas of the correspondent grains on the top and bottom of the crystal are equal: $S_1^T = S_1^B$ and $S_2^T = S_2^B$. The motion of grain boundary causes a decrease in the free energies of the system. This decrease is given by

$$\Delta G = \int_{x_1}^{x_1^*} \left[2\Delta\gamma^T y(x) + \delta\gamma_b \sqrt{1 - y'(x)} \right] dx + \Delta x \delta \Delta y^L, \qquad (4.34)$$

where $\Delta\gamma^T = \gamma_2^T - \gamma_1^T$ and $\Delta\gamma^L = \gamma_1^L - \gamma_2^L$. Consequently, the driving force is:

$$P = -\frac{\Delta G}{V} = -\frac{2\Delta\gamma^T}{\delta} - \frac{\gamma_b}{y_1} + \frac{\Delta\gamma^L}{y_1}. \tag{4.35}$$

Assuming that $\gamma_s \cong 3\gamma_b$, $\Delta\gamma^T = \Delta\gamma^L \cong 0.2\gamma_s$ and $\gamma_b \cong 0.5$ J/m^2 we can estimate the driving force for both bicrystal configurations. Accordingly, $P_1 = -0.6 \cdot 10^3 + 0.8/y_1$ is the driving force for the grain boundary in configuration 1 and $P_2 = 0.6 \cdot 10^3 + 0.3/y_1$ is that in configuration 2.

The calculated mobilities for grain boundary migration in both bicrystal configurations are summarized in Tabls. 4.1, 4.2 and in Figs. 4.14b, 4.16b. Figs. 4.14b, 4.16b demonstrate the scattering of calculated mobilities obtained for the same bicrystal configuration. Such scattering can be explained by the difference in mobility of *differently shaped* grain boundaries.

The question that has not been addressed is the preferable shape of the moving grain boundary. In the steady-state case the motion of the grain boundary is the motion of all segments of the curved boundary together on the top, bottom and lateral surfaces of the specimen. At a line of the surface triple junction formed by the three surfaces (the grain boundary and two external surfaces) the equilibrium is established depending on the corresponding surface energies. Actually, the balance of the acting forces is obeyed on the x-axis only. For the steady-state moving grain boundary the equilibrium condition at the rib OA of the specimen (Fig. 4.21) can be derived for the top/bottom as

$$\gamma_2^L - \gamma_1^L + \gamma_b \cos\theta + \cos\beta = 0 \tag{4.36}$$

and for the lateral surface of specimen as

$$\gamma_2^T - \gamma_1^T + \cos\beta + \gamma_b \cos\theta = 0, \tag{4.37}$$

where the angle β is a grain boundary contact angle on the lateral surface of the specimen. Summation of Eq. (4.36) and Eq. (4.37) gives us:

$$\cos\beta = -\cos\theta. \tag{4.38}$$

Eq. (4.38) determines the equilibrium shape of the moving grain boundary in the steady-state. It links the "lateral" and the "top/bottom" shapes of the grain boundary. Thus, the shape of the grain boundary on the lateral surface of the specimen can be predicted by Eq. (4.38).

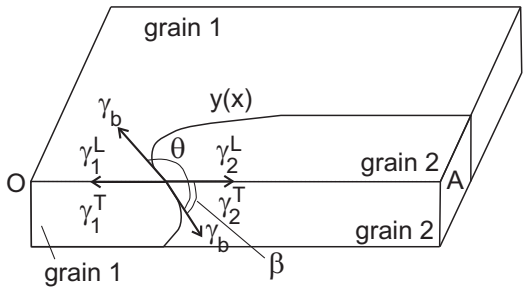

Figure 4.21: Equilibrium shape of moving grain boundary

In the utilized SEM technique simultaneous observation of the top, bottom and lateral surfaces of the specimen is impossible. However, the shape of the boundary can be recorded (by an optic microscope), once the specimen has been cooled. Strictly speaking, the shape of the grain boundary obtained after cooling is different from the one recorded at the last (highest) temperature of the experiment. The specimen was cooled down in the SEM, where a high cooling rate was not possible due to vacuum atmosphere. Therefore, the grain boundary shape recorded after cooling cannot be associated with the shape of the moving grain boundary revealed during in-situ experiments. Nevertheless, in the first approximation the boundary shape after cooling can be considered as an equilibrium boundary shape at an unknown temperature. The shape of the grain boundary recorded by the optic microscope after cooling is shown in Fig. 4.22. The contact angles β and θ were measured experimentally, the contact angle β was also calculated in accordance with Eq. (4.38). The results are summarized in Tabl. 4.3. The observed discrepancy between measured and calculated angle β can be interpreted as due to temperature gradient through the specimen thickness during cooling in vacuum which leads to boundary velocity gradient through the specimen.

This simple analysis shows the relationship between the contact angle on the top/bottom surface of specimen and that on the lateral surface. To define the grain boundary shape unambiguously in a 3-dimensional space, the minimum of surface free energy of the system should be found (Eq. 4.33) and then the analysis discussed above should be applied to the grain boundary in all points where it intersects the external crystal surface. This leads to complex 3-dimensional analysis of the grain boundary shape.

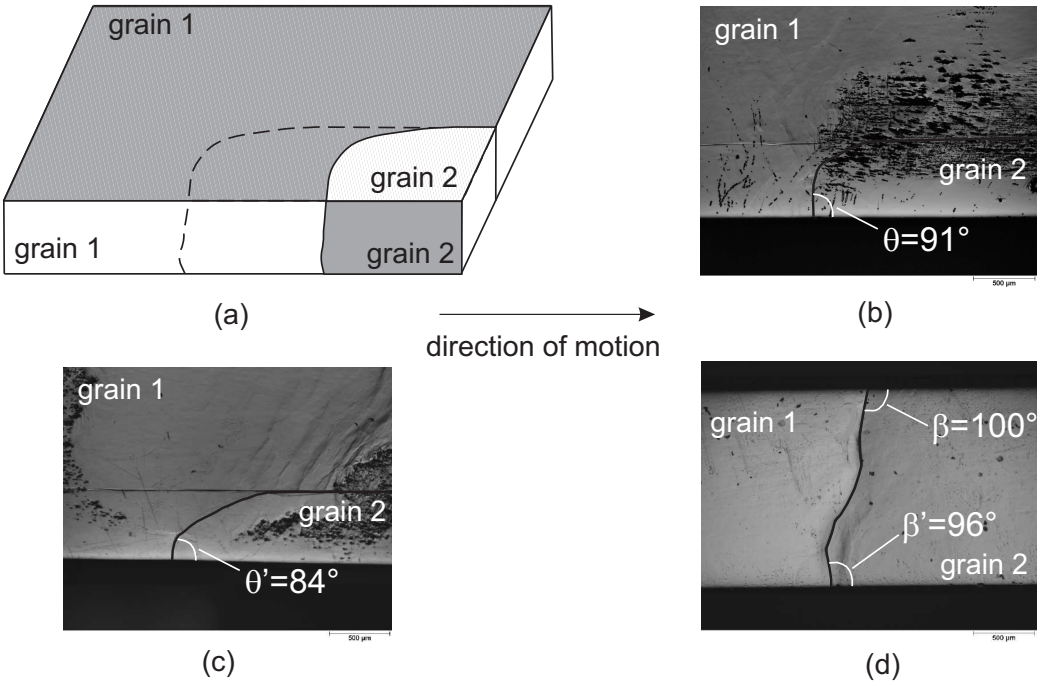

Figure 4.22: (a) Specimen 19_1 (configuration 1) after cooling. Grain boundary shape recorded by the optic microscope on the (b) top, (c) bottom and (d) lateral specimen surface

Table 4.3: Contact angles θ and β for specimen 19_1 (configuration 1) and 7_1 (configuration 2)

specimen	measured		calculated [°]	measured		calculated [°]
	θ^T	β^T	β^T	θ^B	β^B	β^B
19_1	91	100	89	84	96	96
7_1	88	94	92	74	77	103

4.5 Summary

The interaction of the moving grain boundary with an external specimen surface in Al-bicrystals was comprehensively studied. The experiments were carried out on two types of bicrystals: without and with strong anisotropy of the surface free energy.

In the first type of experiments the effect of "surface" triple junction has been addressed. The experiments revealed a linear relationship between the grain boundary velocity and the driving force. This result allows concluding that the velocity of the steady-state grain boundary motion of an initially planar symmetrical <111> tilt boundary in quarter-loop bicrystal geometry is determined by the boundary mobility only and, thus, is not affected by the surface triple junction and by the groove dragging. Measurements of the contact angle at the surface junction and the resulting magnitude of the criterion Λ, which describes the impact of the junction on the boundary motion, confirm this conclusion.

The motion of curved grain boundaries was also studied in bicrystal geometry with a strong anisotropy of the (specific) surface free energy of the adjoining grains. In particular, the migration of an initially planar asymmetrical <112> grain boundary in quarter-loop geometry was investigated. The complex shape of the moving grain boundary was observed. Moreover, the shape of the moving grain boundary changes when the temperature encreases, but it does not change at a constant temperature. The velocity of the moving grain boundary as well as its shape was found to be constant at a constant temperature. This shows that the studied grain boundaries move in the steady-state regime at a constant temperature. The shape of the grain boundary was analyzed with regard to its contact angle on the top/bottom and lateral surfaces of the specimen. The relationship between the contact angle on the top/bottom and on the lateral specimen surfaces was obtained. It was also shown that the moving grain boundary can demonstrate different shapes if the total free energy of the system reaches its minimum.

Chapter 5

Motion of grain boundaries with triple junctions in aluminum tricrystals with different concentration of magnesium

Grain boundaries are the major elements of microstructure of materials. In the course of their motion grain boundaries interact with each other. The lines of intersection of three grain boundaries are called *grain boundary triple junctions* (Fig. 5.1). Although the number of grain boundary junctions is of the same order of magnitude as the number of grain boundaries, the grain growth is usually associated with the motion of grain boundaries, that are not affected by triple junctions. The role of triple junctions has been discussed in interface science for many years. In the first interpretation the role of triple junctions was reduced to prescribe equilibrium angles at the line where the boundaries meet. However, during the last ten years our understanding of the role of triple junctions changed dramatically from pure geometrical concept to the competent structural defect which has own *finite* mobility and may essentially change grain growth kinetics under certain circumstances. Experimental studies on triple junction motion were conducted on both polycrystals and specially manufactured tricrystals. Theories of triple junction migration have been developed. However, many issues remain unexplored. Many of them, like the presence of solute atoms or crystallography of triple junctions, on triple junction drag can be studied in experiments on tricrystal only. In the present work we consider the motion of grain boundaries with

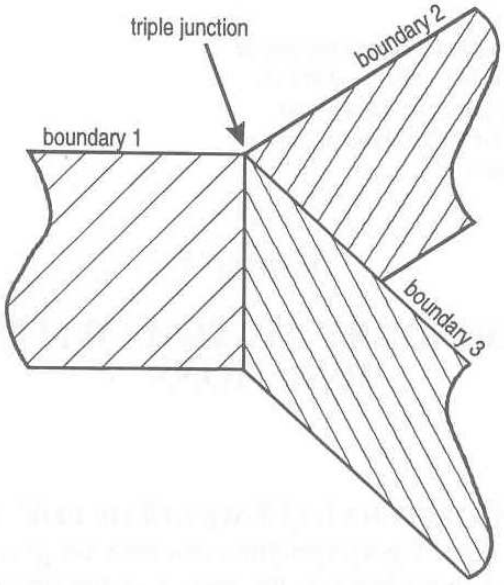

Figure 5.1: Grain boundary triple junction

triple junctions in aluminum tricrystals with different content of solute Mg atoms.

5.1 Triple junction drag theory

The idea that grain boundary triple junctions may have own *finite* mobility was first put forward by Shvindlerman et al. In [42] the concept of specific triple junction mobility was introduced.

The steady-state motion of grain boundaries with the triple junction is only possible in a narrow range of geometrical configurations with specific restrictions imposed on the properties of the grain boundaries. One of such configurations is shown in Fig. 5.2. The triple junction line in Fig 5.2 is perpendicular to the plane of the diagram. Far from the triple junction all three grain boundaries are flat, their planes are parallel to each other and perpendicular to the plane of the diagram. In that case, the problem can be considered as quasi-two-dimensional.

The following assumptions are usually made. The system migrates un-

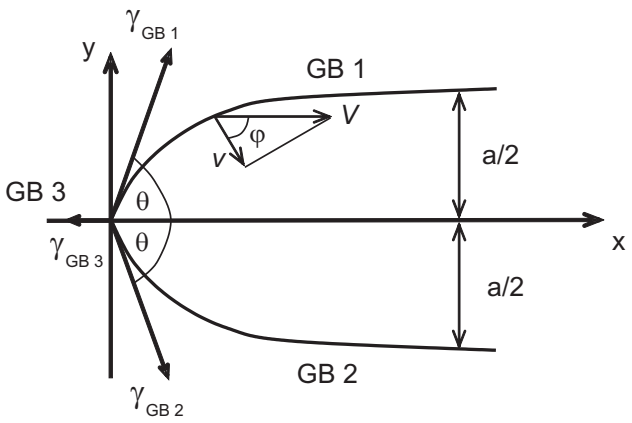

Figure 5.2: Grain boundary system with triple junction in coarse of steady-state motion

der the action of a driving force which is provided by the energy γ_b of the curved grain boundaries. The system is considered either as uniform or as symmetrical. In a uniform system all three grain boundaries possess equal energies and mobilities. A symmetrical system has two identical curved grain boundaries GB 1 and GB 2 and a different straight boundary GB 3. In what follows we consider a symmetrical system, since nowadays it is usually used in the majority of tricrystal experiments. The relationships between respective grain boundary energies and mobilities are given by

$$\begin{aligned} \gamma_{GB1} = \gamma_{GB2} \equiv \gamma_b \neq \gamma_{GB3}, \\ m_{GB1} = m_{GB2} \equiv m_b \neq m_{GB3}. \end{aligned} \tag{5.1}$$

The given assumptions imply the system symmetry along the x-axis. The problem of the shape of moving grain boundaries in this case is identical to the problem of the shape of a single grain boundary in a bicrystal discussed earlier in Chapter 3 (Eqn. (3.10), (3.12). Therefore, the analysis of Chapter 3 applies here as well. Since grain boundaries move together with a triple junction, the driving force applied to the triple junction can be written as[1]

$$P = \gamma_b \left(2\cos\theta - \frac{\gamma_b}{\gamma_3} \right), \tag{5.2}$$

[1]For a uniform triple junction system the term $\gamma_b/\gamma_3 = 1$

where γ_3 is the energy of the straight grain boundary GB 3 and θ is a half of the contact angle at the tip of the triple junction. The velocity of the triple junction motion can be expressed as

$$V_{tj} = m_{tj}\gamma_b \left(2\cos\theta - \frac{\gamma_b}{\gamma_3}\right). \tag{5.3}$$

The velocity of the steady-state motion of the grain boundary system with a triple junction is given by Eq. (3.14). For the sake of convenience, it is repeated here

$$V_{gb} = 2\frac{\theta m_b \gamma_b}{a}. \tag{5.4}$$

In the case of steady-state motion of the entire boundary system the velocity of the triple junction V_{tj} is equal to the velocity of the grain boundaries V_{gb}. From Eqs. (5.3)-(5.4) we obtain

$$\frac{2\theta}{2\cos\theta - \frac{\gamma_b}{\gamma_3}} = \frac{m_{tj}a}{m_b} = \Lambda. \tag{5.5}$$

The dimesionless criterion Λ reflects the drag effect of the triple junction on the migration of the entire grain boundary system. Let us consider two limiting cases:

1. $\Lambda \longrightarrow 0$. In this case the angle $\theta \longrightarrow 0$ and the migration of the entire boundary system is controlled by the mobility of the triple junction and the correspondent driving force (Eq. (5.2). For the limit $\theta = 0$ the velocity of the system (Eq. (5.3) takes the form

$$V = m_{tj}\gamma_b \left(2 - \frac{\gamma_b}{\gamma_3}\right). \tag{5.6}$$

2. $\Lambda \longrightarrow \infty$. In this case the angle θ tends to its value at the thermodynamic equilibrium

$$\theta = \arccos\left(\frac{\gamma_3}{2\gamma_b}\right) = \theta_{eq}. \tag{5.7}$$

The motion of the system is governed by the grain boundary mobility and the corresponding driving force. In accordance to Eq. 5.4, the velocity of the boundary system can be written as

$$V = 2\frac{\theta_{eq} m_b \gamma_b}{a}. \tag{5.8}$$

These two regimes of grain growth kinetics can be distinguished experimentally measuring the contact angle 2θ for a known ratio γ_3/γ_b.

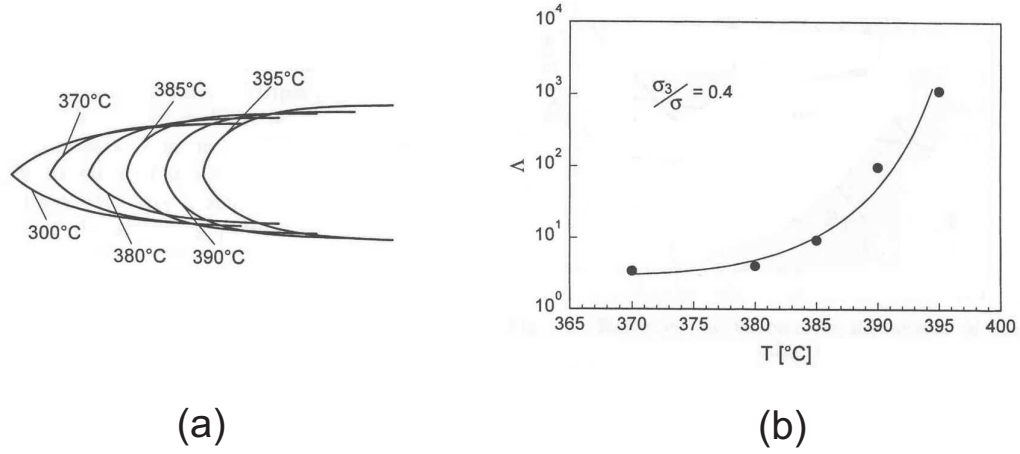

Figure 5.3: (a) Evolution of the shape of the grain boundary system with temperature, (b) temperature dependence of criterion Λ for $\gamma_3/\gamma_b = 0.4$ [30]

5.2 Previous studies

5.2.1 Migration of individual triple junctions

There are a few experimental works that studied the triple junction drag effect. For the first time the specific mobility of a triple junction was confirmed experimentally by Czubayko et al. [30]. These results were obtained in experiments on high pure (99.999 at. %) Zn-tricrystals. The motion of crystallographically different triple junctions was studied. The most pronounced triple junction drag effect on the grain boundary motion was observed for the triple junction formed by two curved high angle grain boundaries (61° and 62° $<01\bar{1}0>$) and the straight low angle grain boundary (3° <0001>) (Fig. 5.3).

The drag influence of triple junction was also studied in Al-tricrystals. The experiments revealed that the motion of grain boundary systems with triple junctions in Al can be controlled by slower moving triple junctions [31]. Triple junctions were formed by tilt grain boundaries with the <111> rotation axis and different angles of misorientation. The maximum drag effect was discovered for the triple junction formed by curved grain boundaries, 21° and 18° <111> accordingly, and low angle 3° <111> straight boundary. A drastic difference between the activation enthalpy of the grain boundary and

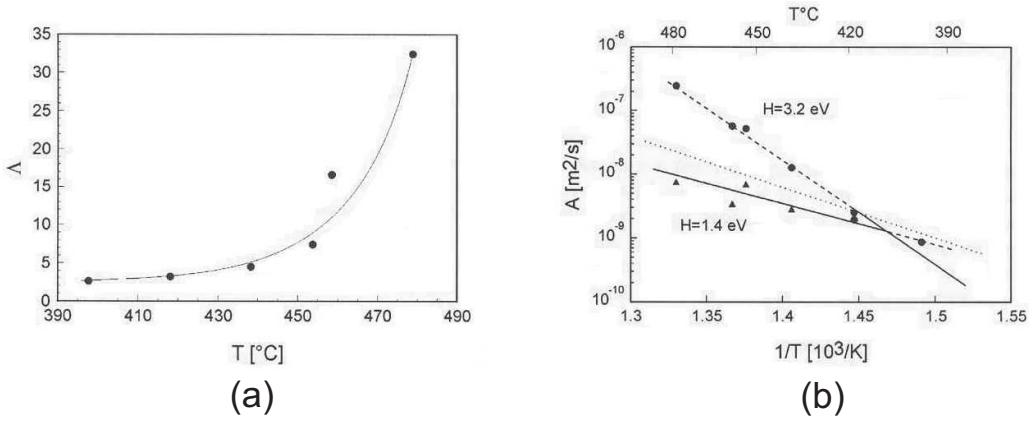

Figure 5.4: (a) Temperature dependence of criterion Λ for $\gamma_3/\gamma_b = 0.261$, (b) activation enthalpy for triple junction and grain boundary migration [31]

the triple junction was revealed in those experiments (Fig. 5.4).

Studies [30] and [31] showed that the drag effect of the triple junction depends on the temperature. It is particularly strong at low temperatures. In the high temperature regime the motion of the connected grain boundaries is less affected by the triple junction and, therefore, effectively controlled by the grain boundary mobility.

There is only one molecular dynamics study on triple junction migration [43]. The obtained results are in excellent qualitative agreement with experimental observations. The main conclusion of this study was that triple junction mobility is finite and can be sufficiently small to limit the rate of grain boundary migration. The triple junction drag on the grain boundary migration is especially important at small grain size, low temperature and near high symmetry misorientations. The discrepancy between the experimental and simulation studies is the condition under which the triple junction drag is significant. In the simulations, triple junction drag never hindered boundary migration at grain sizes above approximately 50 atomic spacing. On the other hand, experiments have demonstrated a triple junction drag for the grain size of about 100 μm. This difference was attributed to the presence of segregated impurities at grain boundaries in the experiments, while the simulations modeled migration in *absolutely* pure metals.

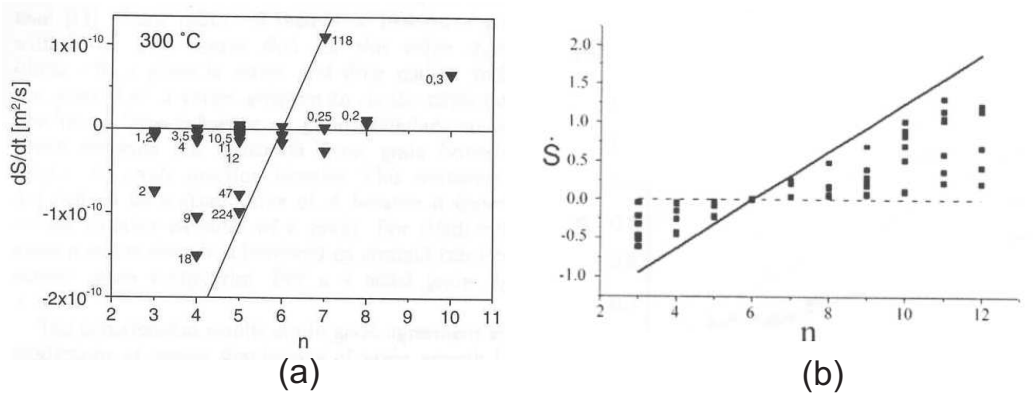

Figure 5.5: (a) Rate of grain area change dS/dt vs. topological class n of grains for 300° [46], (b) vertex simulation with junction drag ($0.1 < \Lambda < 10$) assuming $m_b \cong 10^{-4}\ m^4/J\ s$ and $\gamma_b \cong 0.3\ J/m^2$ [47]

5.2.2 Triple junction dragging and grain growth in 2D polycrystals

Triple junctions do affect the kinetics of grain growth which is most adequately describes in 2-dimensional space by the Von Neumann-Mullins equation [9, 44]

$$\frac{dS}{dt} = -\frac{A_b \pi}{3}(n-6)\,, \tag{5.9}$$

where S is the grain area, A_b is the reduced grain boundary mobility, n is the number of neighboring grains (topological class of grain). The following assumptions are made in this equation:

1. the triple junction do not drag the grain boundary migration,
2. all grain boundaries have equal mobilities and energies irrespective of their misortientation and plane inclination,
3. the grain boundary mobility is independent of its velocity.

The rate of grain area change is independent of the shape of boundaries and determined by the topological class n only. Grains with n >6 grow and those with n <6 dissappear, grains with n =6 are stable.

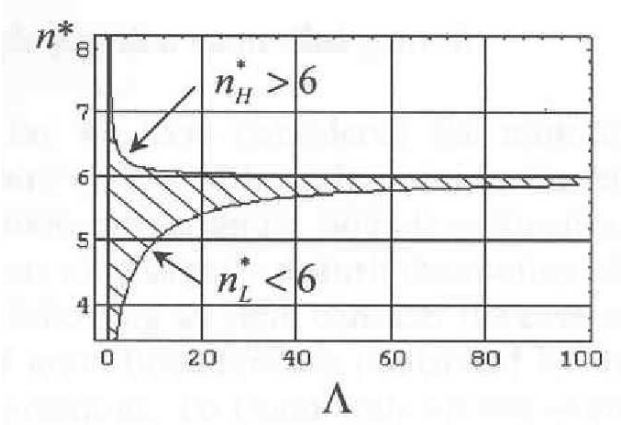

Figure 5.6: The limiting topological classes n_h^* and n_l^* vs. Λ

If triple junctions exert the drag on the adjoining grain boundaries owing their lower mobility, the Von Neumann-Mullins equation can be written [45] for n <6

$$\frac{dS}{dt} = \frac{A_b\left[2\pi - n\left(\pi - 2\theta\right)\right]}{1 + \frac{2\cos\theta - 1}{2\theta}} \tag{5.10}$$

and for n >6

$$\frac{dS}{dt} = \frac{A_b\left[n\left(\pi - 2\theta\right) - 2\pi\right]}{1 - \frac{1 - 2\cos\theta}{\ln(\sin\theta)}}. \tag{5.11}$$

Since θ is a function of Λ, the growth rate can also be expressed in terms of Λ. Let us consider the case $dS/dt = 0$ which occurs for n =6 in the Von Neumann-Mullins case. As obvious from Fig. 5.6, under the action of triple junction drag there is no unique n^* anymore and there are different branches n_h^* and n_l^* for n >6 and n <6, respectively. For small Λ there is a large gap between n_h^* and n_l^* and grains with $n_h^* < n^* < n_l^*$ should not change, since they can neither grow nor disappear.

The experimental study of the behavior of triple junctions in polycrystals in a quasi-two-dimensional system was first reported by Mattissen et al. [46]. The experiments revealed that due to triple junction drag there is no unique linear relationship between growth rate and the number of grain sides, n (Fig. 5.5a). The same results were also obtained by computer simulations using the 2D vertex model (Fig. 5.5b) [47].

Table 5.1: Concentration of main solute elements in used Al-alloys

Al-alloys	Al II	Al III	Al IV	Al V
Main Solute Element	Mg	Mg	Mg	Mg
Concentration, wt. ppm	0.2	50	100	1000

5.3 Experimental

The experiments were carried out on tricrystals produced from high pure Al (99.9999 wt. %, Al II, see Appendix A) with different contents of Mg atoms. The advantage of tricrystal experiments is that both interaction of the moving grain boundary with solute atoms and impact of solute atoms on the triple junction mobility can be studied simultaneously.

The Mg concentration was determined by glow discharged mass-spectroscopy (Tabl. A.1). As evident from Tabl. A.1 the total impurity concentration comprises a large number of elements. Since every element may interact differently with the grain boundary, it is important to understand, which element concentration is relevant for the overall migration behavior of the boundary. The problem is hard to address experimentally, since it is impossible to produce a "pure" binary alloy. However, alloys with different concentrations of one solute element and constant concentrations of other elements can be produced. Note that the concentration of this element exceeds the total amount of other impurity elements in the specimen, and below this solute element is referred to as the *main* solute element.

Thus, the concentration of the main solute element is the relevant concentration for grain boundary migration. For the sake of convenience, we characterize the used materials with regard to the concentration of the main solute element (Tabl. 5.1). In the first approximation we consider the concentration of Mg atoms in Al II alloy as the relevant concentration.[2]

All studied tricrystal specimens had the same crystallographic configuration and only the concentration of main solute element (Mg) varied. The

[2]It is to note, that in Al II alloy the concentration of Mg atoms (0.2 wt. ppm) is essentially smaller then the total impurity concentration (1 wt ppm). Strictly speaking, in this case the concentration of Mg cannot be considered as the relevant concentration for grain boundary migration

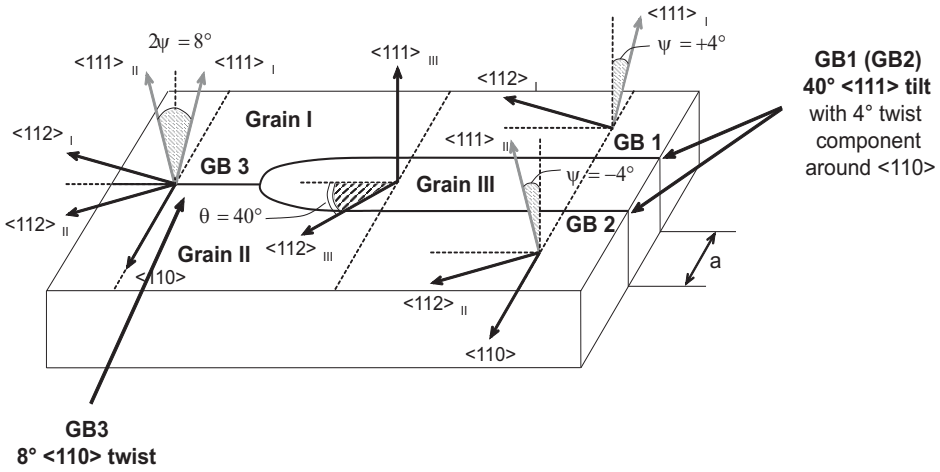

Figure 5.7: Geometry of grown tricrystals

utilized tricrystal configuration is shown in Fig. 5.7. Two curved grain boundaries GB 1 and GB 2 are identical in terms of their misorientation angles and rotation axes. A 40° <111> tilt boundary (GB 1, GB 2) is superimposed by a rotation around the axis perpendicular to the grain boundary plane by an angle $\psi = \pm 4°$. Thus, such a boundary can be described as a 40° <111> tilt boundary with a $\pm 4°$ twist component. GB 3 is a low angle twist grain boundary with a rotation axis <110> and a misorientation angle $2\psi = 8°$. The width of the shrinking grain, a, (Grain III) was about 900-1000 μm in all studied specimens.

The migration of connected grain boundaries has not been yet studied in such geometrical configuration. As mentioned in Chapter 4, the orientation contrast in the SEM is much better from the boundary which have an additional twist component than from the pure tilt one. Note that <111> boundaries with misorientation angles of about 40° are of special interest because of their dominant role in recrystallization of aluminum and its alloys.

The shape of grain boundaries and the location of the triple junction was recorded in-situ utilizing SEM set-up considered in Chapter 2. Fig. 5.8 shows the sequence of the recorded images for one of the studied tricrystal specimens. The orientations of the three adjacent grains were determined by the Laue-technique. The orientational characteristics of the studied tricrystals are given in Appendix B. For every temperature the velocity of the triple

junction, the angle 2θ, and the width of the vanishing grain were measured. The mobility of the grain boundary and of the triple junction was determined by Eqs. (5.4), (5.6). For convenience, we use reduced forms of grain boundary and triple junction mobilities

$$A_{gb} \equiv \frac{v \cdot a}{2\theta} = m_b \gamma_b = A_{gb0} \exp\left(-\frac{H_b}{kT}\right), \tag{5.12}$$

$$A_{tj} \equiv \frac{v \cdot a}{2\cos\theta - 2\cos\theta_{eq}} = m_{tj} \gamma_b a = A_{tj0} \exp\left(-\frac{H_{tj}}{kT}\right). \tag{5.13}$$

5.4 Effect of Mg atoms on grain boundary and triple junction mobility

The motion of grain boundaries with a triple junction was studied in the pure aluminum tricrystals (Al II) and in Al-tricrystals with the concentration of Mg atoms of 50 (Al III), 100 (Al IV) and 1000 (Al V) wt. ppm. For all specimens the velocity v and the angle 2θ were found to be constant at a given constant temperature during the entire studied temperature range. Evidently, the assumption of a steady-state motion of the entire grain boundary system was justified. Fig. 5.9 shows the temperature dependence of the grain boundary A_{gb} and triple junction A_{tj} reduced mobility and the contact angle 2θ in specimens with different concentrations of Mg atoms. The activation parameters (activation enthalpy H and pre-exponential mobility factor A_0 determined in accordance to Eqs. (5.12), (5.13) are summarized in Tabl. 5.2.

5.4.1 Effect of Mg atoms on grain boundary mobility

The temperature dependence of the grain boundary reduced mobility is shown in Fig. 5.10. One can see that Mg atoms have a pronounced effect on the grain boundary mobility. An increase in the Mg content from $0.2{\cdot}10^{-5}$ to 0.1 wt. % decreases the boundary mobility by more than one order of magnitude. The magnitude of the drag effect is practically independent of temperature (Fig. 5.11) in the studied range of Mg concentrations. When the Mg conventration rises the value of the activation enthalpy does not change up to 100 weight ppm of Mg and then decreases remarkedly (Fig. 5.12). The

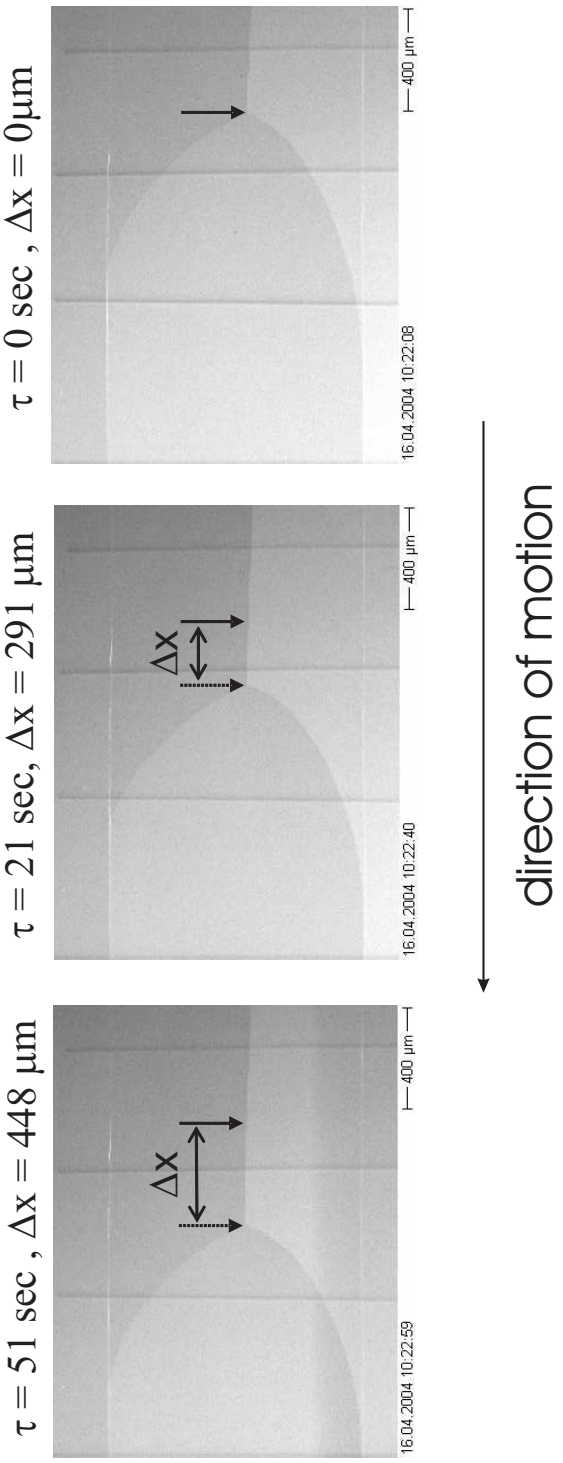

Figure 5.8: Sequence of recorded SEM images for the motion of grain boundary system with a triple junction in Al with 50 wt ppm of Mg (Al III)

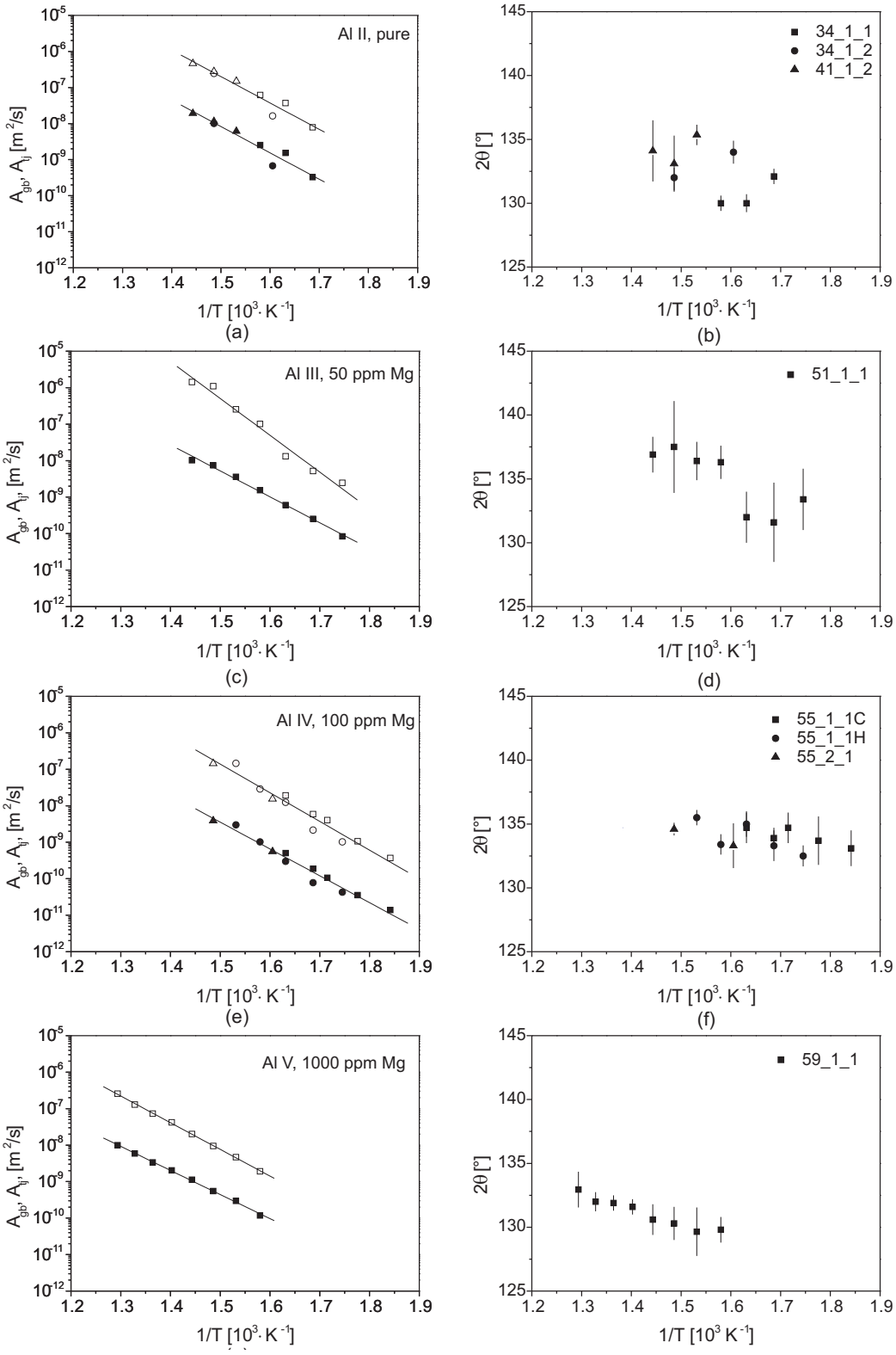

Figure 5.9: Temperature dependence of the reduced mobility A_{gb} (solid symbols), A_{tj} (open symbols) and of the contact angle 2θ in Al-specimens with different concentration of Mg atoms: (a)–(b) Al II, (c)–(d) Al III, (e)–(f) Al IV, (g)–(h) Al V. Different symbols correspond to different experiments

Table 5.2: The activation enthalpy and pre-exponential factor for grain boundary and triple junction migration

	H_{gb}, eV	A_{gb0}, m^2/s	H_{tj}, eV	A_{tj0}, m^2/s
Al II	1.45±0.16	$7.173 \cdot 10^2$ $^{+1.152 \cdot 10^4}_{-6.752 \cdot 10^2}$	1.60± 0.24	$1.098 \cdot 10^8$ $^{+1.096 \cdot 10^8}_{-9.182 \cdot 10^7}$
Al III	1.49±0.01	$8.938 \cdot 10^2$ $^{+2.269 \cdot 10^2}_{-1.809 \cdot 10^2}$	2.01± 0.14	$7.005 \cdot 10^8$ $^{+8.089 \cdot 10^9}_{-6.446 \cdot 10^8}$
Al IV	1.47±0.08	$3.867 \cdot 10^2$ $^{+3.348 \cdot 10^3}_{-3.005 \cdot 10^2}$	1.57± 0.11	$8.597 \cdot 10^4$ $^{+5.969 \cdot 10^5}_{-7.514 \cdot 10^4}$
Al V	1.32±0.02	$3.589 \cdot 10^0$ $^{+1.488 \cdot 10^0}_{-1.052 \cdot 10^0}$	1.46± 0.02	$7.324 \cdot 10^2$ $^{+2.211 \cdot 10^2}_{-1.702 \cdot 10^2}$

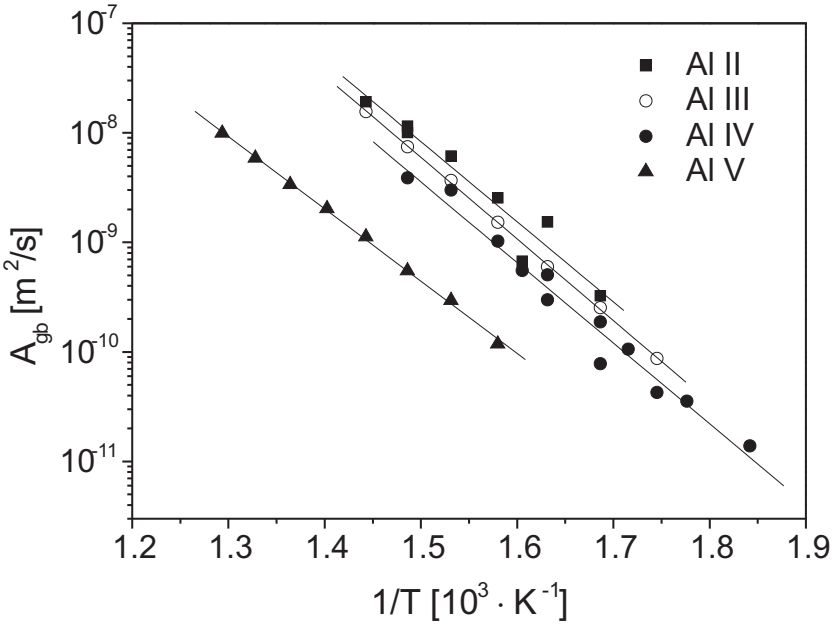

Figure 5.10: Temperature dependence of the reduced grain boundary mobility A_{gb} in Al-alloys with different concentration of Mg atoms.

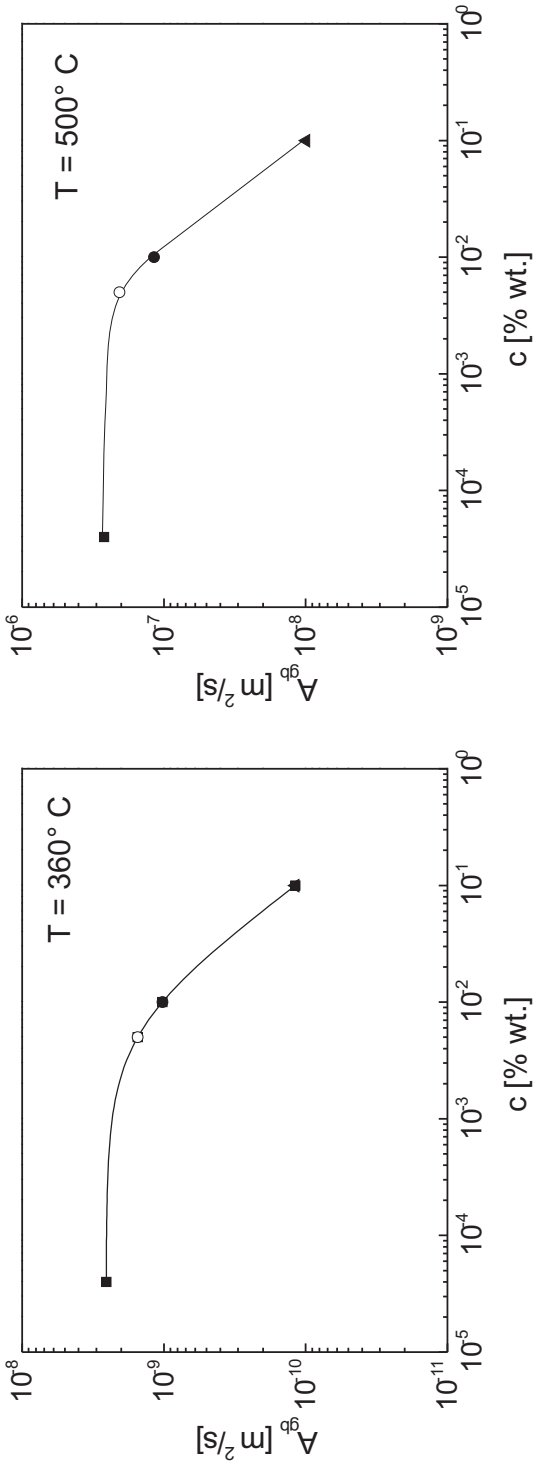

Figure 5.11: Reduced mobility *Agb* as a function of Mg concentration c in different Al-alloys: ■ – Al II; ○ – Al III; ● – Al IV; ▲ – Al V

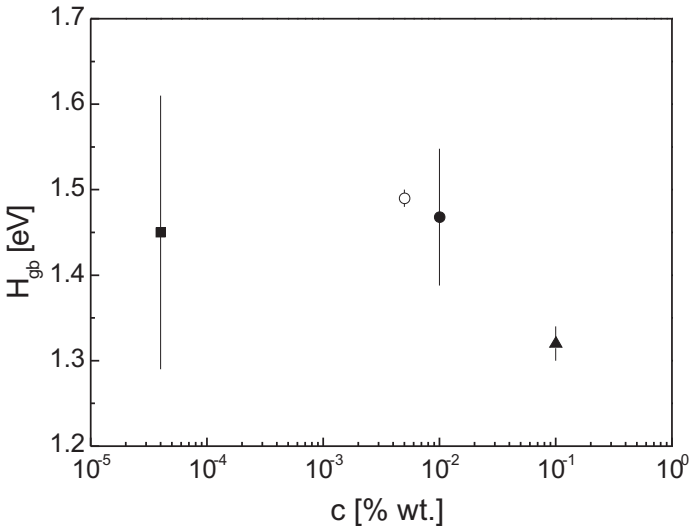

Figure 5.12: The dependence of activation enthalpy of grain boundary migration H_{gb} on concentration of Mg atoms c in different Al-alloys: ■ – Al II; ○ – Al III; ● – Al IV; ▲ – Al V

dependence of the pre-exponential factor on the Mg content was found to be similar to the activation enthalpy (Fig. 5.13).

The physical basis of grain boundary motion in solids with impurities was put forward by Lücke and Detert [29]. According to their theory the grain boundary moves together with the segregated impurities. Therefore, the velocity of the impurity atoms v_{im} should be equal to the boundary velocity v_b which moves under the action of the driving force p. The grain boundary imparts the same driving force to the impurities carried along

$$v_b = m_b p = v_{im} = m_{im} \frac{p}{\Gamma}, \tag{5.14}$$

where m_b and m_{im} are the mobility of the boundary and impurity atoms, respectively. $\Gamma = c^b - c_0$ is the adsoption at the boundary, i.e. the difference between the concentration of adsorbed impurities in the boundary and the bulk concentration c_0. With the Nernst-Einstein relation

$$m_{im} = \frac{D}{kT}, \tag{5.15}$$

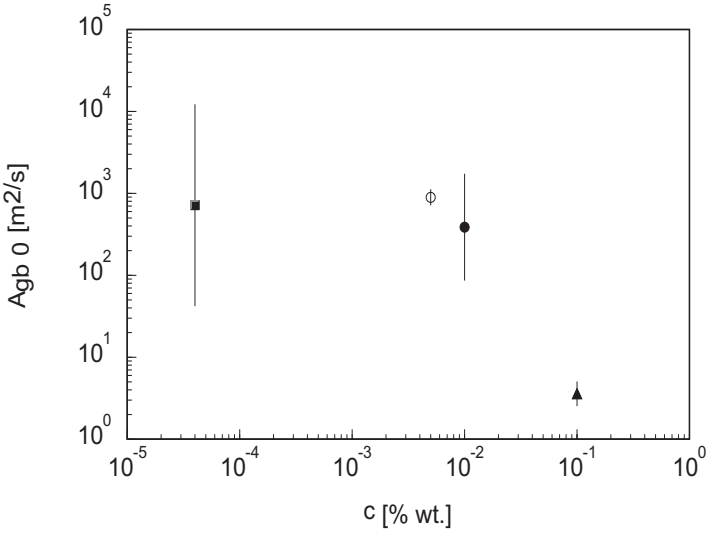

Figure 5.13: The dependence of grain boundary migration pre-exponential factor A_{gb0} on concentration of Mg atoms c in different Al-alloys: ■ – Al II; ○ – Al III; ● – Al IV; ▲ – Al V

where D is the respective diffusion coefficient, Eq. (5.14) yields

$$m_b = \frac{m_{im}}{\Gamma} = \frac{D}{\Gamma kT}. \tag{5.16}$$

For dilute (volume) solutions and for $c_b \gg c_0$ Lücke and Detert used the Henry isotherm

$$\Gamma = zBc_0 - c_0 = c_0 \left(zB_0 \exp \frac{H_i}{kT} - 1 \right) \cong zB_0 \exp \frac{H_i}{kT}, \tag{5.17}$$

where $B = \exp G_i/kT$, $B_0 = \exp(-S/k)$, G_i is the Gibbs free energy of adsorption, S_i is the adsoption entropy, H_i is the interaction entropy of impurity atoms with the boundary, z is the number of adsoption sites in the boundary. Eqs. (5.15)–(5.17) render the known expression for the mobility of the boundary with impurities

$$m_b = \frac{D_0 \exp\left(-\frac{H_d - H_i}{kT}\right)}{zB_0 kT} \cdot \frac{1}{c_0}, \tag{5.18}$$

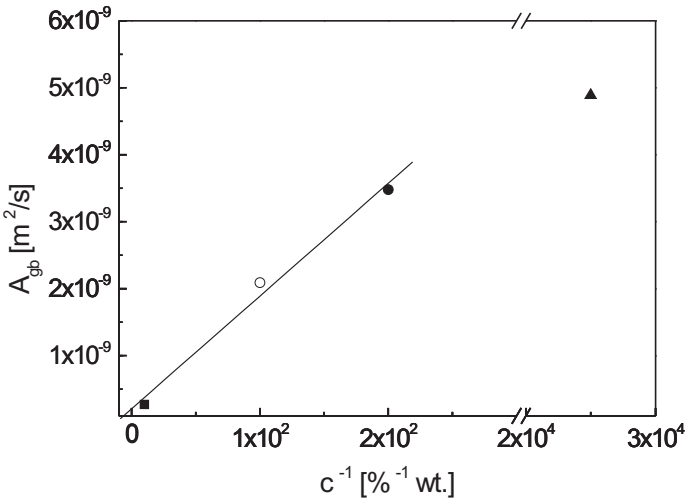

Figure 5.14: Reduced grain boundary mobility Agb vs. inverse concentration of Mg atoms c^{-1} in different Al-alloys: ■ – Al II; ○ – Al III; ● – Al IV; ▲ – Al V

where D_0 is the diffusion pre-exponential factor, H_d is the activation enthalpy of the volume diffusion of impurity atoms. According to this equation the activation enthalpy for the grain boundary migration is a sum of the two activations enthalpies, impurity diffusion and impurity adsoption. The pre-exponential mobility factor changes inversely propotionally to the impurity concentration.

One is tempted to make a conclusion that in studied Al-alloys the grain boundary motion is described by the Lücke and Detert theory, at least for low concentrations of Mg atoms (up to 100 weight ppm). Fig. 5.14 demonstrates the reduced grain boundary mobility as a function of inverse Mg concentration. As can be seen that in the concentration range between 0.2 and 100 wt. ppm of Mg the reduced grain boundary mobility increases linearly with inverse Mg concentration. Therefore, it can be concluded that the grain boundary motion in the range of Mg concentrations between 0.2 and 100 wt. ppm is determined by the impurity drag theory of Lücke and Detert. Note that at the current level of research it remains difficult to prove

it unambiguously due to the lack of mobility measurements in the considered concentration range. As evident from Figs. 5.12–5.14 the behavior of the grain boundary migration in Al V alloys (1000 wt. ppm of Mg) strongly deviates from that in Al-alloys with the lower Mg concentrations.

The obtained results (Figs. 5.12–5.14) allows to conclude that in the range of Mg concentration between 0.2 and 100 wt. ppm the grain boundary migration is controlled by the volume self-diffusion of Al atoms (H_d=1.47 eV, according to [48] and H_d=1.5 eV, according to [49]). With increase in the Mg concentration until 1000 wt. ppm in the bulk and, accordingly, the concentration of Mg atoms in the boundary, the grain boundary migration is started to be controlled by the volume diffusion of Mg atoms (H_d=1.35 eV, according to [50]).

5.4.2 Effect of Mg atoms on triple junction mobility

It is obvious from Figs. 5.8 and 5.15 that the contact angle 2θ increases with increasing temperature. In particular, for the Al III alloys the variations in the contact angle 2θ are largest (Fig. 5.15). The criterion Λ (Eqs. 5.5 and 5.7)[3] was found to be constant for a given temperature, but it increases with increasing temperature (Fig. 5.16). In all studied alloys, even at low temperatures Λ is not smaller then 10 (Al V) and it increases when the temperature rises up to 2 orders of magnitude. Therefore, at the temperatures, where Λ is small, the motion of boundaries is dragged to the certain extent by the slower triple junction. However, the minimum value of Λ=12 (Al V) is not small enough and the motion of the entire boundary system is still controlled by the grain boundary kinetics. It might be assumed that with increase in the temperature the triple junction becomes more mobile than the grain boundaries as indicated by increasing Λ. Therefore the drag of the triple junctions decreases at high temperatures. Close to the melting point, the motion of the entire boundary system is governed by the grain boundary mobility only. It has been already shown that the temperature dependence of the contact angle cannot be explained in terms of different temperature coefficients of the grain boundary energies [9].

[3]The ratio γ_3/γ_b was determined under an assumption that for temperatures near the melting point the value of the contact angle reaches its thermodynamic equilibrium value. $2\theta_{eq}$ was measured at the temperature of 630° ± 2°C for the "notched" Al III specimens (Figs. 6.8, 6.9) and was found to be equal to 138.5°±0.3° (Fig 15.14)

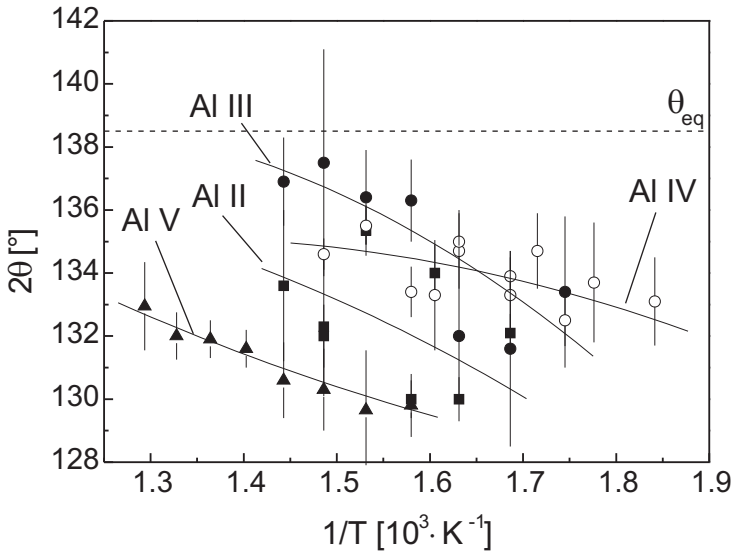

Figure 5.15: Contact angle 2θ vs. temperature in different Al-alloys: ■ – Al II; ○ – Al III; ● – Al IV; ▲ – Al V

Fig. 5.17 shows the dependence of Λ on the Mg concentration at 360°C and 400°C. The obtained results allow concluding that the magnitude of Λ is affected by Mg content. One can see, that excluding pure Al II alloys[4], Λ decreases with increasing Mg concentration. That means, that the "dragging" influence of triple junctions is more pronounced in Al-alloys with the higher Mg concentration. Such tendency can be explained on terms of the impact of Mg atoms on the triple junction m_{tj} and grain boundary m_{gb} mobilities. According to Eq. (5.5), the parameter Λ is a function of the triple junction m_{tj} and grain boundary m_{gb} mobilities. If the triple junction mobility m_{tj} decreases faster with Mg concentration than the grain boundary mobility m_{gb}, this is reflected by the parameter Λ. This tendency is particularly evident in Fig. 5.18, which shows that the triple junction mobility drops faster than the grain boundary mobility with increasing the amount of Mg. Such behavior can be explaned by different interaction of Mg atoms with the triple junction and grain boundary struture.

[4]As was mentioned, impurity-boundary interaction in Al II is not only determined by Mg atoms and may have a complex multicomponent character

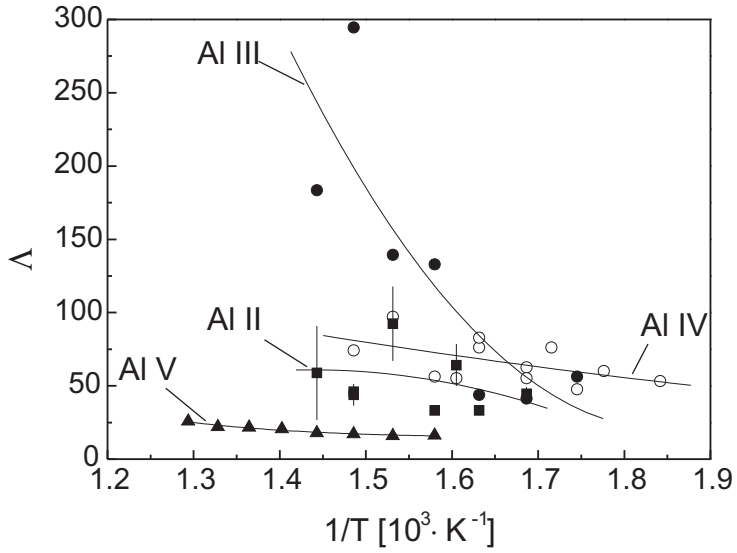

Figure 5.16: Parameter Λ vs. temperature in different Al-alloys: ■ – Al II; ○ – Al III; ● – Al IV; ▲ – Al V

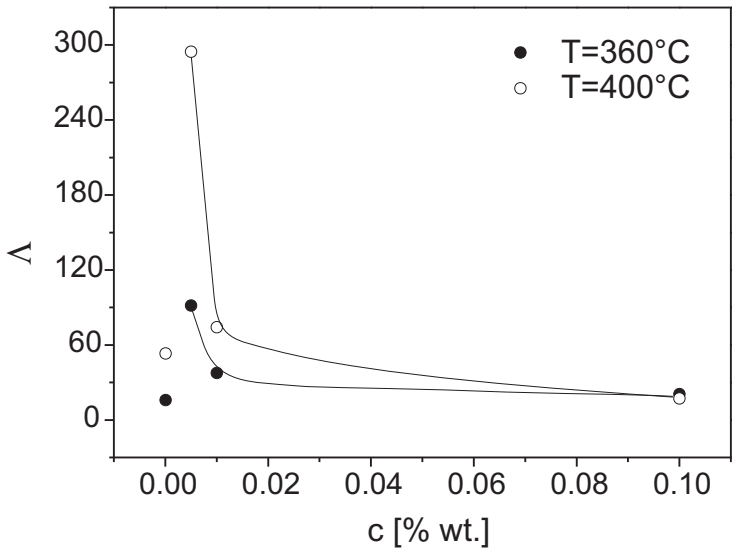

Figure 5.17: Parameter Λ vs. concentration of Mg at constant temperature of 360 and 400°C

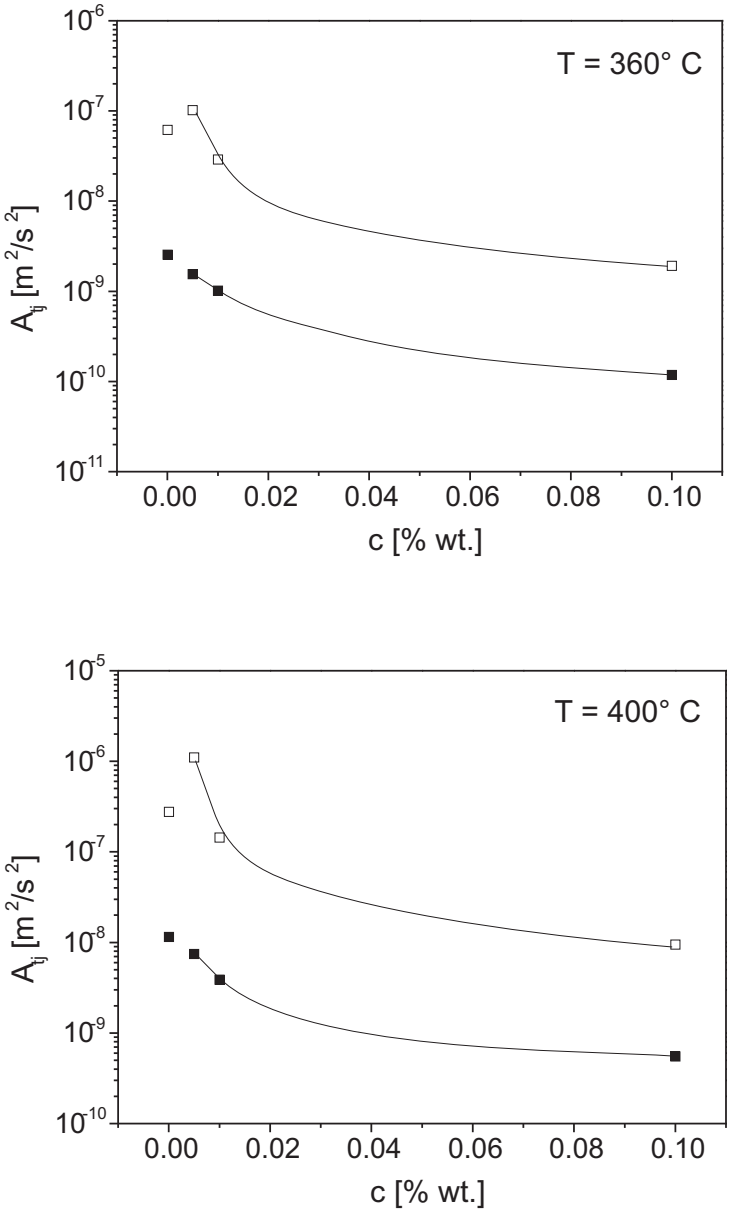

Figure 5.18: Reduced mobility A_{gb} (solid simbols) and A_{tj} (open symbols) as a function of Mg concentration c at constant temperature of 360 and 400°C

5.5 Summary

The temperature dependence of the migration of a symmetrical triple junction with two 40° <111> grain boundaries with a ±4° twist component was investigated in Al-tricrystals with different concentrations of Mg atoms in the temperature range between 270°C and 500°C. The effect of Mg atoms on the grain boundary and triple junction mobilities was studied.

The activation parameters for grain boundary and triple junction migration, the activation enthalpy (H_{gb}, H_{tj}) and the pre-exponential factor (A_{gb0}, A_{tj0}), were found to be affected by the solute Mg atoms. In the concentration range between 0.2 and 100 wt. ppm of Mg the reduced grain boundary mobility A_{gb} increases linearly with inverse Mg concentration and it has a reasonable agreement with the impurity drag theory of Lücke and Detert. For the higher Mg content (1000 wt. ppm) the dependence of the grain boundary mobility on the Mg concentration cannot be described by this theory.

In the whole studied temperature range the motion of grain boundaries with triple junctions is governed by the grain boundary kinetics. It has been shown that the criterion Λ depends on the Mg concentration. It drastically decreases with increasing Mg amount and therefore the "dragging" influence of the triple junctions on the motion of the entire system increases. Such tendency can be explained in terms of different interaction of Mg atoms with the triple junction and grain boundary structure.

Chapter 6

Measurement of excess free volume of grain boundaries

6.1 Introduction and previous studies

The grain boundary excess free volume is a fundamental property of grain boundaries. Follow to the destruction of the perfect crystal stacking due to the introduction of a grain boundary into a stack of lattice planes, the crystal has to expand locally at the interface to accommodate the structural mismatch (Fig. 6.1). This "expansion" at the grain boundary is referred to as the grain boundary excess free volume (BFV).[1] The BFV strongly correlates with the properties of grain boundaries such as diffusion, sliding [51], wetting [52] etc. It is also releated to mechanisms of grain boundary migration which in turn determine the microstructure evolution during recrystallization and grain growth. The knowledge of the BFV is especially important for fine grained and nanocrystalline polycrystals where it is instrumental to control the microstructure and properties. The value of the excess free volume dictates the driving force that tries to "squeeze" grain boundaries out of a polycrystal under the loading. In other words, the BFV determines to a large extent the stability of a grain structure in polycrystals under high stresses. Below we review the previous works where the BFV was studied. We consider its relation with the properties of grain boundaries: energy, diffusion, mobility etc.

Not much studies on the grain boundary excess free volume have been

[1] Sometimes the BFV is also referred to as the boundary volume expansion

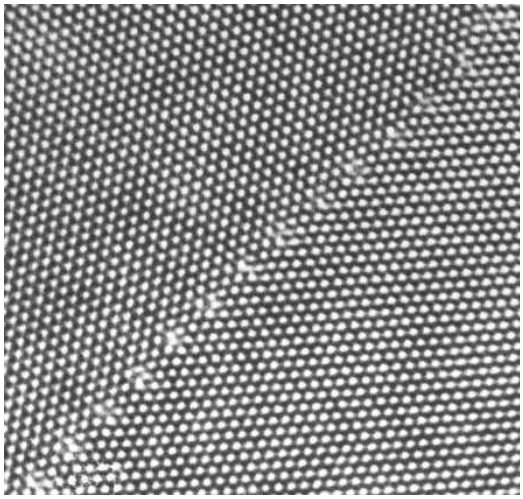

Figure 6.1: Σ19 grain boundary in Al

done. We start our review from the works where grain boundaries were studied in hard-spheres (in two-dimensional space – hard-disks) model. In hard-spheres model the atoms are represented as a collection of hard, perfectly elastic, balls. It is a simple and very powerful model. This model has a long history of the useful applications in materials science. More than two thousand years ago Greek philosopher Democritus claimed that the world is made of hard atoms that would never break [53]. Through-out the history of materials science, this model was successfully utilized describing the efficiency of packing, i.e. the arrangement of hard spheres that they occupy a minimum volume. This peculiarity of the model provides the ability for the analysis of the interface structure; in particular, the difference between the packing densities of the interface and the bulk, i.e. the excess free volume of interfaces, can be determined by this model.

A qualitative analysis of the BFV and its correlation with various properties of grain boundaries has been done by Knizhnik. In [54] the structure of tilt grain boundaries in two-dimensional hard-disks FCC crystals was analyzed (Fig. 6.2a). The BFV was calculated as the difference between the volume of the bicrystal and the volume of the ideal single crystal containing the same amount of atoms (hard-disks) per unit area of the grain boundary. Fig. 6.2b shows the grain boundary excess free volume V^{ex} as a function of the angle of misorientation φ for <100> symmetrical tilt boundaries. Similar

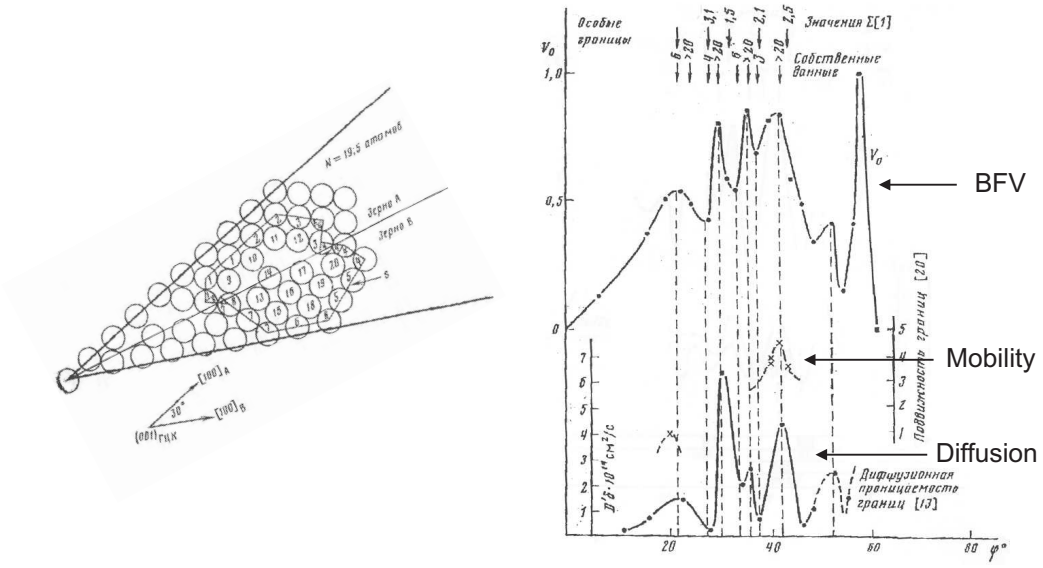

Figure 6.2: (a) Symmetrical tilt grain boundary with rotation axis <100> and misorientation angle $\varphi = 30°$ in hard-disks FCC crystal. (b) Excess free volume (V_0), diffusion and mobility of <100> tilt GB in FCC metal vs. misorientation angle φ

to the grain boundary mobility [18] the BFV changes non-monotonically with increasing the angle of misorientation and assumes deep cusps at low Σ CSL boundaries. The comparison between the misorientation dependence of the calculated BFV V^{ex} and the misorientation dependence of grain boundary diffusion δD_b (Fig. 6.2b) demonstrates qualitatively similar behavior: grain boundaries with the smaller BFV exhibit the lower diffusivity, the larger BFV dictates the higher diffusivity of the boundaries.

Comprehensive investigations on structure-property correlations of grain boundaries in Au and Cu were accomplished by Wolf [55, 56, 57]. These studies were performed by atomistic calculations using many-body embedded-atom-method (EAM) potential for gold and the Lennard-Jones (LJ) pair potential for copper. As a result, these studies revealed that the BFV is proportional to the boundary energy and to the number of broken bonds per unit of boundary area. Fig. 6.3 shows the obtained results. Over 250 grain boundaries were studied. It is worth emphasizing that character of the grain boundaries studied in [55, 56, 57] varied, i.e. tilt, twist and mixed boundaries

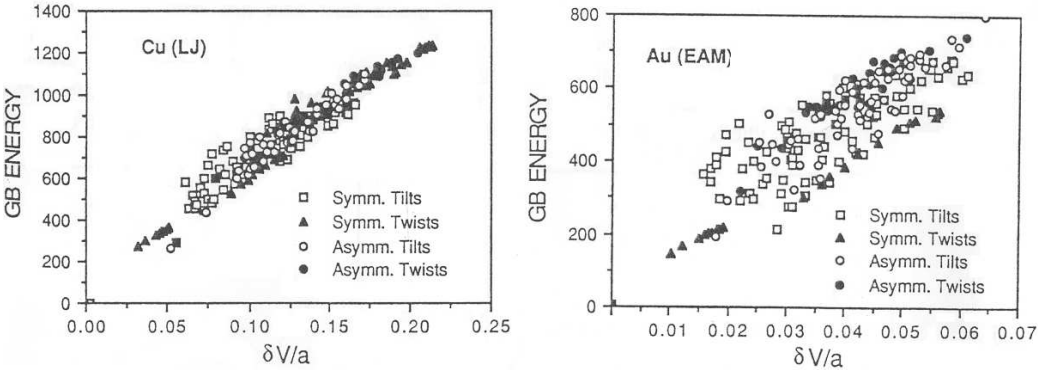

(a) (b)

Figure 6.3: Grain boundary energy vs. grain boundary free volume for Cu (a) and Au (b)

with different rotation axes <hkl> and misorientation angles θ were investigated. The relationship between the BFV V^{ex} and the energy of boundary γ_b was elucidated and the linear dependence

$$\gamma_b\left(V^{ex}\right) = \alpha + \beta V^{ex} \tag{6.1}$$

was discovered, where α and β are fitting coefficients and V^{ex} is the BFV. Note that for the first time linear dependence between the BFV and the energy of boundary was reported by Frost at al. for <100> tilt boundaries in hard-spheres FCC crystals [58] .

Stremel et al. analyzed the structure of <111>, <110>, <100> and <210> grain boundaries [59, 60]. In those works the magnitude of the BFV was calculated using geometrical distribution of the broken bond density at the boundary plane for Al and Fe(γ).

A correlation between the grain boundary mobility and the BFV was recently examined by Srolovitz et al. [63]. In particular, the migration of $\Sigma 5$ <100> tilt grain boundaries with different inclinations was studied in FCC metal. Simulations were performed using EAM potential for Ni. Both the excess free volume and mobility showed qualitatively similar non-monotonic behavior with respect to the boundary inclination. The BFV (and mobility) assumed minima for the inclinations where the boundary plane has low indexes (relative to at least one of the two crystals).

Let us refer to a few experimental studies where the problem of the excess free volume was addressed. Meiser et al. [64] estimated the excess free

Table 6.1: Grain boundary excess free volume (previous studies)

	Method	Metal	V^{ex} $[m^3/m^2]$
Frost et al. [58][2]	hard-spheres model	FCC	$0.1 \div 0.5$
Knizhnik [54][3]	hard-disks model	FCC	$0 \div 1$
Wolf [55, 56, 57]	molecular statics	Cu(LJ) Au(EAM)	$9 \cdot 10^{-12} \div 8 \cdot 10^{-11}$ $5 \cdot 10^{-12} \div 3 \cdot 10^{-11}$
Merkle et al. [61, 62][4]	HRTEM	Au(Σ11)	$2.8 \cdot 10^{-12} \div 3.3 \cdot 10^{-12}$
Meiser et al. [64][4]	disappearing of energy peaks	Sb	$1 \cdot 10^{-10} \div 1 \cdot 10^{-12}$
Stremel et al. [59, 60]	broken bond density	Al Fe(γ)	$5 \cdot 10^{-11} \div 1 \cdot 10^{-10}$ $5 \cdot 10^{-11} \div 1 \cdot 10^{-10}$
Srolovitz et al. [63]	molecular dynamics	Ni(EAM) (Σ5)	$3.9 \cdot 10^{-11} \div 4.2 \cdot 10^{-11}$

volume of grain boundaries in silver measuring the position of the peaks on the energy-misorientation angle diagram at ambient and a high gas pressure of $7 \cdot 10^8$ Pa. In those experiments Sb single crystal spheres (diameter 60 ± 10 μm) were sintered onto a surface of a <110> Sb single crystal plate by annealing at 950° in inert gas atmosphere at pressure of $1 \cdot 10^5$ and $7 \cdot 10^8$ Pa. The high-temperature annealing exerts rotations of the spheres and in turn decreasing the energy of the grain boundaries between the plate and the spheres. The orientation distribution of the spheres was measured after annealing. The observed disappearing of some orientation peaks (and thus, energy peaks) with increasing the pressure was interpreted in terms of phase transformation and the larger value of the BFV for some low energy grain boundaries. The BFV was estimated for the grain boundaries with

[2]Dimensionless value. The difference between the areas of a bicrystal and that of a perfect single crystal containing the same number of hard-disks, normalized per unit length of the grain boundary

[3]Dimensionless value. The difference between the volumes of a bicrystal and that of a perfect single crystal contained the same number of hard-spheres normalized per atomic volume

[4]Experimental

misorientations corresponding to the vanished peaks.

The boundary excess free volume was also measured by Merkle et al. in HRTEM studies [61, 62]. The lattice "fringe" shifts across the interface were measured. As a result, such measurements give a highly precise value of the BFV.

The considered above results are summarized in Tabl. 6.1. Usually the magnitude of the BFV is normalized per boundary area and, thus, is given in m^3/m^2. The value of the BFV averaged over all different types of grain boundaries previously investigated is in range of $10^{-11} \div 10^{-10}\ m^3/m^2$.

6.2 Thermodynamic method to measure excess free volume of grain boundaries

In the present work the thermodynamic method for the experimental determination of the BFV is proposed. The details of this method are discussed below.

6.2.1 Brief introduction into thermodynamics of interfaces

Let us consider a bicrystal consisting of two homogeneous bulk phases α and β, which are in contact along a planar interface (Fig. 6.4). The entire system is maintained in equilibrium at constant temperature T, hydrostatic pressure p and chemical potential μ_i of each of the components. Combining the first and the second low of thermodynamics we can write increase in the internal energy in a system with an interface in the form

$$dE = TdS - pdV + \sum_{i=1}^{k} \mu_i dN_i + \gamma d\widetilde{A}, \tag{6.2}$$

where S is the entropy, V is the volume, N_i is the number of atoms of component i, k is the number of components, $\widetilde{A}$ is the area of the interface and γ is the excess free energy per unit area of the interface. Eq. (6.2) contains the bulk terms and additional term γdA which is required to account increase in the internal energy associated with increase of the area of the interface. The basic thermodynamic variables: the Gibbs free energy G, the Helmgoltz

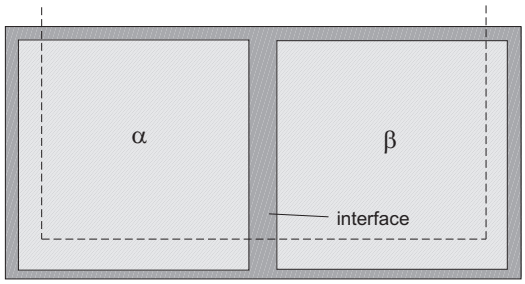

Figure 6.4: Bicrystal consisting of α and β bulk phases and interface

free energy F and the Gibbs grand potential Ω are defined by

$$G = E + pV - TS = \sum_{i=1}^{k} \mu_i dN_i, \tag{6.3}$$

$$F = E - TS, \tag{6.4}$$

$$\Omega = E - TS - \sum_{i=1}^{k} \mu_i dN_i = -pV. \tag{6.5}$$

Combining each of these equations with Eq. (6.2), this yields

$$dG = -SdT + Vdp + \sum_{i=1}^{k} \mu_i dN_i + \gamma d\widetilde{A}, \tag{6.6}$$

$$dF = -SdT - pdV - \sum_{i=1}^{k} \mu_i dN_i + \gamma d\widetilde{A}, \tag{6.7}$$

$$d\Omega = -SdT - pdV - \sum_{i=1}^{k} N_i d\mu_i + \gamma d\widetilde{A}. \tag{6.8}$$

From Eqs. (6.2) and (6.6)–(6.8) in accordance with a theorem of small variations of the thermodynamic potential γ corresponds to

$$\gamma = \left(\frac{\delta E}{\delta \widetilde{A}}\right)_{S,V,N_i}, \tag{6.9}$$

$$\gamma = \left(\frac{\delta G}{\delta \widetilde{A}}\right)_{T,p,N_i}, \tag{6.10}$$

$$\gamma = \left(\frac{\delta F}{\delta \widetilde{A}}\right)_{T,V,N_i}, \tag{6.11}$$

$$\gamma = \left(\frac{\delta \Omega}{\delta \widetilde{A}}\right)_{T,V,\mu_i}. \tag{6.12}$$

Eqs. (6.9)–(6.12) show that any type of energy change (δE, δG, δF, $\delta \Omega$) per change in the interface area ($\delta \widetilde{A}$) can be used to represent γ. In a certain case the applicable equation is defined under constraints which are present in the system. For instance, the Gibbs free energy notation is convenient for a one-component system at constant T and p.

6.2.2 Gibbs thermodynamics applied to grain boundaries

The thermodynamics of interfaces was first developed more than 100 years ago by Gibbs. He defined the extensive thermodynamic properties of interfaces, such as the internal energy, entropy etc., as excess quantities associated with the presence of the interface in the system.[5] The interface properties were determined by the Gibbs method as the difference between a real system, in which the interface (surface) is the certain dividing layer between two phases, and an ideal system, in which the phases are homogeneous up to the their contact. According to Gibbs the "dividing surface" is the transition layer between two homogeneous phases α and β, the thickness of which is much smaller than the other dimensions of the system.

If M is a certain extensive characteristics of the system (energy, entropy, volume etc), then its surface excess M^s can be defined as an excess (difference) between the total value of M and its bulk part:

$$M^s = M - \left(M^\alpha + M^\beta\right), \tag{6.13}$$

where M^α and M^β are the constituents of M in α and β phases, accordingly.

Let us define the bulk densities m^α and m^β of the quantity M in the volumes V^α and V^β divided by the interface, then

$$M^s = M - \left(m^\alpha V^\alpha + m^\beta V^\beta\right). \tag{6.14}$$

[5] Sometimes the Gibbs method is called as a "method of excesses"

Note that this definition is not complete since it does not define the location of the transition surface layer. In other words, it contains no information how the volumes V^α and V^β were determined. The idea of the method of surface excesses is that the quantities V^α and V^β can be determined in a variety of ways (of course, the condition $V^\alpha + V^\beta + V^s = const$ must be satisfied). For the equilibrium system with a flat interface, Eq. (6.14) has the properties of linearity $(M_1 + M_2)^s = M_1^s + M_2^s$, its application to the main thermodynamic equations considered above gives the *same relationship* between the excess surface quantities *irrespective* of the position of the dividing surface, though the excess surface values do depend on the choose of the interface position.

Gibbs divided the quantities into surface and bulk part in the following way. He assumed the the excess surface volume to be zero ($V^s = 0$) and $V^\alpha + V^\beta = V$, where V is the total volume of the system. In geometrical term it means that the transition surface layer is replaced by the 2-dimensional dividing surface. Eq. (6.14) can be rewritten as

$$M = m^\alpha V^\alpha + m^\beta V^\beta + m^s \widetilde{A}, \tag{6.15}$$

where m^s is the surface excess density (excess per unit area), $\widetilde{A}$ is the area of the surface and $M^s = m^s \widetilde{A}$ is the the surface excess of the property.

In such a manner the surface excess and the density of surface excess of various thermodynamic parameters can be introduced. The surface excess of the material in the equilibrium system is referred to by a special term, the adsorption Γ. Thus, in this term, the number of atoms N_i of the i-th component in the equilibrium is given by

$$N_i = n_i^\alpha V^\alpha + n_i^\beta V^\beta + \Gamma_i \widetilde{A}, \tag{6.16}$$

where n_i is the atomic density of the i-th component, Γ_i is the adsorption of the i-th component at the surface.

Now let us return to Eq. (6.8) for the Gibbs grand potential. For the surface parameters it reads

$$d\Omega^s = -S^s dT - V^s dp - \sum_{i=1}^{k} N_i d\mu_i^s + \gamma d\widetilde{A}. \tag{6.17}$$

On the other hand, by differentiating of Eq. (6.5) for the system with the interface we obtain :

$$d\Omega^s = d\left(-pV^s + \gamma\widetilde{A}\right) = -pdV^s - Vdp^s + \gamma d\widetilde{A} + \widetilde{A}d\gamma. \tag{6.18}$$

Subtracting Eqs. (6.17) and (6.18) we obtain the equation which connects the variations in the excess free energy of the interface with the variations in temperature, pressure and chemical potentials of the bulk phases:

$$\widetilde{A}d\gamma = -S^s dT - \sum_{i=1}^{k} N_i^s d\mu_i + V^s dp. \tag{6.19}$$

For the specific values $s^s = S^S/\widetilde{A}$, $\Gamma_i = N_i^s/\widetilde{A}$, $v^s = V^s/\widetilde{A}$ Eq. (6.18) is substituted by

$$d\gamma = -s^s dT - \sum_{i=1}^{k} \Gamma_i^s d\mu_i + v^s dp. \tag{6.20}$$

Eq. (6.19) is well known Gibbs equation, which is usually applicable to adsorption at interfaces and adsorption at grain bundaries.

In the Gibbs method, in a local sense, $V^s = 0$ and Eq. (6.19) assumes the form

$$d\gamma = -s^s dT - \sum_{i=1}^{k} \Gamma_i d\mu_i. \tag{6.21}$$

For the grain boundary adsorption in the one-component system the term $\sum_{i=1}^{k} \Gamma_i d\mu_i$ is substituted by $\Gamma_0 d\mu$. The parameter Γ_0 has a meaning of the autoadsorption at grain boundaries in pure materials. The autoadsorption is referred to as the difference in the atomic densities between the boundary and the bulk per boundary area. Let us consider an ideal single crystal of the volume V which contains N_a atoms (Fig. 6.5a). We introduce a grain boundary (thin layer with the lower atomic density than in the bulk) to the crystal that the volume of the crystal V remains constant and only the number of atoms changes (Fig. 6.5b). To satisfy the requirement $V = constant$ the grain boundary has to cut a part of the crystal body with the higher atomic density and, thus, the total number of atoms in such bicrystal decreases ($N_a^* < N_a$). For the autoadsorption we get

$$\Gamma_0 = \frac{N_a^* - N_a}{\widetilde{A}} \left[\frac{mol}{m^2}\right], \tag{6.22}$$

where $\widetilde{A}$ is the grain boundary area. It is seen that the autoadsorption is negative, $\Gamma_0 < 0$, by definition. Eq. (6.20) acquires the form

$$d\gamma_b = -s^s dT - \Gamma d\mu. \tag{6.23}$$

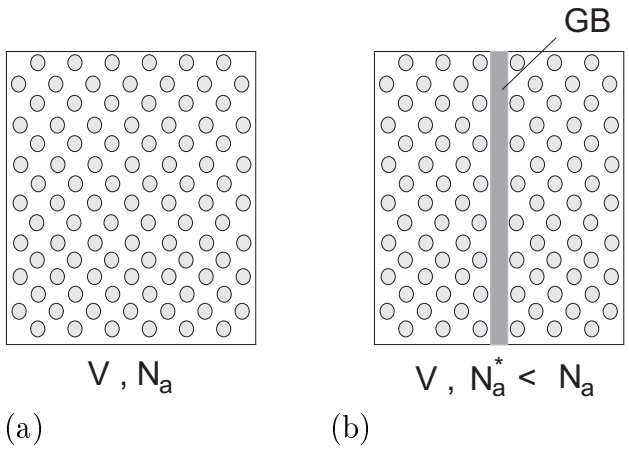

Figure 6.5: (a) Ideal single crystal of the volume V with N_a atoms. (b) Bicrystal of the same volume V with $N_a^* < N_a$ atoms.

Expressing μ through the thermodynamic characteristics of the bulk:

$$d\mu = \Omega_a dp - s_a^v dT, \tag{6.24}$$

where s_a^v is the antropy of the atom in the bulk, Ω_a is the atomic volume. Taking into account that $s^s = \Gamma_0 s_s^v$, where s_s^a is the surface excess of the entropy per atom at the surface (boundary) we obtain

$$d\gamma_b = -\Gamma_0 \left(s_s^a - s_v^v\right) dT - \Gamma_0 \Omega_a dp. \tag{6.25}$$

The variation in the excess free energy of the boundary (grain boundary energy) with increase in the hydrostatic pressure and temperature may be obtained by differentiating of Eq. (6.25)

$$\left(\frac{\partial \gamma_b}{\partial p}\right)_T = -\Gamma_0 \Omega_a, \tag{6.26}$$

$$\left(\frac{\partial \gamma_b}{\partial T}\right)_p = -\Gamma_0 \left(s_a^s - s_a^v\right) = -\frac{q}{T}, \tag{6.27}$$

where q is the specific heat of grain boundary formation and $-q/T$ is the specific surface excess of entropy. One can see that in principle it is possible to determine the autoadsorption and the surface excess of entropy by measuring the energy.

In modern theories of grain boundary structure the autoadsorption is closely related to the concept of the grain boundary excess free volume. The autoadsorption determines how much the material density of the boundary differs from the material density of the bulk.

6.2.3 Triple junction method to measure excess free volume of grain boundaries

Direct measurements of the grain boundary adsorption and, thus, the BFV are impossible. The only way to determine the excess free volume of grain boundary is to measure a grain boundary property, for instance, the grain boundary energy, which reflects the BFV. The term $(-\Gamma_0\Omega_a)$ in the right part of Eq. (6.26) is the excess free volume of the grain boundary. If it is possible to measure increase in the grain boundary energy with increasing the external pressure (left term in Eq. (6.26)) at T held constant and in the system maintained closed, then the excess free volume of the boundary can be determined. There are a few experimental methods to measure the grain boundary energy. In the present work we discuss only the triple junction method and do not discuss other ones, since in the majority of them the pressure dependence of grain boundary energy cannot be studied anyhow.[6]

The scheme of this method is shown in Fig. 6.6a. If the mechanical equilibrium[7] is established at the triple junction and grain boundary energies do not depend on boundary inclination, the correlation between the energies of the grain boundaries is given by

$$\frac{\gamma_{b_1}}{\sin\alpha_1} = \frac{\gamma_{b_2}}{\sin\alpha_2} = \frac{\gamma_{b_3}}{\sin\alpha_3}, \tag{6.28}$$

where γ_{b_1}, γ_{b_2}, γ_{b_3} are the energies of the grain boundaries and α_1, α_2, α_3 are the angles between the grain boundaries. For random grain boundaries and for grain boundaries which are far from special misorientations, the inclination dependence of grain boundary energy is known to be small and therefore can be neglected.

[6] The detailed review of experimental methods to measure the grain boundary energy is given by Gottstein and Shvindlerman in [9]

[7] The triple junction is in the mechanical equilibrium when a sum of the driving forces acting on it, is added to zero and the grain boundaries form a stable (unmovable) configuration at given conditions (T and p)

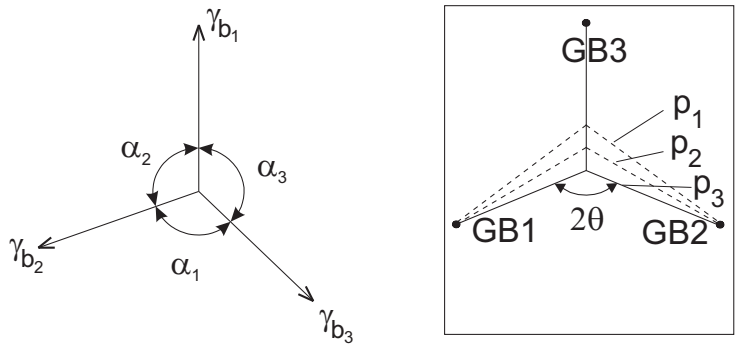

(a) (b)

Figure 6.6: (a) Equilibrium angles at triple junction. (b) Sequential junction position during measurement of pressure dependence of boundary energy $p_1 < p_2 < p_3$

The triple junction method is best realized in specially grown tricrystals, where the triple junction is formed by two high-angle grain boundaries GB1 and GB2 which have the same misorientation and, thus, equal energies $\gamma_1 = \gamma_2 = \gamma_b$. The third boundary GB3 has the energy γ_3 which is *a priori* known. The grains are homogeneous through the thickness of the tricrystal. That means the triple junction is rectilinear and perpendicular to the plane of diagram. Far from the triple junction all three grain boundaries are planar, their planes are perpendicular to the plane of the diagram. This leads to a quasi-two-dimensional problem.

Fig. 6.6b shows the idea of the experiment. Let us imaging that the boundaries are "nailed" and the triple junction is unmovable due to any reason at given temperature T and hydrostatic pressure p [8] (for instance, due to absence of the curvature of grain boundaries and, thus, absence of the driving force for migration). In other words, the mechanical equilibrium at the triple junction is achieved. We also assume that the energy of grain boundary does not depend on its inclination, the neighboring grains are isotropic and the alteration in the boundary energy is only through the effect of pressure. In this case the contact angle 2θ reflects the balance between the energies of boundaries GB1, GB2 and GB3 at constant temperature T and pressure p:

$$2\gamma_b \cos\theta = \gamma_3. \tag{6.29}$$

[8] In what follows we consider only the hydrostatic gas pressure

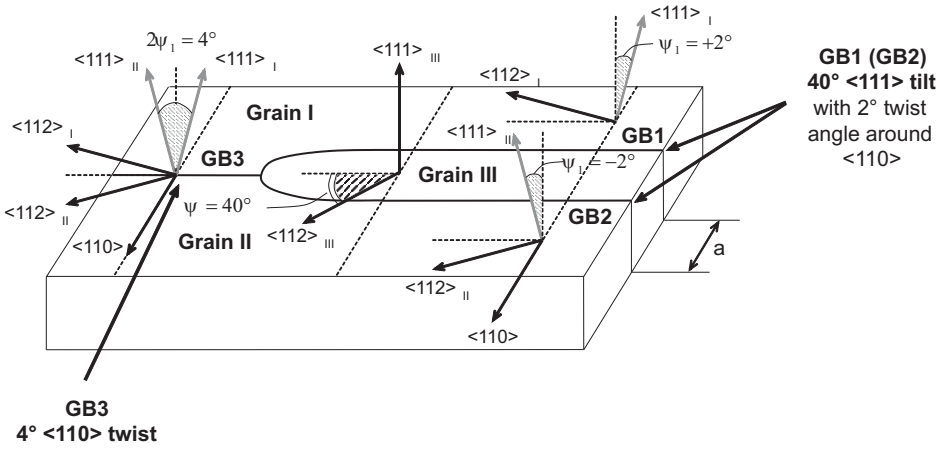

Figure 6.7: Configuration of grown tricrystals

If γ_3 is known, then the energy γ_b of high-angle grain boundaries GB1 and GB2 can be obtained measuring the contact angle 2θ. The increase in the pressure exerts increasing the energy of the grain boundary and, as a result, the changes in the contact angle 2θ. Notice that the energy of all three grain boundaries is affected by the pressure. Of course, it varies differently from boundary to boundary. The advantage of the tricrystal technique is that it is possible, as it is shown below, to create a feasible tricrystal configuration where the grain boundary energy and its pressure dependence are known for one of the grain boundaries (GB3) and other grain boundaries (GB1 and GB2) are the same (have the same crystallographic structure). In this case Eq. (6.29) can be directly applied to determine the energy γ_b of GB1 (GB2) at given temperature and pressure.

6.3 Experimental

In this paragraph the tricrystal configuration and experimental technique are introduced. The experiments were carried out on tricrystals of high pure aluminum (99.9995 wt. %, Al I, see Appendix A). The tricrystal configuration utilized is shown in Fig. 6.7. Two high angle grain boundaries GB1 and GB2 have the same disorientation. As was mentioned in Chapter 1, there are many ways to describe the disorientation between two crystallites. In this case we define the disorientation in terms of the rotation axis <hkl> and

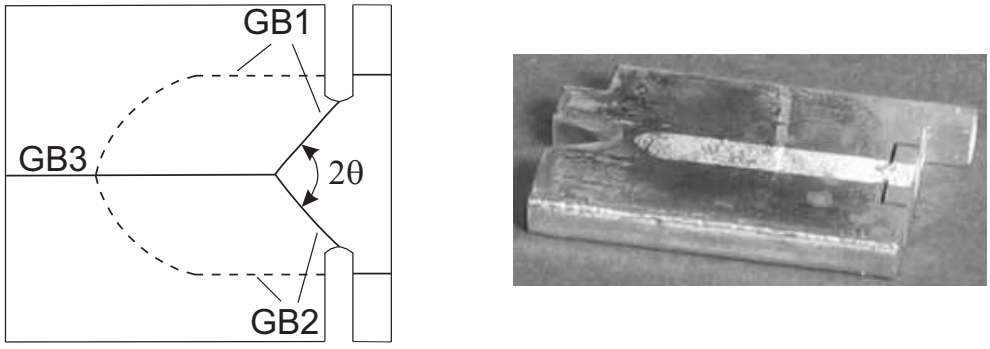

(a) (b)

Figure 6.8: (a) Tricrystal specimen for the measurement of the excess free volume of grain boundary. Dotted line represents a grain boundary location before the annealing experiment, solid line – after the annealing experiment. 2θ is a measured contact angle. (b) Specimen photograph before the experiment

the misorientation angle ψ. Thus, the 40° <111> tilt boundaries GB1 and GB2 are superimposed by a rotation around the axis perpendicular to the grain boundary plane by the angle $\psi_1 = \pm 2°$ (Fig. 6.7). In what follows we call this boundary as a 40° <111> tilt boundary with ±2° twist component. GB3 is a low-angle *twist* grain boundary with the rotation axis <110> and the misorientation angle $2\psi_1 = 4°$; its energy γ_3 can be calculated according to Read and Shockley [3].

The investigations were conducted at hydrostatic pressure up to 14 kbar and at constant temperature of 630°C. The temperature of annealing was kept constant with an accuracy of ±1°. The specimens were exposed to the high gas pressure (pressurized nitrogen atmosphere) and then were annealed during 1 hour at 630°. The pressure was kept constant within ±0.05 kbar. The gas pressure equipment is not discussed here due to its complexity and copyright restrictions but the details can be found elsewhere [65]. The contact angle 2θ (Fig. 6.6b) was measured after the experiment with an optical microscope (Fig. 6.9) and with a SEM (Fig. 6.10). The middle grain of the specimen was notched by two straight cuts made by the electrical discharge machine (EDM) (Fig. 6.8). In such configuration grain boundaries with the triple junction migrate under the action of the capillary driving force until they are stopped by the notches (Fig. 6.8a). It should be emphasized that the measured contact angle 2θ at the triple junction really achieves its *equilibrium*

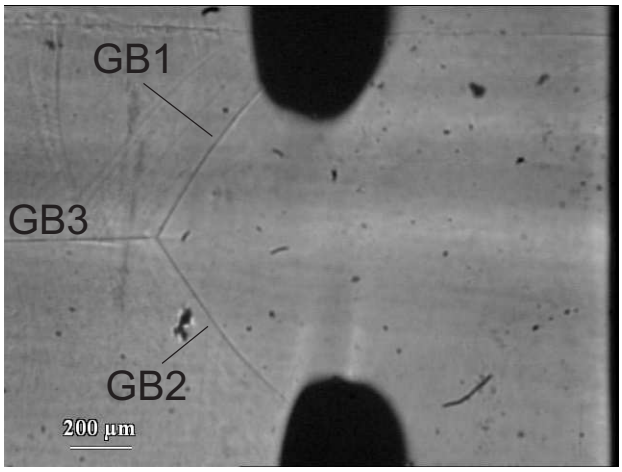

Figure 6.9: Tricriystal specimen after annealing. Optic microscop, thermal groove

value since the system achieves the configuration with a minimum of the free energy. This is demonstrated in Fig. 6.9. Two high-angle grain boundaries are almost straight and, thus, have a minimum area; their contribution to the total free energy of the system is minimum. It must be also underlined that in the proposed experimental method the grain boundaries had moved fast enough before they reached the notches and, therefore, thermal groove dragging can be neglected [41].

6.4 Low angle twist grain boundary under hydrostatic pressure

As mentioned above, the energy of high-angle grain boundary can be calculated through the measurements of the contact angle 2θ by Eq. (6.29). However, the value of γ_3 and its pressure dependence should be known.

Before we discuss the behavior of a low-angle twist grain boundary in the hydrostatic stress field let us remind the basic elements of the theory of elasticity [66, 67]. The stress state of a volume element is given by the stress

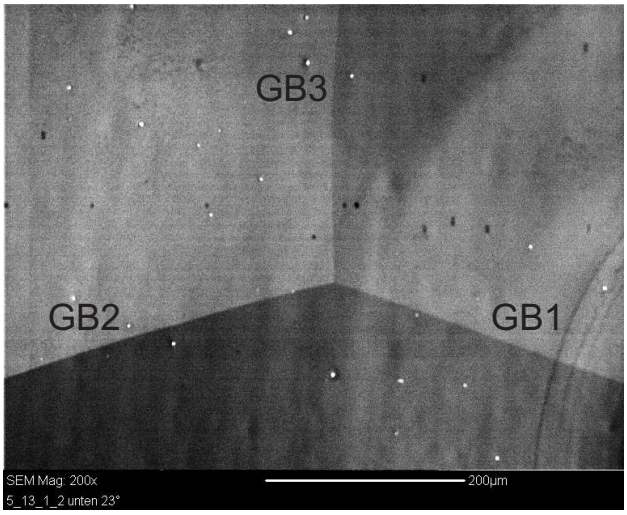

Figure 6.10: Tricrystal specimen after annealing. SEM, orientational contrast

tensor σ which has nine stress components

$$\sigma = \begin{bmatrix} \sigma_{xx} & \sigma_{xy} & \sigma_{xz} \\ \sigma_{yx} & \sigma_{yy} & \sigma_{yz} \\ \sigma_{zx} & \sigma_{zy} & \sigma_{zz} \end{bmatrix}. \tag{6.30}$$

The stress tensor is always symmetrical, i.e. $\sigma_{ij} = \sigma_{ji}$ and therefore it has only six independent components (σ_{xx}, σ_{xy}, σ_{xz} – normal stresses and σ_{xy}, σ_{xz}, σ_{yz} – shear stresses). It is convenient to decompose the stress tensor into a hydrostatic part σ_h and deviatoric part σ_d. In this respect, for hydrostatic stress only normal components are non-zero and the stress tensor has a following appearance

$$\sigma_h = \begin{bmatrix} \sigma_{xx} & 0 & 0 \\ 0 & \sigma_{yy} & 0 \\ 0 & 0 & \sigma_{zz} \end{bmatrix}. \tag{6.31}$$

Since the hydrostatic stress has been introduced, let us return to a low-angle grain boundary in the hydrostatic stress field. As follows from the dislocation model of low-angle grain boundaries proposed by Read-Shockley the low-angle grain boundary is entirely comprised of a periodic crystal dislocations [3]. In particular, a low-angle twist grain boundary requires three sets of screw dislocations.

The structure of dislocation is defined on an atomic level. The introduction of a dislocation in a perfect crystal causes an elastic distortion of the crystal lattice. The distortion field comprises of both: the distortion associated with the dislocation core and the distortion associated with the elastic strain field of the dislocation. The stress tensor for a screw dislocation (apart from dislocation core) is given by

$$\sigma^{(s)} = \begin{bmatrix} 0 & 0 & \tau_{xz} \\ 0 & 0 & \tau_{yz} \\ \tau_{xz} & \tau_{yz} & 0 \end{bmatrix}. \tag{6.32}$$

Normal components of the stress tensor for the screw dislocation are zero. It allows concluding that the stress state of the screw dislocation and, thus, its elastic energy associated with the elastic strain field E_{el}, is not affected by the hydrostatic pressure which is defined by Eq. (6.31). The elastic energy of a screw dislocation (per unit length) is

$$E_{el}^{(s)} = L \cdot \frac{Gb^2}{4\pi}, \tag{6.33}$$

where G is the shear modulus, b is the lattice Burgers vector, L is the dislocation length [66]. However, Eq. (6.33) does not take into account the energy of the dislocation core. It is usually assumed that in the dislocation core the stress corresponds to the theoretical shear stress

$$\frac{E_{core}}{L} \cong \frac{\tau_{th}^2}{2G} \cdot \pi r_0^2 = \left(\frac{G}{2\pi}\right)^2 \frac{\pi r_0^2}{2G} \cong \frac{Gb^2}{8\pi}. \tag{6.34}$$

The total energy of a screw disclocation (per unit length) is given in [66] by

$$E^s = \frac{E_{el}^{(s)}}{L} + \frac{E_{core}}{L} = \frac{Gb^2}{4\pi}\left(\ln\frac{R_0}{r_0} + 1\right), \tag{6.35}$$

where r_0 is the radius of the dislocation core and R_0 has a meaning of the mean grain size. Since the ratio R_0/r_0 is usually very large $(10^5 - 10^7)$ the contribution of the dislocation core to the total dislocation energy is small (the energy of dislocation core E_{core} is not more that 10% from the total energy of the dislocation).

The above analysis shows that the energy of a screw dislocation and, thus, that of a low-angle twist grain boundary may depend on the hydrostatic pressure but only to the small extent associated with the energy of the

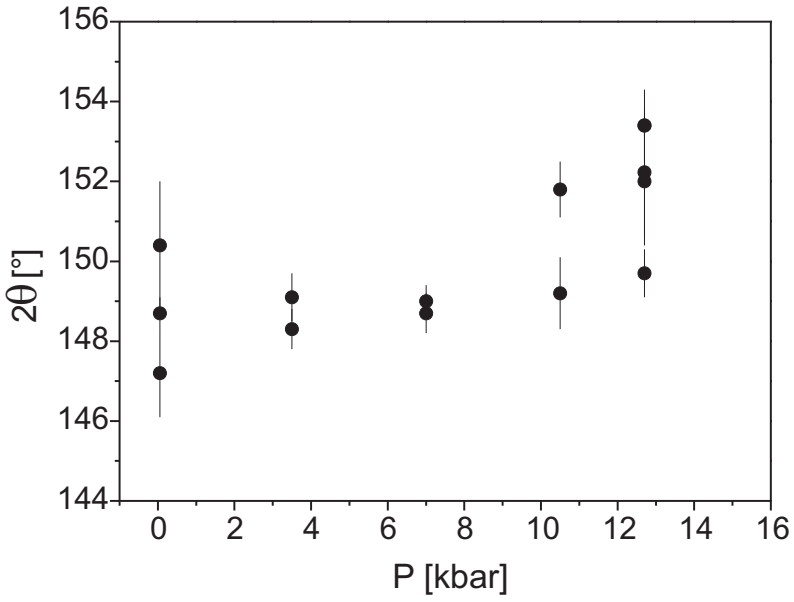

Figure 6.11: Measured contact angle 2θ vs. pressure

dislocation core. On the other hand, there are no reasons to expect that this dependence is strong. In the proposed thermodynamic method we neglect the possible extent of the dislocation core to the total energy of the screw dislocation and therefore we assumed that the energy of the low-angle grain boundary GB3 is not affected by the hydrostatic pressure.[9]

6.5 Excess free volume of <111> high-angle grain boundaries in Al

Results of contact angle measurements are summarized in Fig. 6.11 and in Tabl. 6.2. All measurements were carried out at constant temprature of 630°C. The dependence between the contact angle 2θ and the hydrostatic pressure was confirmed. The increase in the pressure applied to the system exerts the increase in the measured contact angle.

The relationship between the contact angle and the hydrostatic pressure

[9] We also assume that the magnitude of the Burgers vector does depend on the pressure

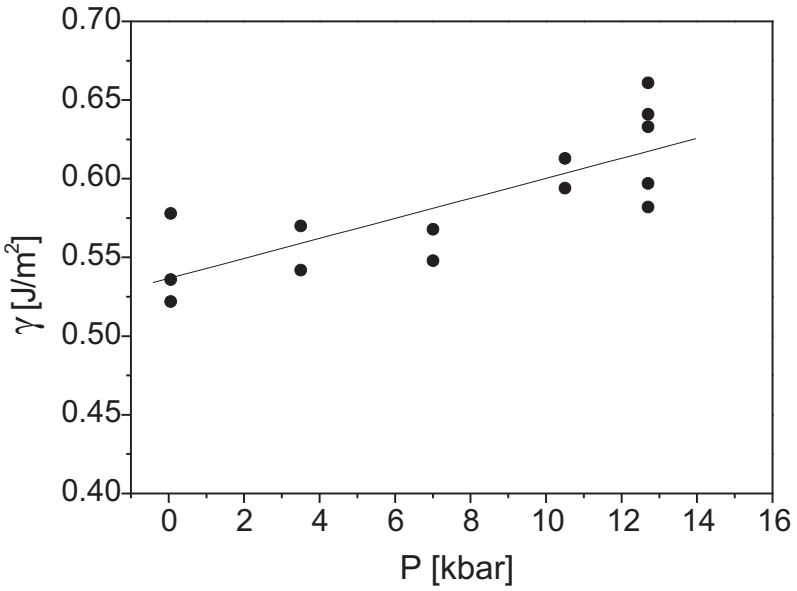

Figure 6.12: Calculated grain boundary energy γ_b vs. pressure

may be obtained by substituting Eq. (6.29) in Eq. (6.26):

$$2\frac{\partial\gamma_b}{\partial p}\cos\theta - 2\gamma_b \sin\theta\frac{\partial\theta}{\partial p} = \frac{\partial\gamma_3}{\partial p}. \tag{6.36}$$

As shown above we can neglect the pressure dependence of the low-angle twist grain boundary GB3:

$$\frac{\partial\gamma_3}{\partial p} = 0, \tag{6.37}$$

and then we get

$$V^{ex} = \left.\frac{\partial\gamma_b}{\partial p}\right|_T = \frac{\gamma_b \sin\theta\frac{\partial\theta}{\partial p}}{\cos\theta} = \gamma_3 \tan\theta\frac{\partial\theta}{\partial p}. \tag{6.38}$$

This equation links a thermodynamic parameter – the excess free volume with macroscopic parameters – the contact angle and pressure which can be measured in experiments.

The utilized triple junction method is based upon the assumption that all tricrystal specimens underwent high temperature annealing at different pressures are *identical*. In reality, however, it is impossible to produce absolutely

Table 6.2: Measured contact angle 2θ and calculated grain boundary energy γ_3 and γ_b at different pressures

pressure $[kbar]$	2θ [°]	γ_3 $[J/m^2]$	γ_b $[J/m^2]$	specimen
0.05	148.7 ± 0.4	0.289	0.536	13_1_1_b
	150.4 ± 1.6	0.295	0.578	14_2_t
	147.2 ± 1.1	0.295	0.522	14_2_b
3.5	148.3 ± 0.5	0.256	0.542	9_2_1_a
	149.1 ± 0.6	0.304	0.570	11_2_b
7.0	148.7 ± 0.5	0.256	0.548	9_1_2_t
	149.0 ± 0.4	0.304	0.568	11_3_b
10.5	151.8 ± 0.7	0.289	0.594	13_1_2_a
	149.2 ± 0.9	0.327	0.613	17_1_2_a
12.7	153.4 ± 0.9	0.304	0.661	11_1_t
	149.7 ± 0.6	0.304	0.582	11_1_b
	152.2 ± 1.6	0.304	0.633	11_4_a
	152.0 ± 1.6	0.289	0.597	13_2_2_a
	153.4 ± 0.25	0.295	0.641	14_1_a

identical tricrystals. The orientations of grains in the grown tricrystals deviate slightly from the desired orientations. This fact leads to variations in the disorientation of the neighboring grains (Tabl. B.5, see Appendix B). Variations in the misorientation angle of ±0.5° can cause the significant difference in the energy of the low angle grain boundary, but for the energy of the high angle grain boundary such variations should not play a prominent role (Fig. 1.3). Consequently, Eq. (6.38) cannot be applied directly to calculate the BFV from the contact angle – pressure dependence. However, the value of the BFV can be obtained from Eq. (6.26). For the sake of convenience we repeat it here:

$$\left(\frac{\partial \gamma_b}{\partial p}\right)_T = -\Gamma_0 \Omega_a = V^{ex}. \tag{6.39}$$

The energy of high angle grain boundaries γ_b was calculated in accordance with Eq. (6.29) for every tricrystal specimen.

The energy of the low angle twist grain boundary γ_3 was calculated ac-

Table 6.3: Autoadsorption Γ_0 and excess free volume V^{ex} for 40° <111> grain boundary

$\partial\gamma_b/\partial p$ $(T = 630°)$	$6.4 \cdot 10^{-11}\ m$
$\Gamma_0 = -\Omega_a^{-1}\,(\partial\gamma_b/\partial p)$ (at. volume $\Omega_a = 10^{-5}\ m^3/mol$)	$-6.4 \cdot 10^{-6}\ mol/m^2$
$V^{ex} = -\Gamma_0\Omega_a$	$6.4 \cdot 10^{-11} \pm 2.1 \cdot 10^{-11}\ m^3/m^2$

cording to Read and Shockley [3] and reads

$$\gamma_3 = \gamma_{LA}^{twist} = 2\frac{G\bar{b}}{4\pi}\psi_1\,(A - \ln\psi_1)\,, \tag{6.40}$$

where $\bar{b} = \frac{\sqrt{2}}{2} = 4.05 \cdot 10^{-10} \cdot \frac{a\sqrt{2}}{2} = 2.86 \cdot 10^{-10}\ m$ is the Burgers vector, $G = 26.4\ GPa$ is the shear modulus, ψ_1 is the misorientation angle, $A = 0.5$ reflects the energy of the dislocation core [68].[10] Results of the these calculations are summurized in Tabl. 6.2 and in Fig. (6.12)

Generally, the relationship between the energy and pressure is not known and can have a complex character. To simplify the problem we approximate the experimental dependence by a linear function. However, our experimental method allows us finding the derivative $\partial\gamma_b/\partial p$ at any point of the $\gamma_b(p)$ dependence. We also assume that there are no phase transitions at grain boundaries (like grain boundary melting or any structural transition). The corresponding relationship is given by

$$\gamma_b = \gamma_0 + \frac{\partial\gamma_b}{\partial p}p, \tag{6.41}$$

where $\gamma_0 = 0.537\ [J/m^2]$ and $\frac{\partial\gamma_b}{\partial p} = 6.4 \cdot 10^{-11}\ [m]$ are the linear regression coefficients. Finally, the autoadsorption and the excess free volume of 40° <111> tilt grain boundary with ±2° twist component were calculated. They are represented in Tabl. 6.3. It should be recorded, that the obtained quantity $V^{ex} = \Gamma_0\Omega_a$ does not depend on the grain boundary model (thickness of grain

[10] Assuming that 4° <110> twist grain boundary consists of 2 sets of lattice screw dislocations

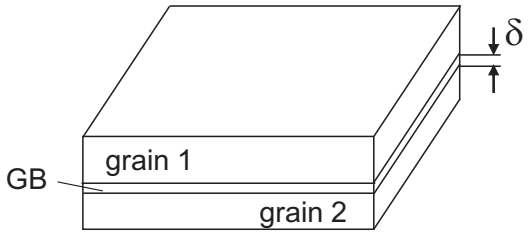

Figure 6.13: Grain boundary as a thin layer

boundary), since in the thermodynamic method no such assumption was made. The proposed measurement technique makes it possible to estimate the BFV for the wide range of grain boundary orientations with rather high accuracy.

The autoadsorption (or BFV) provides the way to estimate the material density in a grain boundary. Let us consider a grain boundary as a thin layer (Fig. 6.13). It is usually assumed (for instance, in grain boundary diffusion models) that grain boundary thickness δ is about 10^{-9} m. In this case the difference in material densities of the boundary and the bulk of the grain is given by

$$\frac{\rho_b}{\rho_0} = 1 + \frac{\Gamma_0}{\delta/\Omega_a} \approx 0.94, \tag{6.42}$$

where δ/Ω_a is the material density of the bulk per atomic volume. Thus, the material density of the 40° <111> tilt boundary with ±2° twist component in Al is 6% less then that of the bulk.[11]

To check the obtained results the pressure dependence of the contact angle 2θ was measured for the triple junction with two 40° <111> tilt grain boundaries as GB1 and GB2 and an 80° <111> tilt boundary as GB3. Due to the crystal symmetry the 80° <111> boundary corresponds to the −40° <111> boundary and the energy of GB3 should be the same as that of GB1 and GB2.[12] Tricrystals with three 40° <111> tilt boundaries were annealed in the high gas pressure atmosphere. Results of contact angle measurements are shown in Fig. 6.14. As was expected, the measured angle was about 120°

[11] There is no thermodynamic limitation for the boundary density to be higher than that of the bulk; it is traditionally assumed that the interface has a smaller density than the bulk

[12] Certainly, these boundaries differ in their inclination, nowever, how has been shown in Chapter 2 for the <111> rotation axis the effect of plane inclination may be neglected

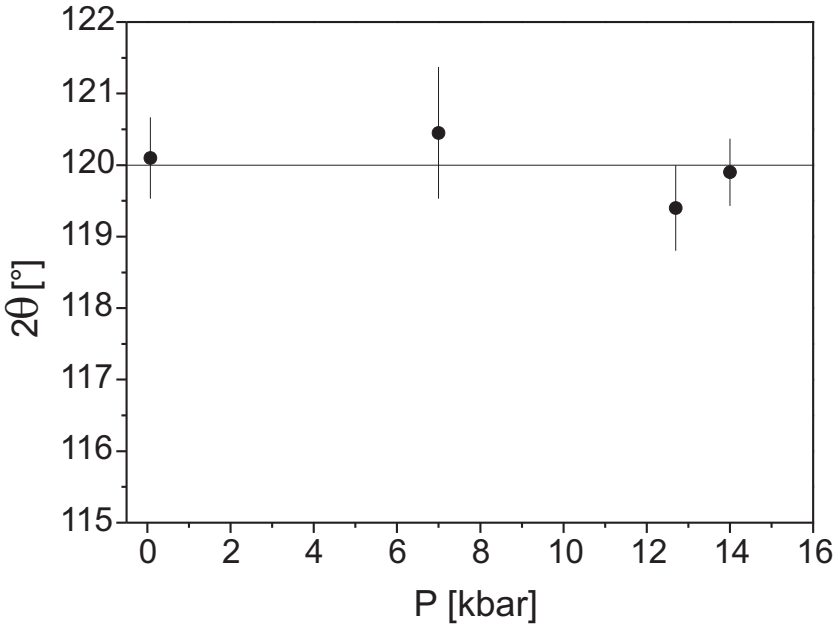

Figure 6.14: Contact angle 2θ vs. pressure for tricrystal sample with three 40° <111> tilt grain boundaries

in the whole range of pressure and, what is of importance $\left(\frac{\partial\theta}{\partial p}\right)\Big|_T = 0$. This result also confirms that for <111> rotation axis the effect of grain boundary plane inclination on the grain boundary energy is very small.

6.6 Summary

A new experimental method to determine thermodynamic characteristics of grain boundaries (the autoadsorption and the excess free volume) was developed. The autoadsorption and the BFV were measured for 40° <111> tilt boundary with ±2° twist component in Al tricrystals and were found to be equal to $-6.4 \cdot 10^{-6}\ mol/m^2$ and $6.4 \cdot 10^{-11}\ m^3/m^2$ accordingly. Note that in the used experimental method no assumptions regarding boundary thickness are made. The obtained thermodynamic entities define the absolute values of grain boundary characteristics. To check the results the tricrystal specimens with three 40° <111> tilt grain boundaries were also studied. These

measurements revealed that the contact angle is about 120° and does not change in the whole range of pressures.

The proposed thermodynamic method provides a new avenue to obtain the quantitative information on properties of grain boundaries. In particular, it can be used to study the transition between low and high angle grain boundaries by measuring the contact angle at the constant high pressure for the triple junctions where the misorientation of one of the boundaries (for instance, GB3 in Fig. 6.8b) changes continuously from low to high angles. The extremum on the contact angle – misorientation diagram will correspond to the transition in the structure of the boundary. The segregation of different sorts of solute atoms can be studied as well.

Chapter 7

Summary and outlook

The recent development in experimental research on grain boundary migration and grain boundary structure in metals is reviewed in the this manuscript. The dependence of grain boundary migration on the boundary character (disorientation between the grains and boundary plane inclination), temperature, solute atoms content is addressed. New thermodynamic method for experimental measurement of the grain boundary excess free volume is introduced.

The migration of solitary grain boundaries and triple junctions was studied in specially fabricated bi- and tricrystals of aluminum. X-ray interface Continuous Tracking Device and Back-Scattered Electron Diffraction in a SEM were used for real-time tracking of the grain boundary position in specimens. Both methods do not interfere with the process of grain boundary motion and allow to determine the grain boundary or triple junction position at any moment of the experiment. The SEM method also allows to record the shape of the moving boundary.

The motion of <111> tilt and mixed tilt-twist grain boundaries with misorientation angle in the range between 34° and 42° was studied in Al-bicrystals.

The experiments revealed that the change of the sets of boundary planes in the curved moving tilt grain boundary does not affect its steady-state motion.

The shape of the moving mixed tilt-twist grain boundary was measured and compared with the analytically calculated boundary shape. Results show that an increase in the twist component along the curved mixed boundary does not affect its steady state motion. Similar to the behavior of <111>

pure tilt boundaries, the mobility of <111> mixed tilt-twist boundaries depends on the misorientation angle in a non-monotonic fashion. It allows us concluding that in high-pure aluminum the curved boundaries in both configurations, pure tilt with differently inclined boundary elements, and mixed tilt-twist, demonstrate essentially the same behavior with regard to the misorientation dependence of their motion. However, the effect of boundary character might be important in ultra-pure metals.

The interaction of the moving grain boundary with an external specimen surface was studied. The motion of curved mixed grain boundaries with <111> and <112> rotation axes was measured in bicrystals of pure aluminum over the temperature range between 315°C and 480°C. The results were analyzed with respect to a potential drag effect of the surface triple junction and the effect of anysotropy of the external specimen surface on boundary migration.

The obtained linear relationship between the boundary velocity and the driving force manifests that boundary velocity is only determined by the boundary mobility and thus, is not affected by the surface junction. Measurements of the contact angle at the tip of the boundary and the resulting magnitude of the criterion Λ, which describes the impact of the junction on the boundary motion, confirm this conclusion.

Motion of curved grain boundaries was also studied in bicrystals with the strong anysotropy of the (specific) surface free energy of the adjoining grains. The migration of 90° <112> grain boundaries in quarter-loop geometry was investigated. The complex shape of the moving grain boundary was observed. The shape of the moving grain boundary changes with the temperature of the experiment, but it does not change at a constant temperature. The velocity of the moving grain boundary and its shape were found to be constant at a constant temperature. This fact allows to conclude that the studied grain boundaries move in the steady-state regime at a constant temperature. The relationship between the contact angle on the top/bottom and lateral specimen surfaces was derived. It has been shown that the moving grain boundary can have various shapes if the free energy reaches its minimum.

The motion of connected grain boundaries (grain boundaries with a triple junction) was investigated in Al-tricrystals with different concentrations of Mg atoms in the temperature range between 270°C and 500°C. The triple junction was formed by two 40° <111> tilt grain boundaries with ±4° twist

component and a 8° <110> low angle twist grain boundary. The effect of Mg atoms on grain boundary and triple junction mobilities was measured.

The activation parameters, activation enthalpy and pre-exponential factor, were found to depend on the Mg concentrarion. In the concentration range between 0.2 and 100 wt. ppm of Mg the reduced grain boundary mobility A_{gb} increases linearly with inverse Mg concentration and it has a reasonable agreement with the impurity drag theory of Lücke and Detert. For the higher Mg content (1000 wt. ppm) the dependence of grain boundary mobility on the Mg concentration cannot be described by this theory.

In the studied temperature range the motion of grain boundaries with the triple junction was controled by grain boundary kinetics. The criterion Λ, which reflects the drag effect of triple junction, essentially decreases with increasing the Mg concentration and therefore the "dragging" influence of triple junction on the motion of the connected boundaries intensifies.

A new expeimental method to determine the thermodynamic characteristics of grain boundaries (the autoadsoption and the excess free volume) was designed. The pressure dependence of grain boundary energy was studied in tricrystals of Al. The contact angle between the grain boundaries reflectes the balance of thier energies. From the contact angle measurements the excess free volume of the 40° <111> tilt boundary with a ±2° twist component was determined.

To verify the obtained results the pressure dependence of the contact angle was measured for the triple junction with three the same grain boundaries. The measured contact angle was about 120° in the whole range of pressures.

Proposed thermodynamic method provides a way to measure the excess free volume of different classes of grain boundaries. The segregation of various sorts of solute atoms can be also studied using this technique.

In conclusion we believe that the results of the presented studies migth lead to deeper understanding of grain boundaries and their role in modern materials science.

Bibliography

[1] Saylor DM, El Dasher BS, Rollett AD, Rohrer GS. Acta Mater. 2004;52;3649

[2] Saylor DM, Morawiec A, Rohrer GS. Acta Mater. 2003;51;3663

[3] Read WT, Shockley W. Phys. Review, 1950;28;275

[4] Pond RC, Smith DA. Int. Met. Review 1976;21;61

[5] Howe JM: Interfaces in Materials, John Wiley & Sons, Inc., New York 1997

[6] Bollman W: Crystal defects and Crystalline Interfaces, Springer, Berlin-Heidelberg 1970

[7] Sutton AP, Vitek V. Phil. Trans. R. Soc. London 1983;A309;1

[8] Bokstein BS: Diffuziya v Metallah (Diffusion in Metals), Metallurgia, Moscow 1978 [in Russian]

[9] Gottstein G, Shvindlerman LS: Grain boundary migration in metals, CRC Press, USA 1999

[10] Cahn JW, Mishin Y, Suzuki A to be published

[11] Cahn JW, Mishin Y, Suzuki A Philosophical Magazine 2006;54;4953

[12] Rath BB, Hu H: The nature and behaviour of grain boundaries (Hu H, editor), Plenum Press, New York 1972

[13] Sun RS, Bauer CL. Acta Metall. 1975;49;635

[14] Dunn CG, Daniels FW, Bolton MJ. Trans AIME 1949;185;708

[15] Molodov DA: Migration of high angle grain boundaries in metals, Shaker Verlag, Aachen 1999

[16] Mattissen D: In-situ Untersuchung des Einflusses der Tripelpunkte auf die Korngrenzebewegung in Aluminium, Shaker Verlag, Aachen 2004

[17] Czubayko U, Molodov DA, Petersen B-Ch, Gottstein G, Shvindlerman LS. Meas. Sci. Technol. 1995;6;947

[18] Aristov VYu, Mirochnik VL, Shvindlerman LS. Sov. Phys. Sol. State, 1976;18;137

[19] Molodov DA, Czubayko U, Shvindlerman LS, Gottstein G. Acta Mater., 1998;46;553

[20] Upmanyu M, Srolovitz DJ, Shvindlerman LS, Gottstein G. Acta Mater., 1999;47;3901

[21] Schönfelder B, Gottstein G, Shvindlerman LS. to be published

[22] Gottstein G, Murmann HS, Renner G, Simpson C, Lücke K: Textures of Materials (Gottstein G, Lücke K, editors), Springer Verlag, Berlin 1978

[23] Molodov DA, Gottstein G, Heringhaus F, Shvindlerman LS. Scripta Mater., 1997;32;529

[24] Zhang H, Srolovitz DJ. Scripta Mater., 2005;52;1193

[25] Fradkov VE, Shvindlerman LS. Phis. Chem. Mech. Surface, 1982;1;180

[26] Straumal BB, Sursaeva VG, Shvindlerman LS. Phys. Met. Matalloved., 1980;49(5);102

[27] Molodov DA. Dissertation, Moscow 1995 [in Russian]

[28] Verhasselt JCh, Gottstein G, Molodov DA, Shvindlerman LS. Acta Mater., 1999;47;887

[29] Lücke K, Detert K. Acta Metall. 1957;5;628

[30] Czubayko U, Sursaeva VG, Gottstein G, Shvindlerman LS. Acta Mater., 1998;46;5863

[31] Protasova SG, Gottstein G, Molodov DA, Sursaeva VG, Shvindlerman LS. Acta Mater., 2001;49;2519

[32] Gottstein G, Shvindlerman LS. Acta Mater., 2002;50;703

[33] Gottstein G, Shvindlerman LS. Acta Mater., 2005;53;1535

[34] Gottstein G, Shvindlerman LS. Accepted for publication to Mat. Science and Technology (2005)

[35] Min D, Wong H. Acta Mater., 2002;50;5155

[36] Molodov DV, Gottstein G, Heringhaus F, Shvindlerman LS. Acta Mater., 1998;46;5627

[37] Aristov VYu, Kopetski ChV, Shvindlerman LS in: Theoretical fundamentals of Materials Science, Nauka, Moscow 1981, p.84 [in Russian]

[38] Gottstein G, Shvindlerman LS. Scripta Mater., 1992;27;1521

[39] Mullins WW. J. Appl. Phys. 1957;28;333

[40] Mullins WW, Trans AIME, 1960;218;354

[41] Aristov VYu, Fradkov VE, Shvindlerman LS. Phys. Met. Metall., 1978;45(5);997 [in Russian]

[42] Galina AV, Fradkov VE, Shvindlerman LS. Phys. Met. Metall., 1987;63;165

[43] Upmanyu M, Srolovitz DJ, Shvindlerman LS, Gottstein G. Acta Mater., 2002;50;1405

[44] Mullins WW. J. Appl. Phys. 1956;27;900

[45] Gottstein G, Shvindlerman LS. Acta Mater., 2002;50;703

[46] Mattissen D, Molodov DA, Shvindlerman LS, Gottstein G. Acta Mater. 2005;53;2049

[47] Gottstein G, Ma Y, Shvindlerman LS. Acta Mater. 2005;53;1535

[48] Lundy TS, Murdoch JF. J. Appl. Phys. 1962;53;1671

[49] Beyeler M. J. Phys. (Fr) 1968;29;345

[50] Rafalski AL, Harvey MR, Reifenberg DH. Trans Quarterly 1967;60;721

[51] Van Swygenhoven H, Derlet PM. Physical review B, 2001;64;224105

[52] Wynblatt P, Takashima M. to be published

[53] Wu J. Int. J. Engng., 2004;20(2);293

[54] Knizhnik GS. Poverhnost: Fizika, Khimia, mehanika, 1981;5;50 [in Russian]

[55] Wolf D. Scripta Metall., 1989;23(11);1913

[56] Wolf D. J. Appl. Phys., 1990;68(7);3221

[57] Wolf D. Scripta Metall. Mater., 1990;38(5);781

[58] Frost HJ, Ashby MF, Spaepen F. Scripta Metall., 1980;14;1051

[59] Stremel MA, Markovitch AL, [in Russian]

[60] Stremel MA, Markovitch AL, Poverhnost: Rentgenovskie, sinhrotronnii i neitronnii issledovaniya [in Russian], 1997;1;85

[61] Buckett KI, Merkle KL. Ultramicroscopy, 1994;56;71

[62] Merkle KL, Csencsits R, Rynes KL, Withrow JP, Stadelmann PA. J. of Microscopy, 1998;190;204

[63] Zhang H, Srolovotz DJ. "Simulation and Analysis of the Migration Mechanism of S5 Tilt Grain Boundary in an FCC Metal" in preparation

[64] Meiser H, Gleite H. Scripta Metall., 1980;14;1980

[65] Straumal B, Rabkin E, Łojkowski W, Gust W, Shvindlerman LS. Acta Mat., 1997;45;1931

[66] Gottstein G: Physical foundations of material science, Springer, Berlin 2004

[67] Stremel MA: Prochnost splavov [in Russian], MISIS 1999

[68] Merwe JH. Proc. Phys. Soc., 1950:A63:616

[69] Rodrigues O. de Mathematiques Pures et Appliquees, 1840;5;380

[70] www.lhup.edu/~dsimanek/physics.htm

Appendix A

Chemical composition of studied materials

Bi- and tricrystals were produced from high pure aluminum of two different charges from Hydro Aluminium AG, Germany (99.9995 wt. %, Al I and 99.9999 wt.%, Al II) and from Al-alloys (based on Al II) doped with magnesium (99.99 wt. %) produced at the IMM (Al III, Al IV, Al V).

The impurity concentration was determined with the high accuracy by the glow discharge mass-spectroscopy (GDMS). The results of several GDMS analysises are summurized in Tabl. A.1 where the concentration of elements (bold font) and low limits of the analysis (normal font) are given.

In Al-Mg alloys (Al III, Al IV, Al V), only the concentration of Mg-atoms was measured after their production. The concentration of other elements was not specially analyzed.

The total impurity concentration is given in accordance to the certifcate of the analysis provided by the manufacturer for Al I and Al II and in accordance to the GDMS analysis for the home-produced alloys.

Table A.1: Concentration of impurities in Al of different charges in wt. ppb

	Aluminum				
	Al I	Al II	Al III	Al IV	Al V
Ag	<100	<5	$<10^3$	$<10^3$	$<10^3$
As	<500	<5	$<10^3$	$<10^3$	$<10^3$
Au	-	-	-	-	-
B	<200	<5	$<10^3$	$<10^3$	$<10^3$
Ba	<200	<5	$<10^3$	$<10^3$	$<10^3$
Be	<100	<5	$<10^3$	$<10^3$	$<10^3$
Bi	<500	<5	-	-	-
Ca	<400	<2	$<10^3$	$<10^3$	$<10^3$
Ce	**432**	<5	$<10^3$	$<10^3$	$<10^3$
Cl	$<10^3$	<100	-	-	-
Co	<100	<5	$<10^3$	$<10^3$	$<10^3$
Cr	<400	**34**	$<10^3$	$<10^3$	$<10^3$
Cs	<500	<5	$<10^3$	$<10^3$	$<10^3$
Cu	$<10^3$	<40	$<10^3$	$<10^3$	$<10^3$
F	<900	<100	-	-	-
Fe	<700	**123**	$<10^3$	$<10^3$	$<10^3$
Ga	<100	<5	$<10^3$	$<10^3$	$<10^3$
Ge	$<10^3$	<40	$<10^3$	$<10^3$	$<10^3$
In	<500	<5	$<10^3$	$<10^3$	$<10^3$
K	<400	<100	-	-	-
La	**206**	<5	$<10^3$	$<10^3$	$<10^3$
Li	<100	<5	$<10^3$	$<10^3$	$<10^3$
Mg	<800	**181**	$\mathbf{4.85{\cdot}10^4}$	$\mathbf{1.02{\cdot}10^5}$	$\mathbf{1.01{\cdot}10^6}$
Mn	<200	<5	$<10^3$	$<10^3$	$<10^3$
Mo	<200	<5	$<10^3$	$<10^3$	$<10^3$
Na	**15**	<5	$<2{\cdot}10^3$	$<2{\cdot}10^3$	$<2{\cdot}10^3$
Ni	<500	<5	$<10^3$	$<10^3$	$<10^3$
Nd	-	-	-	-	-
O	$<3{\cdot}10^4$	$<10^4$	$<10^3$	$<10^3$	$<10^3$
P	**184**	**28**	-	-	-
Pb	<500	<5	$<10^3$	$<10^3$	$<10^3$
Pd	$<10^3$	<100	$<10^3$	$<10^3$	$<10^3$
Pt	$<10^3$	<100	$<10^3$	$<10^3$	$<10^3$
S	<900	<100	-	-	-
Sb	<800	<5	$<10^3$	$<10^3$	$<10^3$
Si	$\mathbf{10^3}$	**479**	-	-	-
Sn	<500	<5	$<10^3$	$<10^3$	$<10^3$
Ti	<300	128	$<10^3$	$<10^3$	$<10^3$
Th	**24**	<0.35	$<10^3$	$<10^3$	$<10^3$
U	**10**	<0.35	$<10^3$	$<10^3$	$<10^3$
V	$<10^3$	**9**	$<10^3$	$<10^3$	$<10^3$
W	<500	<25	$<10^3$	$<10^3$	$<10^3$
Zn	<300	<5	$<10^3$	$<10^3$	$<10^3$
Zr	<300	<5	$<10^3$	$<10^3$	$<10^3$
Total	$5{\cdot}10^3$	10^3	$4.85{\cdot}10^4$	$1.02{\cdot}10^5$	$1.01{\cdot}10^6$

Appendix B

Orientation of used bi- and tricrystals

Disorientations between the adjacent grains of used bicrystals are presented in terms of the fixed rotation axis <hkl> and the variable rotation (misorientation) angle θ.

The disorientations in used tricrystals are represented in terms of the axis $r(r_x, r_y, r_z)$ and the angle of rotation ω, which can be most convenient represented by its Rodrigues vector $R(R_x, R_y, R_z)$ [69]

$$R = r \tan \frac{\omega}{2} \tag{B.1}$$

in Rodrigues space (Fig. B.1a). For a two-dimensional representation sections through Rodrigues space perpendicular to the Z-axis are shown in Fig. B.1b.

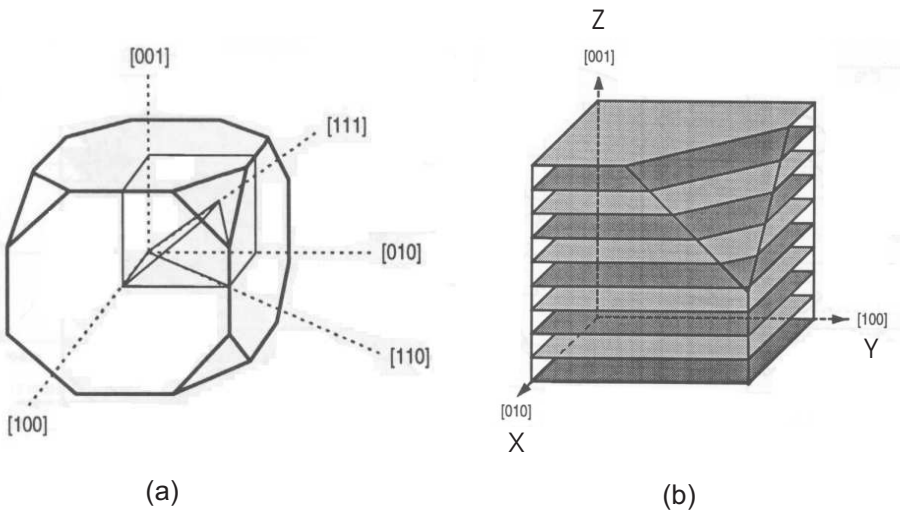

Figure B.1: (a) Fundamental zone of Rodrigues space for cubic metals. (b) One eighth of the fundamental zone with sections through Rodrigues space perpendicular to axis Z [001]

B.0.1 Disorientations between the grains in studied bicrystals

Fig. B.2 shows the misorientation angle θ and misalignments Φ and Ψ of the normal direction with an ideal [111] axis for both adjoining grains.

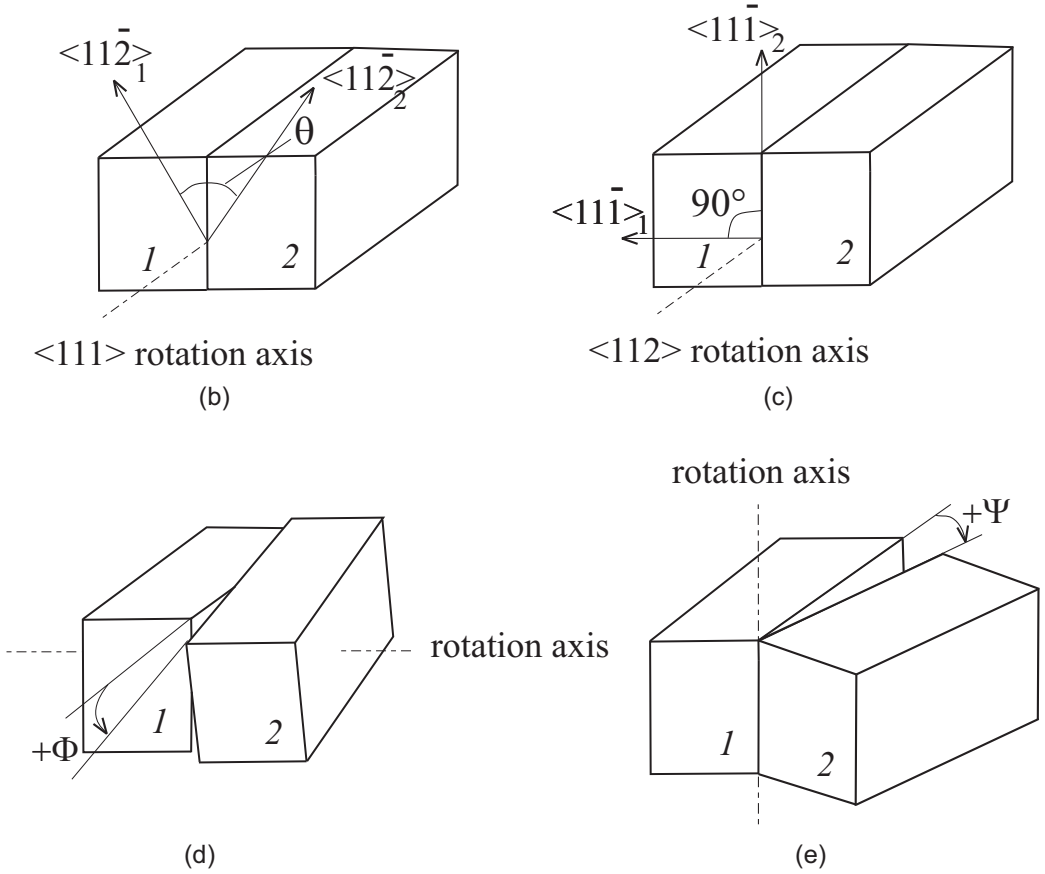

Figure B.2: (a) Tilt grain boundary with rotation axis <111> and misorientation angle θ in studied bicrystals (Chapter 3). (c) Tilt grain boundary with rotation axis <112> and misorientation angle of 90° in studied bicrystals (Chapter 4). (d)-(e) Angles of deviations: (d) twist angle Φ with respect to the rotation axis perpendicular to boundary plane, (e) second tilt angle Ψ with respect to the rotation axies parallel to boundary plane

Table B.1: Disorientations between the grains of bicrystals in Chapter 3

Bicrystal	<hkl>	$\theta°$	grain 1		grain 2	
			$\Phi°$	$\Psi°$	$\Phi°$	$\Psi°$
BI21	<111>	36.8	0.9	1.2	1.2	1.3
AB8	<111>	36.3	1.8	1.7	-0.9	0.2
AB7	<111>	34.3	-2.1	-1.3	-1.3	0.4
2_3	<111>	37.0	1.0	1.8	0.2	0.6
2_8	<111>	37.1	-0.7	0.2	-0.8	0.7
2_18	<111>	37.5	0.5	0.6	-0.9	0.2
2_15	<111>	37.8	-0.1	0.3	-0.2	0.1
2_13	<111>	38.4	-0.4	0.3	-0.5	0.1
2_26	<111>	39.9	0.8	0.3	0.9	-0.8
2_24	<111>	40.1	0.7	0.6	0.6	-0.8
2_14	<111>	40.6	-0.4	-0.1	-0.2	1.2
2_16	<111>	41.3	-0.5	0.4	-0.2	1.2
2_9	<111>	41.9	-0.9	0.1	-0.7	0.5

Table B.2: Disorientations between the grains of bicrystals in Chapter 4

Bicrystal	<hkl>	$\theta°$	grain 1		grain 2	
			$\Phi°$	$\Psi°$	$\Phi°$	$\Psi°$
2_18	<111>	37.5	-0.5	-0.3	0.8	0.0
2_26	<111>	39.9	-0.8	0.3	-0.9	-0.9
2_14	<111>	40.6	0.4	-0.1	0.1	1.5
bk6	<112>	90.9	0.7	-0.5	1.6	-0.4
bk7	<112>	90.7	0.6	-0.6	1.6	-0.1
bk10	<112>	92.3	1.6	-1.4	1.0	-0.9
bk11	<112>	91.4	1.5	-1.1	1.6	-0.3
bk18	<112>	90.6	0.7	-0.3	1.6	-0.4
bk19	<112>	91.2	0.8	-0.3	0.1	-0.9
bk21	<112>	91.4	1.3	-0.3	3.9	-1.1

B.0.2 Disorientations between the grains in studied tricrystals

Series 4 (Chapter 5)

Grain boundaries I and II (between the grains 1 and 3 and between the grains 2 and 3) are 40° <111> tilt grain boundaries with a 4° twist component around <110> axis. Grain boundary III (between the grains 1 and 2) is a 8° <110> twist grain boundary (Tabl. B.3, Fig. B.3).

Table B.3: Disorientations between the grains in tricrystals of series 4

Tricrystal	Neighboring grains	$r_x\ r_y\ r_z$	ω°	R_x	R_y	R_z
tk4_34	1-3	0.64 0.57 0.52	41.82	0.2429	0.2185	0.1980
	2-3	0.62 0.62 0.48	41.55	0.2356	0.2352	0.1817
	1-2	0.71 0.70 0.00	7.72	0.0958	0.0945	0.0000
tk4_41	1-3	0.62 0.57 0.53	41.33	0.2357	0.2155	0.2006
	2-3	0.64 0.62 0.46	42.24	0.2555	0.2397	0.1775
	1-2	0.71 0.70 0.00	7.82	0.0485	0.0478	0.0000
tk4_51	1-3	0.63 0.58 0.51	42.77	0.2471	0.2288	0.2001
	2-3	0.64 0.61 0.48	43.49	0.2536	0.2426	0.1895
	1-2	0.71 0.70 0.01	8.00	0.0496	0.0489	0.0007
tk4_55	1-3	0.64 0.56 0.53	40.31	0.2350	0.2054	0.1931
	2-3	0.66 0.59 0.46	41.83	0.2522	0.2259	0.1772
	1-2	0.71 0.71 0.02	8.73	0.0542	0.0542	0.0015
tk4_59	1-3	0.64 0.56 0.53	42.35	0.2470	0.2164	0.2054
	2-3	0.65 0.59 0.48	41.04	0.2421	0.2205	0.1811
	1-2	0.71 0.71 0.01	7.31	0.0453	0.0453	0.0006

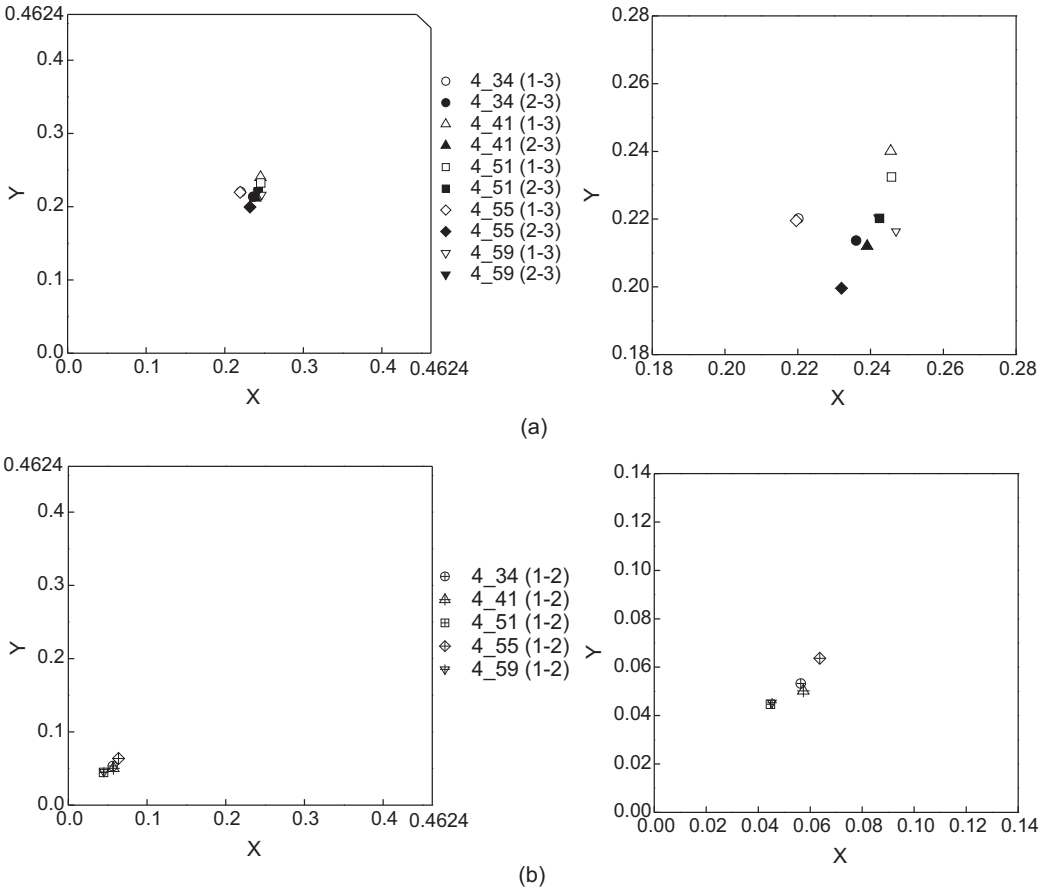

Figure B.3: Sections of Rodrigues space (a) at Z=0.1772..0.2054 with misorientations between grain 1 and grain 3 (1-3) and grain 3 and grain 2 (3-2), (b) at Z=0..0.0015 with misorientations between grain 1 and grain 2 (1-2)

Series 5 (Chapter 6)

Grain boundaries I and II between grains 1 and 3 and between grains 2 and 3 are 40° <111> tilt grain boundaries with 2.25° twist component around <110> axis. Grain boundary III, between grains 1 and 2 is a 4.5° <110> twist grain boundary (Tabl. B.4, Fig. B.4).

Table B.4: Disorientations between the grains in tricrystals of series 5

Tricrystal	Neighboring grains	$r_x\ r_y\ r_z$	ω°	R_x	R_y	R_z
tk5_7	1-3	0.64 0.57 0.52	40.84	0.2383	0.2159	0.1936
	2-3	0.61 0.58 0.54	39.14	0.2168	0.2062	0.1920
	1-2	0.71 0.70 0.01	4.22	0.0261	0.0258	0.0004
tk5_9	1-3	0.63 0.58 0.51	41.85	0.2409	0.2218	0.1950
	2-3	0.61 0.57 0.54	39.66	0.2200	0.2055	0.1947
	1-2	0.72 0.70 0.01	3.80	0.0239	0.0232	0.0003
tk5_11	1-3	0.60 0.59 0.54	40.21	0.2196	0.2160	0.1977
	2-3	0.63 0.60 0.50	42.67	0.2467	0.2343	0.1953
	1-2	0.72 0.69 0.01	4.91	0.0309	0.0296	0.0004
tk5_13	1-3	0.62 0.61 0.50	39.86	0.2248	0.2212	0.1813
	2-3	0.65 0.55 0.52	41.86	0.2486	0.2103	0.1989
	1-2	0.72 0.69 0.01	4.55	0.0286	0.0274	0.0004
tk5_14	1-3	0.59 0.59 0.54	39.32	0.2108	0.2108	0.1929
	2-3	0.60 0.60 0.50	41.50	0.2309	0.2301	0.1922
	1-2	0.72 0.70 0.00	4.68	0.0294	0.0286	0.0000
tk5_17	1-3	0.60 0.60 0.50	41.50	0.2273	0.2273	0.1894
	2-3	0.60 0.60 0.50	40.20	0.2240	0.2090	0.2002
	1-2	0.72 0.69 0.01	5.47	0.0344	0.0330	0.0005
tk5_18	1-3	0.60 0.60 0.50	42.10	0.2401	0.2246	0.1993
	2-3	0.60 0.60 0.60	40.40	0.2245	0.2091	0.2022
	1-2	0.71 0.70 0.01	4.01	0.0249	0.0245	0.0003

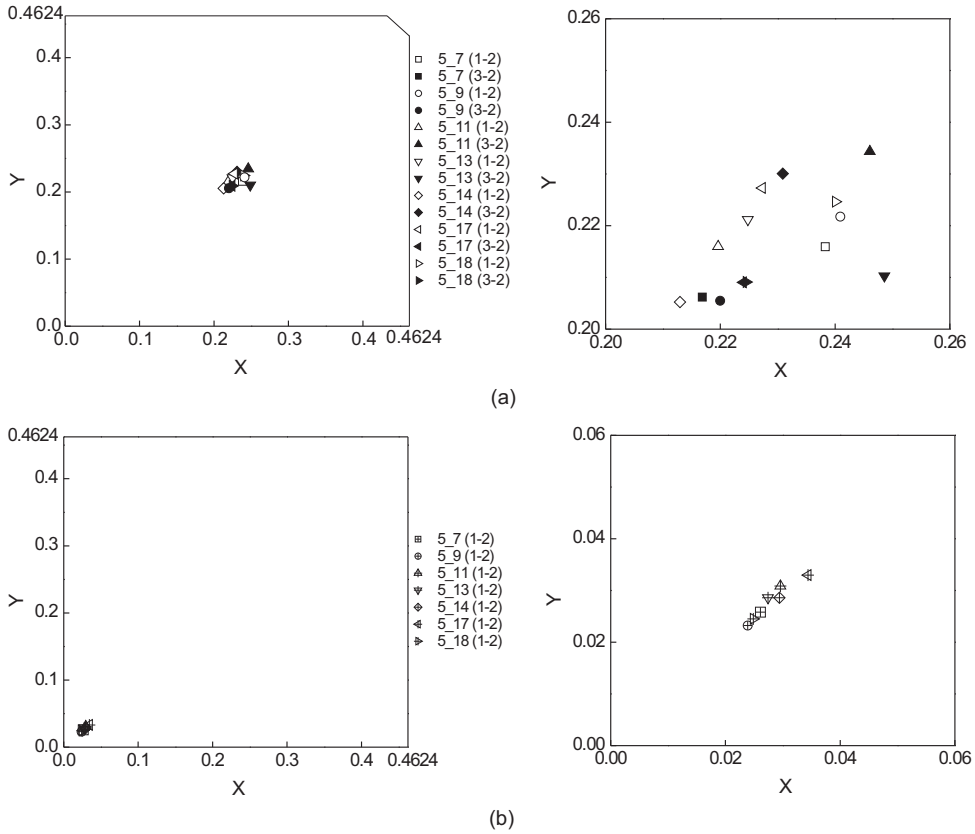

Figure B.4: Sections of Rodrigues space (a) at Z=0.1813..0.2022 with misorientations between grain 1 and grain 3 (1-3) and grain 3 and grain 2 (3-2), (b) at at Z=0..0.0005 with misorientations between grain 1 and grain 2 (1-2)

Series 6 (Chapter 6)

Three grain boundaries are 40° <111> tilt boundaries (Tabl. B.5, Fig. B.5).

Table B.5: Disorientations between the grains in tricrystals of series 6

Tricrystal	Neighboring grains	$r_x\ r_y\ r_z$	$\omega°$	R_x	R_y	R_z
tk6_8	1-3	0.59 0.59 0.56	40.11	0.2141	0.2137	0.2044
	2-3	0.62 0.56 0.55	38.97	0.2199	0.1931	0.1987
	1-2	0.64 0.56 0.53	38.78	0.2237	0.1975	0.1866
tk6_18	1-3	0.61 0.58 0.54	39.02	0.2186	0.2059	0.1915
	2-3	0.62 0.57 0.54	39.75	0.2224	0.2064	0.1965
	1-2	0.60 0.59 0.54	39.01	0.2116	0.2088	0.1925
tk6_19	1-3	0.60 0.59 0.54	39.02	0.2114	0.2088	0.1930
	2-3	0.62 0.56 0.55	39.51	0.2232	0.2017	0.1961
	1-2	0.60 0.59 0.54	40.21	0.2211	0.2151	0.1970
tk6_20	1-3	0.61 0.58 0.54	39.05	0.2148	0.2074	0.1912
	2-3	0.60 0.59 0.54	41.16	0.2193	0.2143	0.1991
	1-2	0.59 0.58 0.57	39.17	0.2083	0.2052	0.2074

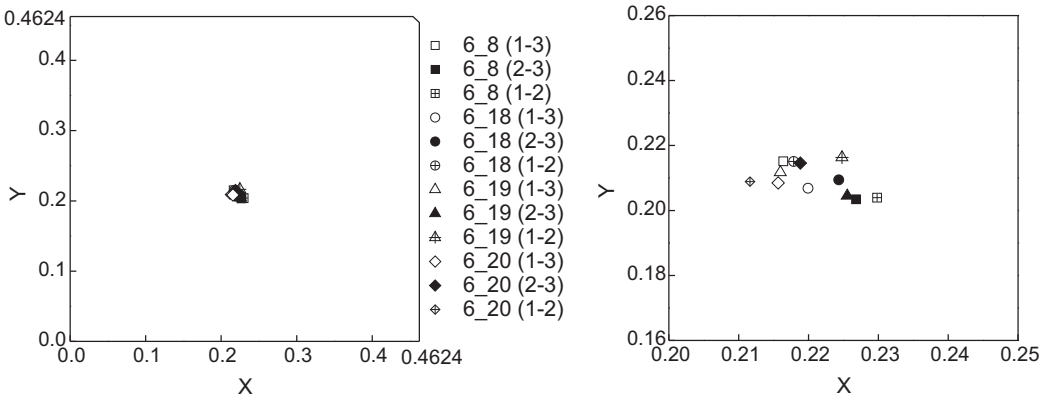

Figure B.5: Sections of Rodrigues space at Z=0.1866..0.2044 with misorientations between grain 1 and grain 2 (1-2), grain 3 and grain 2 (3-2) and grain 1 and grain 2 (1-2)

Appendix C

Analysis of experimental errors

An error (or uncertainty) is defined as the difference between a measured or estimated value for a quantity and its true value, and is inherent in all experiments. Therefore, reported experimental results should always include a realistic estimate of their errors. Errors may be divided roughly into two categories: indeterminate and determinate errors. The detailed report on error analysis in experimental science is done by Simanek in [70]. Below we briefly introduce two categories of errors and estimate uncertainties of our measurements.

C.1 Indeterminate errors

Indeterminate errors are present in all experimental measurements. There is no way to determine the size or sign of the error in any individual measurement. Indeterminate errors cause a measuring process to give different values when that measurement is repeated many times (assuming all other conditions are held constant). Indeterminate errors can have many causes, including operator errors or biases, varying environmental conditions and inherent variability of measuring instruments.

The effect that indeterminate errors have on results can be somewhat reduced by taking repeated measurements then calculating their avarage. The average is generally considered to be a "better" representation of the "true value" than any single measurement, because errors of positive and negative sign tend to compensate each other in the averaging process.

C.2 Determinate errors

A common cause of determinate (systematic) errors is instrumental or procedurial bias. For instance, a miscalibrated scale or instrument. Another cause is an experimental blunder. For instance, reading a scale incorrectly or using an incorrect values of a constant in the equations.

Every effort should be made to reduce the possibility of these errors, by careful calibration of the experimental equipment and by use the best possible measurement technique.

Determinate errors can be more serious than indeterminate errors for the following reasons

- There is no method for discovering and identifying them just by looking at the experimental data.
- Their effect can not be reduced by averaging repeated measurements.
- A determinate error has the same size and sign for each mesurement.

C.3 Experimental errors in the present work

C.3.1 Experimental errors in measurements of grain boundary and triple junction mobilities (Chapter 3 – Chapter 5)

The activation enthalpy H and pre-exponential A_0 factor of grain boundary and triple junction motion were determined in accordance with Eqs. (3.4), (5.12), (5.13) from measurements of the velocity of moving grain boundaries at different temperatures utilizing the least squares method:

$$H = \frac{n\left(\sum xy\right) - \left(\sum x\right)\left(\sum y\right)}{n\left(\sum\left(x^2\right)\right) - \left(\sum x\right)^2}, \tag{C.1}$$

$$A_0 = \frac{\left(\sum y\right)\left(\sum\left(x^2\right)\right) - \left(\sum x\right)\left(\sum xy\right)}{n\left(\sum\left(x^2\right)\right) - \left(\sum x\right)^2}, \tag{C.2}$$

where x is the reduced temperature (T^{-1}), y is the reduced mobility of grain boundary (A_{gb}) or triple junction (A_{tj}), n is the number of experimental points.

The indeterminate errors ΔH and ΔA_0 were calculated as the Root Mean Squared Error (RMSE). The Mean Squared Error (MSE) is given by

$$\frac{1}{n+1}\left(X_i - X_{ev}\right)^2, \tag{C.3}$$

where $X_{ev} = \left(X_1 + ... + X_n\right)/n$, X_i is the measured quantity. The RMSE is simply the square root of the MSE.

The calculated ΔH and ΔA_0 are represented in Tabls. 3.1, 3.2 and 5.2. The instrumental errors in the velocity and of contact angle measurements are negligibly small in comparison to the scattering experimental points, therefore we do not take them into account.

C.3.2 Experimental errors in measurements of the excess free volume of grain boundaries (Chapter 6).

We make three following assumptions: first we suppose that there is no geometrical distortions of microscopic images during transfer from the SEM to the computer. The error of the contact angle 2θ measurement is indeterminate and is calculated as the RMSE. Second, accuracy of measurement of the crystal orientation of $\pm 0.4^\circ$ includes all process errors: astigmatism of X-Ray beam in the Laue-equipment, deformation of the X-Ray film during its processing etc. Third, deviations of the rotation axis from its "ideal" position is neglected and the energy of the grain boundary is calculated through the misorientation angle (see representation of crystal orientation in Paragraph 1.1.1). Combining Eq. (6.38) with Eq. (6.40) we obtain

$$V^{ex} = \frac{\partial \gamma_b}{\partial p} = \frac{1}{\cos\theta}\frac{Gb}{4\pi}\psi\left(A - \ln\psi\right). \tag{C.4}$$

Below we derive an equation for the relative experimental error in measurements of the BFV (Eqs. (C.5)–(C.8)).

$$\frac{\Delta V^{ex}}{V^{ex}} = \frac{\Delta\left(\frac{\partial\gamma_b}{\partial p}\right)}{\left(\frac{\partial\gamma_b}{\partial p}\right)}, \tag{C.5}$$

$$\ln\left(\frac{\partial\gamma_b}{\partial p}\right) = \ln\left(\frac{1}{\cos\theta}K\psi(A - \ln\psi)\tan\theta\frac{\partial\theta}{\partial p}\right), \tag{C.6}$$

$$\begin{aligned} \ln\left(\frac{\partial\gamma_b}{\partial p}\right) &= \ln\left(\frac{1}{\cos\theta}\right) + \ln(K) + \ln(\psi) + \\ &\quad \ln(A - \ln\psi) + \ln(\tan\psi) + \\ &\quad \ln\left(\frac{\partial\theta}{\partial p}\right), \end{aligned} \tag{C.7}$$

$$\begin{aligned} \frac{\Delta\left(\frac{\partial\gamma_b}{\partial p}\right)}{\left(\frac{\partial\gamma_b}{\partial p}\right)} &= \frac{\sin\theta}{\cos\theta}\Delta\theta + \frac{\Delta\psi}{\psi} + \frac{1}{(A - \ln\psi)}\frac{\Delta\psi}{\psi} + \\ &\quad \frac{1}{\tan\psi\cos^2\psi}\Delta\psi + \frac{\Delta\left(\frac{\partial\theta}{\partial p}\right)}{\left(\frac{\partial\theta}{\partial p}\right)}, \end{aligned} \tag{C.8}$$

where K, K_2 are constants. The following values are used: ψ=0.066 [rad] (3.8°), $\Delta\psi$=0.007 [rad] (0.4°), θ=1.326 [rad] (76.0°), $\Delta\theta$=0.028 [rad] (1.6°), $\frac{\partial\theta}{\partial p}$=0.3799 $\left[\frac{m^2}{N}\right]$, $\Delta\left(\frac{\partial\theta}{\partial p}\right)$=0.0302 $\left[\frac{m^2}{N}\right]$.

$$\frac{\Delta V^{ex}}{V^{ex}} \approx 0.33$$

The relative experimental error in the measurments of the excess free volume of high angle <111> grain boundaries is about 33 %.

Lebenslauf

Persönliche Daten:

Name	Vladimir A. Ivanov
Geburtsdatum und –ort	3. Dezember 1975, Moskau, Russland
Staatsangehörigkeit	russisch

Schulbildung und Studium:

09/1983-06/1993	Allgemeinbildende Schule № 549, Moskau
09/1993-02/1999	Staatliches Institut für Stahl und Legierungen (Technologische Universität), Moskau, Russland
02/1999	Abschluss Diplom-Ingenieur

Berufliche Erfahrung:

03/1999-12/2000	wissenschaftlicher Angestellter, Lehrstuhl für Physikalische Chemie, Staatliches Institut für Stahl und Legierungen (Technologische Universität), Moskau, Russland
01/2001-01/2006	wissenschaftlicher Angestellter, Institut für Metallkunde und Metallphysik der RWTH Aachen, Aachen, Deutschland
02/2006-05/2006	wissenschaftlicher Angestellter, School of Computational Sciences, George Mason University, Fairfax, VA, Vereinigte Staaten von Amerika
seit 06/2006	wissenschaftlicher Angestellter, Department of Physics and Astronomy, George Mason University, Fairfax, VA, Vereinigte Staaten von Amerika